

Increased efficiency of current-induced chiral domain wall motion by interface engineering

Dissertation

Zur Erlangung des Doktorgrades der Ingenieurwissenschaften
(Dr. rer. nat.)

der

Naturwissenschaftlichen Fakultät II
Chemie, Physik und Mathematik

Der Martin-Luther-Universität Halle-Wittenberg

vorgelegt von

Herrn Yicheng Guan

geb. am 03.08.1992 in Wuxi, Jiangsu Province, China

Gutachter: Prof. Dr. Stuart S.P. Parkin
Prof. Dr. Georg Woltersdorf
Prof. Dr. Günter Reiss

Tag der öffentlichen Verteidigung: 27.05.2021

Abstract

Racetrack devices based on chiral domain wall magnetic bits in perpendicularly magnetized ferromagnet/heavy metal thin film systems are promising candidates for next-generation spintronic memories. Néel type domain walls are stabilized in such devices by an interfacial Dzyaloshinskii-Moriya interaction. These Néel type domain walls can be readily manipulated by the injection of spin currents generated from electrical currents in the heavy metal layers. More efficient current-induced domain wall motion is needed for commercially viable, fast, and low power racetrack memory devices. In this thesis we demonstrate significantly increased efficiency of domain wall motion with substantially lowered threshold current densities and enhanced domain wall velocities by the introduction of atomically thin $4d$ and $5d$ metal “dusting” layers at the ferromagnetic/heavy metal interfaces. The greatest efficiency is found for dusting layers of Pd and Rh, just one monolayer thick at Pt/Co interfaces, for which the domain wall’s velocity is increased by up to a factor of 3.5. This is due to a subtle interplay of several spin-orbitronic parameters. This thesis demonstrates a path to increased efficiency of chiral domain wall motion by tailored interfaces in racetrack devices.

Contents

1. Introduction	1
2. Background	5
2.1. Ferromagnetism, magnetic energy, and magnetic domain wall	6
2.2. Magnetic dynamics and field-driven DW motion.....	15
2.3. Interfacial Dzyaloshinskii-Moriya interaction in multilayer system.....	20
2.4. Current induced domain wall motion.....	24
2.4.1. Current induced domain wall motion by spin-transfer torque.....	24
2.4.2. Current induced domain wall motion by spin-orbit torque	29
2.4.3. Current induced domain wall motion in the synthetic anti-ferromagnet structure	37
3. Experimental methods.....	45
3.1. Sample preparation and lithography.....	45
3.2. Differential Kerr Microscopy based on Magnet-Optic Kerr Effect	48
3.3. Set-up for Current-induced Domain Wall Motion	52
4. CIDWM in FM and SAF structures with 4d and 5d DL insertions	55
4.1. Current-induced chiral DW motion in FM structure with DL insertion	55
4.1.1. DL thickness and material dependence of CIDWM in FM structure	55
4.1.2. Temperature, pulse length, and device size dependence of CIDWM in FM structure..	59
4.1.3. Longitudinal field dependence of CIDWM in FM structure with DLs.....	65
4.2. Current-induced chiral DW motion in SAF structure with DL insertions	68
4.2.1. DL thickness and material dependence of CIDWM in SAF structure	68
4.2.2. Longitudinal field dependence of CIDWM in SAF structure with DLs.....	71
5. Discussions of CIDWM in FM and SAF structures with DL insertions.....	73
5.1. SQUID measurement for the magnetic properties of FM and SAF structures with DLs	74
5.2. Calculation of interfacial DMI constant of FM structures with DLs	78
5.3. Fitting of the v - J curve in FM structures with DLs using a simplified I - D model	81
5.4. Threshold spin current density based on DW mobility in FM structures with DLs	85

5.5.	Simplified 1-D model for ECT driven DWM and threshold spin current density based on DW mobility in SAF structures with DLs.....	89
5.6.	Illustration of v_{lg} by simulations from the 1-D analytical model for CIDWM under longitudinal magnetic field in SAF structure.....	92
6.	CIDWM in FM and SAF structures with Co-sputtered Pt/Pd DL insertion	95
6.1.	Magnetic properties of FM and SAF structures with Co-sputtered Pd _{0.31} Pt _{0.69}	95
6.2.	CIDWM in FM and SAF structures with Co-sputtered Pd _{0.31} Pt _{0.69} DL	97
6.3.	Longitudinal field dependence of CIDWM in FM and SAF structures with Co-sputtered Pd _{0.31} Pt _{0.69} DLs.....	101
6.4.	Effective spin Hall angle and threshold spin current density based on DW mobility and threshold current density in FM and SAF structures with Co-sputtered Pd _{0.31} Pt _{0.69} DLs.....	103
7.	CIDWM in FM structure with sandwiched HM layer	105
7.1.	Magnetic properties of FM structure with sandwiched HM layer	105
7.2.	CIDWM in FM structure with sandwiched HM layer.....	107
8.	Transport measurement for FM structure with DL insertions	111
8.1.	Hall measurement for the FM structure with DL insertions.....	111
8.2.	Second-harmonic measurement for the FM structure with Pd and Rh DLs.....	116
9.	Conclusion	123
	Bibliography.....	127
	Appendix	137
A.	Macro-magnetic derivation of second harmonic Hall signal for determination of effective fields.....	137
B.	Supplementary figures.....	143
B.1.	Film characterizations with AFM and XRD.....	143
B.2.	Fitting for the longitudinal field dependence of DW velocity in SAF structure using a 1-D analytical model.....	145
B.3.	Determination of the Gilbert damping parameter from optical ferromagnetic resonance (OFMR) measurements.....	151
	Acknowledgment	153

List of Figures

Figure 1-1: Illustration of racetrack memory devices.....	1
Figure 1-2: Evolution of racetrack memory from generation 1 to generation 4.....	3
Figure 2-1: Illustration of a ferromagnet, anti-ferromagnet, and ferrimagnet system.....	6
Figure 2-2: Mechanism for the appearance of magnetization by band polarization.....	8
Figure 2-3: Function plot of the RKKY interaction.....	9
Figure 2-4: Orientation of magnetization in a magnetic thin film.....	10
Figure 2-5: The magnetization coordinates inside a domain wall.....	13
Figure 2-6: Top view of magnetization profiles of Néel wall and Bloch wall configuration in a PMA system.....	14
Figure 2-7: Schematic illustration of the torques exerted on the magnetization by the application of an effective magnetic field.....	16
Figure 2-8: The field-driven DW motion with Walker breakdown.....	19
Figure 2-9: Illustration of the Dzyaloshinskii-Moriya interaction at the FM/HM interface.	21
Figure 2-10: Néel walls with different fixed chirality.....	22
Figure 2-11: Simulation and experimental results for field-induced DW motion with the presence of DMI.....	23
Figure 2-12: Schematic illustration of spin-transfer torque in a spin valve structure.....	25
Figure 2-13: Simulation results of CIDWM velocity as a function of spin drift velocity.....	28
Figure 2-14: Microscopic origin of the spin galvanic effect and inverse spin galvanic effect.....	30
Figure 2-15: Illustration of the anomalous Hall effect, spin Hall effect, and inverse spin Hall effect.....	31
Figure 2-16: Schematic illustration of spin current generated from the SHE of the HM layer in the FM/HM system.....	32
Figure 2-17: SOT-driven DWM with the presence of interfacial DMI.....	35
Figure 2-18: Antiferromagnetically coupled Néel DWs in the SAF structure.....	38
Figure 2-19: The current-induced DW velocity in the FM/HM case and SAF case plotted as a function of the exterior longitudinal magnetic field.....	42
Figure 2-20: Exchange coupling torques in the SAF structure.....	43
Figure 3-1: FM and SAF structure with DL insertions.....	46
Figure 3-2: The device fabrication process with photolithography and SEM images of racetrack devices.....	47
Figure 3-3: The Kerr microscope image of a typical FM structure.....	49

Figure 3-4: Current-induced domain wall motion measured under differential Kerr microscopy.	51
Figure 3-5: The set-up for current-induced domain wall motion.	53
Figure 4-1: Current-induced chiral domain wall motion in FM structure with various DLs.	57
Figure 4-2: The DL thickness dependence of threshold current density, DW mobility, and DW velocity at a fixed current density in FM structures with DL insertion.	59
Figure 4-3: Temperature dependence of CIDWM in FM structure.	60
Figure 4-4: Dependence of the CIDWM on pulse length in FM structure.	62
Figure 4-5: Wire width dependence of CIDWM in FM structure.	64
Figure 4-6: Longitudinal field dependence of the DW velocity in FM structure with various DLs.	66
Figure 4-7: DL thickness dependence of DMI effective field in FM structures.	67
Figure 4-8: Current-induced chiral domain wall motion in SAF structure with various DLs.	69
Figure 4-9: The DL thickness dependence of threshold current density, DW mobility, and DW velocity at a fixed current density in SAF structures with DL insertion.	70
Figure 4-10: Longitudinal field dependence of the DW velocity in SAF structure with various DLs.	72
Figure 5-1: The magnetic hysteresis loops in FM and SAF structures.	74
Figure 5-2: Magnetic properties obtained from the Magnetization Hysteresis loop in FM and SAF structures.	76
Figure 5-3: Magnetic hysteresis loop of samples with Ru DL insertion.	77
Figure 5-4: DL thickness dependence of DW width and interfacial DMI constant.	79
Figure 5-5: Interfacial DMI constant as a function of effective uniaxial anisotropy.	80
Figure 5-6: The fitting curve of the v - J curve under the subtraction of J_{th} in FM structures with DLs.	82
Figure 5-7: DL thickness dependence of v_D and J_D obtained from the I - D model fitting and comparison of D_s	84
Figure 5-8: Threshold current density in FM structures plotted as a function of DMI constant and effective uniaxial anisotropy energy.	85
Figure 5-9: DL thickness of the effective θ_{SH} obtained from the DW mobility around the threshold current density.	87
Figure 5-10: The pinning potential plotted as a function of effective uniaxial anisotropy energy and interfacial DMI constant.	88

Figure 5-11: The illustration of the v - J curve of SOT-driven DW motion and ECT-driven DW motion.	90
Figure 5-12: The threshold spin current density plotted as a function of effective uniaxial anisotropy energy and interfacial DMI constant of the lower magnetic layer. ...	91
Figure 5-13: Simulation results based on a I - D analytical model for the dependence of the SAF CIDWM versus the longitudinal field.....	94
Figure 6-1: Magnetic properties obtained from the Magnetization Hysteresis loop in FM and SAF structures with co-sputtered Pd _{0.31} Pt _{0.69} DL.	96
Figure 6-2: Current-induced chiral domain wall motion in FM and SAF structures with Co-sputtered Pd _{0.31} Pt _{0.69} DLs.	97
Figure 6-3: The DL thickness dependence of threshold current density, DW mobility, and DW velocity at a fixed current density in FM structures with Pd _{0.31} Pt _{0.69} DL insertion.	99
Figure 6-4: The DL thickness dependence of threshold current density, DW mobility, and DW velocity at a fixed current density in SAF structures with Pd _{0.31} Pt _{0.69} DL insertion.	100
Figure 6-5: Longitudinal field dependence of the DW velocity in FM and SAF structure with different DL thicknesses.....	101
Figure 6-6: Interfacial DMI constant as a function of effective uniaxial anisotropy and DL thickness dependence of v_{lg}	102
Figure 6-7: DL thickness of the effective spin Hall angle obtained from the DW mobility around the threshold current density in the FM and SAF structures.	103
Figure 6-8: The threshold spin current density plotted as a function of effective uniaxial anisotropy energy in FM and SAF structures.....	104
Figure 7-1: Magnetic properties obtained from the Magnetization Hysteresis loop in FM structure with sandwiched HM layer.	106
Figure 7-2: Current-induced chiral domain wall motion in FM structure with sandwiched HM layers.	107
Figure 7-3: Longitudinal field dependence of the DW velocity in FM structure with sandwiched HM layer and calculated DMI constant.	108
Figure 7-4: The upper Pt layer thickness dependence of effective spin Hall angle and threshold spin current plotted as a function of effective uniaxial anisotropy energy in FM structure with sandwiched Pt HM.	109
Figure 8-1: Device structure and experimental set-up for the Hall measurements and measurement results.....	113
Figure 8-2: The Hall measurement to obtain planar Hall resistance.....	115
Figure 8-3: Experimental set-up for the harmonic Hall measurement and obtained harmonic Hall signals.	116

Figure 8-4:	The calculated Damping-like and Field-like effective field plotted as a function of injected current density in Pd and Rh DL cases.	118
Figure 8-5:	DL thickness dependence of calculated effective Damping-like and Field-like torque efficiency.	119
Figure 8-6:	DL thickness dependence of calculated effective Damping-like to Field-like torque efficiency ratio.	120
Figure A-1:	Schematic illustration of a magnetic film with PMA under the application of the exterior magnetic field.	137
Figure B-1:	AFM topographic images of typical films with and without interfacial DLs. .	143
Figure B-2:	The x-ray diffraction (XRD) patterns of the SAF structures with Pd dusting layer insertions.	144
Figure B-3:	Fitting results of CIDWM in SAF.	145
Figure B-4:	Fitting results of CIDWM in SAF.	146
Figure B-5:	Fitting results of CIDWM in SAF.	147
Figure B-6:	Fitting results of CIDWM in SAF.	148
Figure B-7:	Fitting results of CIDWM in SAF.	149
Figure B-8:	Fitting results of CIDWM in SAF.	150
Figure B-9:	OFMR determined Gilbert damping parameter for samples with DLs.	151

List of Tables

Table 5.1:	Values of K_u^{eff} corresponding to zero pinning strength for CIDWM and $D=0$ for FM structures with 4d and 5d DLs.	88
Table 5.2:	Magnetic parameters used in the simulation based on a I - D analytical model for Figure. 5.12.....	94

Acronyms

CMOS	complementary metal-oxide-semiconductor
FM	ferromagnetic
HM	heavy metal
DL	dusting layer
GMR	giant magnetoresistance effect
PMA	perpendicular magnetic anisotropy
DW	domain wall
LLG	Landau-Lifshitz-Gilbert
CIDWM	current-induced domain wall motion
STT	spin-transfer torque
SOC	spin-orbit coupling
SHE	Spin Hall effect
SGE	spin galvanic effect
SOT	spin-orbit torque
SAF	synthetic anti-ferromagnetic
ECT	exchange coupling torque
RKKY	Ruderman-Kittel-Kasuya-Yosida
DMI	Dzyaloshinskii-Moriya interaction
MOKE	magnetic optical Kerr effect
XRD	X-ray diffraction
OFMR	optical ferromagnetic resonance

1. Introduction

Solid-state spintronic devices are recognized as one of the most promising candidates to enable ‘beyond CMOS’ technologies for solid-state data storage, logic, and neuromorphic computing applications [1-6]. The operation of these devices is primarily based on the generation and manipulation of spin-polarized currents. These currents can be used, in particular, to manipulate magnetic bits that are encoded within magnetic spin textures (domains [7], skyrmions [8], or antiskyrmions [9]) in nanoscale racetracks. A racetrack-based memory, as shown in Figure 1.1, is fundamentally a shift register in which the fast and energy-efficient motion of such magnetic bits along 2D or 3D racetracks by a spin current is a crucial challenge for its commercial implementation [7, 10].

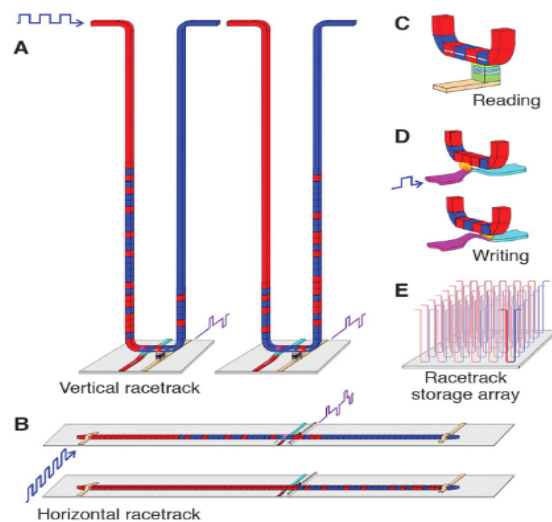


Figure 1-1: Illustration of racetrack memory devices. (A) 3D racetrack memory devices with a vertical track, the magnetic domain walls are manipulated by current pulse injections along the racetrack; (B) 2D racetrack memory with a horizontal configuration; (C) a reading device integrated into a racetrack memory based on a magnetic tunnel junction (MTJ); (D) a possible writing device for a racetrack using current pulse injection; (E) a high-density storage array of vertical racetrack memory devices. This figure is adopted from ref [5].

Chapter 1

Current-induced DW motion (CIDWM) has significantly evolved from in-plane magnetic [11] to perpendicularly magnetized synthetic antiferromagnetic (SAF) [12] racetracks due to advances in volume spin-transfer torque (STT) [13, 14] and spin-orbit torque (SOT) [15-17] mechanisms (Figure 1.2). Driven by a chiral spin torque that arises from the spin-orbit coupling in the presence of broken inversion symmetry at ferromagnet/heavy metal (HM) interfaces [18], Néel DWs in thin films with strong perpendicular magnetic anisotropy (PMA), stabilized by a Dzyaloshinskii-Moriya interaction (DMI) at the ferromagnet/HM interfaces [19, 20], can be moved along the current direction at high velocities [16, 17, 21], in both straight and curved racetracks [22, 23]. An even more efficient DW motion was reported in synthetic antiferromagnet (SAF) racetracks that are composed of two perpendicularly magnetized ferromagnetic sub-racetracks coupled antiferromagnetically across an ultrathin ruthenium layer [12]. The giant exchange coupling torque (ECT) in the SAF structure provides an additional dominating driving mechanism that allows for an increased DW propagation velocity beyond $\sim 1,000$ m/s. The ECT in rare earth-transition metal alloys is further maximized at the angular momentum compensation temperature of the ferrimagnetic alloy [24, 25]. Recently, efficient CIDWM was also found in certain magnetic insulators [26].

Chapter 1

Significant progress has been made regarding a detailed understanding of the interface derived chiral spin torque [21] and magnetic chirality [27] to the underlying mechanisms of CIDWM [28, 29], for example, by varying the HM underlayer that is in contact with the interface ferromagnetic layer [21, 30] or by tuning the thickness of the ferromagnetic layers [17, 31, 32]. The notion of interfacial dusting layers (DL) was initially proposed to demonstrate the interfacial origin of the giant magnetoresistance (GMR) effect, in which atomically thin ferromagnetic layers were inserted at the interfaces in sandwich structures [33]. There has been significant interest in the insertion of DLs in several studies, primarily related to the switching of the magnetic moment of micro-elements [26, 34-38]. In this thesis, we show that by introducing atomically thin dusting layers of selected $4d$ and $5d$ HMs at the ferromagnet/platinum interface, a significantly enhanced efficiency of CIDWM is achieved for both single magnetic layers and SAF racetrack structures. The Néel DWs move up to more than three times faster, for the same injected current density, compared to otherwise identical structures without any DL. Moreover, the threshold current density, J_{th} , defined as the minimum current density required to overcome the effective pinning field and move the DWs, can be substantially reduced by incorporating atomically thin DLs. Significant modifications of the interfacial magnetic properties originating from the spin-orbit coupling have been brought to the system through the DL insertions, and the inner relationship between specific physical parameters is revealed.

This thesis is organized with the following structure: Chapter 2 gives a theoretical background of magnetism, magnetic dynamics, and current-induced domain wall motion; Chapter 3 illustrates the experimental methods and set-ups used in this thesis; Chapter 4 shows CIDWM results for both single magnetic layers and SAF samples with selected $4d$ and $5d$ DL insertions; Chapter 5 discusses the mechanisms responsible for the enhanced CIDWM performance in both types of samples; Chapter 6 shows CIDWM results for a co-sputtered Pt/Pd alloy DL; Chapter 7 contains the CIDWM results of a modified HM layer with a sandwich structure; Chapter 8 discusses the transport properties of single magnetic layer samples with DL insertions including the anomalous Hall resistance, planar Hall resistance and the spin-orbit torque efficiency from harmonic Hall measurements; a conclusion and outlook for future research are presented in Chapter 9.

2. Background

In this chapter, the theoretical background of the current induced domain wall motion will be introduced, starting from the introduction of physical mechanisms in magnetic orders, formation of magnetic domain walls by the relevant energy terms, including the interfacial Dzyaloshinskii-Moriya interaction. The magnetization dynamics of domain walls motivated by field, spin-transfer torque, and spin-orbit torque are also introduced. Finally, the current-induced domain wall motion in a synthetic anti-ferromagnetic structure by the exchange coupling torque is introduced.

2.1. Ferromagnetism, magnetic energy, and magnetic domain wall

The term ferromagnetism is used to describe a material with spontaneous non-zero magnetization due to the atomic spins aligned collectively in the same direction without any exterior magnetic field application [39-41]. In early research, such spontaneous alignment is believed to be caused by an inner molecular field in the direction of net magnetization [42, 43]. The atomic magnetic dipoles cannot account for this molecular field since its large magnitude. The molecular field is then explained by the Heisenberg exchange model that describes the interaction between neighboring atoms spins, which could be written in the following form [44]:

$$\mathcal{H} = -2J_{\text{ex}}\mathbf{S}_i \cdot \mathbf{S}_j \quad (2.1)$$

J_{ex} is the exchange coupling constant and $\mathbf{S}_{i/j}$ is the spin of the atoms located at $i_{\text{th}}/j_{\text{th}}$ location. To reach the minimum energy state, for ferromagnetic materials, J_{ex} is positive, and thus the spins will all align in the same direction. When the exchange coupling constant is negative, the most neighboring spins will form an anti-parallel alignment. If both atomic spins have the same magnitude, an anti-ferromagnetic system with zero net magnetization is formed. When the most neighboring magnetic moments have different magnitude, such a system is named as ferrimagnet. The schematic illustration of ferromagnet, anti-ferromagnet and ferrimagnet are shown in Figure 2.1.

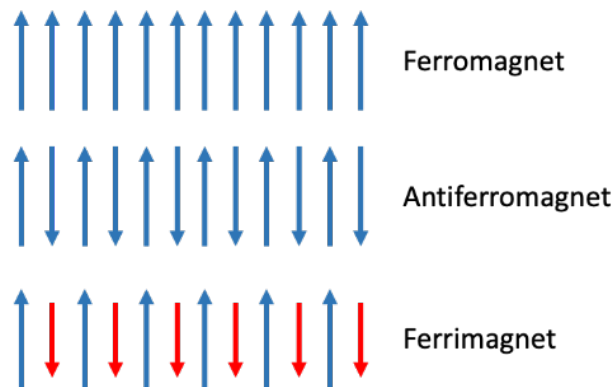


Figure 2-1: Illustration of a ferromagnet, anti-ferromagnet, and ferrimagnet system. The different colors indicate the magnetic moments from different atoms.

Chapter 2

Only a few metallic materials exhibit ferromagnetism, including three $3d$ transition metals of Fe, Ni, and Co, and a few heavy rare earth metals like Gd, Dy, etc. Even though the Heisenberg exchange model has given an excellent description of ferromagnetism by direct interaction between localized spins, in these real materials, the description is still not precise enough. In the $3d$ transition metal case, the $3d$ electrons which possess the magnetism, are quite far away from the atomic core and can effectively move among the atoms. In other words, they form a band structure. Such ferromagnetism formed from the spin polarization in band structures is called itinerant ferromagnetism. In heavy rare earth metals, the $4f$ electrons, as the carrier of magnetism, are deeply located inside the atoms, and hence it's called localized ferromagnetism.

In the itinerant ferromagnets as the $3d$ transition metals, the spontaneous magnetization in band structure can be well described by the *Stoner Criterion* [45]. Considering a free-electron system, at finite temperature, the condition at Fermi level defined by:

$$N = \int_0^{\infty} f(E)g(E)dE \quad (2.2)$$

Where $f(E)$ the Fermi-Dirac distribution is function and $g(E)$ gives the density of states. In a ferromagnetic metal, the band will split into two bands of majority (+) and minority (-) spins, and the number of electrons occupies each band is:

$$\begin{cases} N_+ = \int_{-\infty}^{+\infty} g(E)f(E_f + H_m M_B)dE \\ N_- = \int_{-\infty}^{+\infty} g(E)f(E_f - H_m M_B)dE \end{cases} \quad (2.3)$$

Here, H_m is the effective molecular field with the form of wM , E_f is the Fermi energy level, and M_B is the magnetic moment of the electrons. Thus, the magnetization induced by the polarization of the band is:

$$M = M_B(N_+ - N_-) \quad (2.4)$$

Chapter 2

With the presence of the molecular field, when the spontaneous magnetization appears, it could be viewed as moving electrons from minority band to majority band, as shown in Figure 2.2. Thus, the total energy, including the kinetic energy and magnetic energy, will have the following form:

$$\Delta E = \Delta E_M + \Delta E_K = -\frac{1}{2}wM^2 + \frac{1}{2}\frac{M^2}{\chi_p} = \frac{1}{2}\frac{M^2}{\chi_p}(1 - w\chi_p) \quad (2.5)$$

χ_p is the magnetic susceptibility with the form of $2g(E_f)M_B^2$. When $\Delta E < 0$ as $1 < w\chi_p$, the system energy will decrease with adding the magnetization of the system, which means the system will favor a ferromagnetic state. By defining $U = 2wM_B^2$, the *Stoner Criterion* for the band ferromagnetism is written in a more familiar form as:

$$Ug(E_f) \geq 1 \quad (2.6)$$

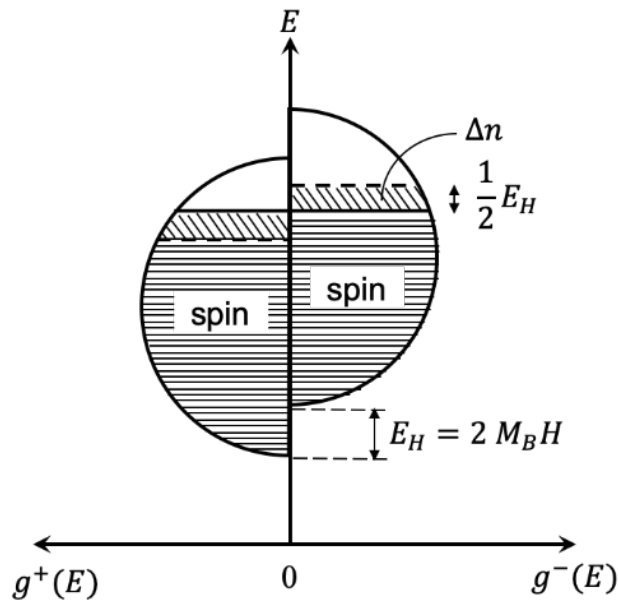


Figure 2-2: Mechanism for the appearance of magnetization by band polarization. This figure is replotted from Ref [43].

Chapter 2

Unlike the $3d$ transition ferromagnetic metals, in the $4f$ rare earth metals, the strong localization of the ferromagnetism makes it extremely hard to interact with each other directly [41, 43]. The conduction $5d/6s$ electrons, then, served as the intermedium for the exchange interaction between the $4f$ spin, which induces ferromagnetism. When a magnetic impurity is introduced to the conduction band, it will give rise to an oscillating polarization as follows:

$$F(\xi) = \frac{\sin\xi - \xi\cos\xi}{\xi^4} \quad (2.7)$$

Here, $\xi = 2k_F r$, as k_F is the Fermi wave vector and r is the distance to the magnetic impurity. With varying the distance, the coupling will also vary between the ferromagnetic and anti-ferromagnetic coupling, as shown in Figure 2.3. Such indirect exchange interaction is called *RKKY* interaction, a name from the initials of authors of Ruderman and Kittel, Kasuya, and Yasida [46-48]. Apart from the ferromagnetism in $4f$ rare earth metals, the RKKY interaction is also responsible for the anti-ferromagnetism, helimagnetism, and the inter-layer exchange coupling in the multilayer structure because of its long-range nature [49, 50].

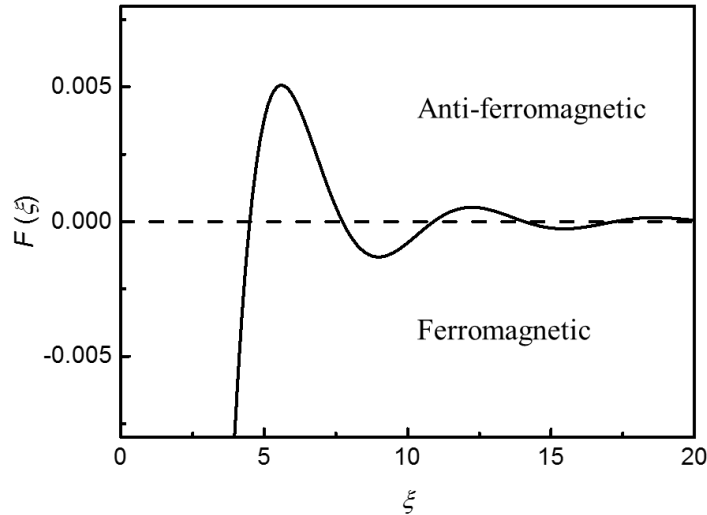


Figure 2-3: Function plot of the RKKY interaction. When the function $F(\xi)$ is positive, it means the exchange interaction is ferromagnetic, while the negative value indicates the anti-ferromagnetic exchange interaction.

Chapter 2

In real materials, the magnetization will have a favored orientation known as magnetic easy-axis or magnetic easy-plane due to the crystal structure. Since the isotropic nature of Heisenberg interaction, there is another energy term known as *magnetocrystalline anisotropy energy* that accounts for the magnetic easy-axis and easy-plane. In the simplest case as *uniaxial magnetic anisotropy*, the anisotropy energy is given by:

$$E_A = K_u \sin^2 \theta \quad (2.8)$$

θ is the angle between the magnetization direction and the easy-axis, as shown in Figure 2.4, and the higher-order terms are neglected. When K_u is positive, the anisotropy energy will be minimized when the magnetization direction is parallel or anti-parallel to the easy-axis. When K_u is negative, then the energy will take a minimum when $\theta = \frac{\pi}{2}$ or $\frac{3\pi}{2}$, meaning the magnetization will be stable in the easy-plane perpendicular to the hard-axis.

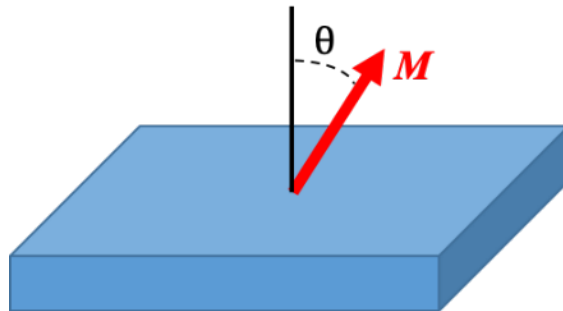


Figure 2-4: Orientation of magnetization in a magnetic thin film. The magnetic anisotropy energy determines the magnetization direction.

Apart from the magnetocrystalline anisotropy energy that arises from the crystal structure, anisotropy energy is also produced from magnetostatic energy due to the magnetic free poles appearing on the outside surfaces or the internal surfaces of an inhomogeneous magnetic material. And this shape anisotropy energy could be written as [41, 43]:

Chapter 2

$$E_S = \frac{1}{2} \sum_{i=x,y,z} N_i M_i^2 \quad (2.9)$$

Here, N_i is the demagnetization factors in the three directions as $\sum_i N_i = 4\pi$, and M_i is the magnetization projected to the x , y , and z -axis directions. In a strongly perpendicularly system with the film lying in the x - y plane, therefore, $N_x = N_y = 0$, $N_z = 4\pi$ and $M_x = M_y = 0$, $M_z = M_S$, the *effective uniaxial anisotropy energy* is then written as [51, 52]:

$$K_u^{\text{eff}} = K_u - 2\pi M_S^2 \quad (2.10)$$

And the minimal field that can drive the magnetization from out-of-plane to in-plane direction defined as the *effective uniaxial anisotropy field* H_K^{eff} is:

$$H_K^{\text{eff}} = \frac{2K_u^{\text{eff}}}{M_S} \quad (2.11)$$

When an exterior magnetic field is applied to the system, the total energy will be written as:

$$E = K_u^{\text{eff}} \sin^2 \theta - \vec{M} \cdot \vec{H} \quad (2.12)$$

In the above derivation, a single magnetized system has been assumed. However, there will exist magnetic domains where the magnetization directions are different. The boundary of these magnetic domains is called the magnetic domain walls (DW), in which the magnetization gradually rotates from the direction of one domain to another. In this work, a 180° domain wall is considered as the magnetization direction of the adjacent domains that are anti-parallel to each other. The inner structure of a DW with strong uniaxial magnetic anisotropy is determined from the competition of exchange energy and anisotropy energy, and the Hamiltonian of the system could be written as:

Chapter 2

$$H = \int d^3r \left[J(\nabla\vec{M})^2 - \frac{K_u^{\text{eff}}M_z^2}{M^2}V \right] \quad (2.13)$$

Where the first term is the exchange energy, and the second one is the effective uniaxial anisotropy energy. A boundary condition of $\vec{M}(\pm\infty) = \mp M\vec{e}_z$ and a spherical coordinate $M(\cos\varphi(x)\sin\theta(x), \sin\varphi(x)\sin\theta(x), \cos\theta(x))$ are applied, as illustrated in Figure 2.5, and the Hamiltonian is rewritten as:

$$H = \int d^3r \left[A((\partial\theta/\partial x)^2 + (\sin\theta \partial\varphi/\partial x)^2) + K_u^{\text{eff}}\sin^2\theta \right] \quad (2.14)$$

Here, A is exchange stiffness defined as JM^2/a where a is the lattice constant. Considering the stationary condition as $\frac{\partial H}{\partial\varphi} = \frac{\partial H}{\partial\theta} = 0$, the following equation sets are derived:

$$\begin{cases} (\partial^2\varphi/\partial x^2)\sin^2\theta + (\partial\varphi/\partial x)(\partial\theta/\partial x)\sin 2\theta = 0 \\ 2A(\partial^2\theta/\partial x^2) - [K_u^{\text{eff}} + A(\partial\varphi/\partial x)^2\sin 2\theta] = 0 \end{cases} \quad (2.15)$$

Since the boundary condition is $\vec{M}(\pm\infty) = \mp M\vec{e}_z$, which means $\theta(\infty) = \pi$ and $\theta(-\infty) = 0$, the solution to the above equation sets are:

$$\begin{cases} \varphi(x) = \text{const} \\ \theta(x) = 2\text{Arctan} \left[\exp\left(\frac{x}{\Delta}\right) \right] \end{cases} \quad (2.16)$$

Here, Δ is the DW width with the form of $\Delta = \sqrt{A/K_u^{\text{eff}}}$. And the DW energy has the form of

$E = 4\sqrt{AK_u^{\text{eff}}}$. With increasing exchange energy, since the adjacent moments tend to align parallel to each other, the angle difference will be smaller, and the DW is then wider. The increase of the effective uniaxial anisotropy energy will force the magnetization only to align

Chapter 2

in the easy-axis direction, and the magnetization rotation will become sharper. Thus, a narrower DW is realized.

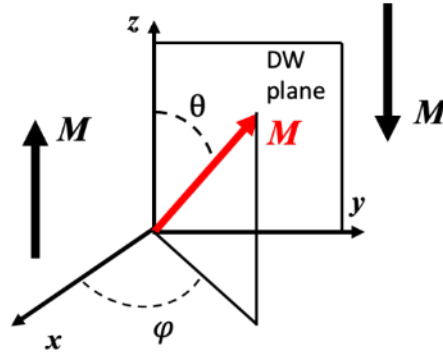
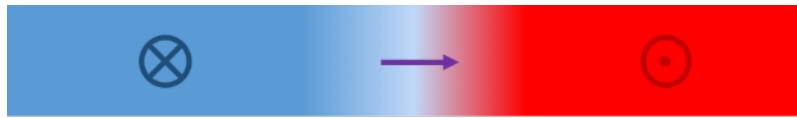


Figure 2-5: The magnetization coordinates inside a domain wall. In a DW propagating in the x -direction, the magnetization inside the DW could be described in the form $M(\cos\varphi(x)\sin\theta(x), \sin\varphi(x)\sin\theta(x), \cos\theta(x))$

In the above description of the DW profile, the magnetization inside the DW can rotate at any fixed azimuth angle φ . Two major types of DWs are defined with the difference in φ angle as shown in Figure 2.6. When $\varphi = 0, \pi$, as the magnetization inside the DW rotates in the DW plane, this kind of DW configuration is called the Néel Wall; when $\varphi = \frac{\pi}{2}$ and $\frac{3\pi}{2}$, the magnetization inside the DW rotates perpendicular to the DW plane, a Bloch Wall is formed. The selection between the Néel wall and Bloch wall configuration is determined from the competitions of energy term involved in the system. For example, in a magnetic nanowire structure, because of the shape anisotropy, the width of the wire and thickness of the film will be deterministic for the formation of Bloch wall or Néel wall configuration.



Néel Wall configuration



Bloch Wall configuration

Figure 2-6: Top view of magnetization profiles of Néel wall and Bloch wall configuration in a PMA system. The arrow in the DW region represents the magnetization direction in the center of the DW.

2.2. Magnetic dynamics and field-driven DW motion

When an exterior field is applied to a ferromagnetic system, a torque will be exerted on the magnetization, and the spin dynamics is described from the classical view as:

$$d\vec{M}(t)/dt = \gamma\vec{H}_{\text{eff}}(t) \times \vec{M}(t) \quad (2.17)$$

Here, $\vec{H}_{\text{eff}}(t)$ is derived from $\vec{H}_{\text{eff}} = \partial U / \partial \vec{M}$, where U is the total energy of the system, and γ is the *gyromagnetic ratio*. Noticing that, when the dot product of both sides with $\vec{M}(t)$ leads to vanishing on the right side of this equation, which shows the non-time variant nature of $|\vec{M}(t)| = M$.

However, the system will get its ‘memory’ of spin status, which means the tendency of the system to stay as its former magnetic status no matter the $\vec{M}(t)$ stands for the overall magnetization or just a single spin. Thus, the reaction time δt is introduced into the gyromagnetic spin dynamic equation as the retardation of dynamics due to the spin status memory:

$$d\vec{M}(t)/dt = \gamma\vec{H}_{\text{eff}}(t - \delta t) \times \vec{M}(t) \quad (2.18)$$

The expansion of the right side is then written as:

$$\vec{H}_{\text{eff}}(t - \delta t) = \vec{H}_{\text{eff}}(t) - \delta t \frac{d\vec{H}_{\text{eff}}(t)}{d\vec{M}(t)} \frac{d\vec{M}(t)}{dt} + \dots \quad (2.19)$$

With taking only the first-order approximation, the gyromagnetic equation has the following form:

$$d\vec{M}/dt = \gamma\vec{H}_{\text{eff}} \times \vec{M} + \frac{\vec{M}}{M} \times \left(\hat{\alpha} \frac{d\vec{M}}{dt} \right) \quad (2.20)$$

Chapter 2

With $\hat{a} = \delta t \gamma M \left(\frac{d\vec{H}_{\text{eff}}}{d\vec{M}} \right)$ as a dimensionless phenomenological damping tensor. If taking this tensor to be diagonal for simplicity, the gyromagnetic equation with damping term is written as [53, 54]:

$$d\vec{M}/dt = \gamma \vec{H}_{\text{eff}} \times \vec{M} + \alpha \frac{\vec{M}}{M} \times \left(\frac{d\vec{M}}{dt} \right) \quad (2.21)$$

Now the dimensionless coefficient α is called the Gilbert damping parameter. With some modifications, the familiar *Landau-Lifshitz-Gilbert equation* is derived [55]:

$$d\vec{M}/dt = \gamma \vec{H}_{\text{eff}} \times \vec{M} - \alpha \gamma \frac{\vec{M}}{M} \times (\vec{H}_{\text{eff}} \times \vec{M}) \quad (2.22)$$

The first term is known as the *Field-like torque*, which makes the magnetization vector continuously precess around the exterior field vector, and the second one known as *Damping-like torque* that helps the magnetization vector finally line up with the exterior field vector, as shown in Figure 2.7.

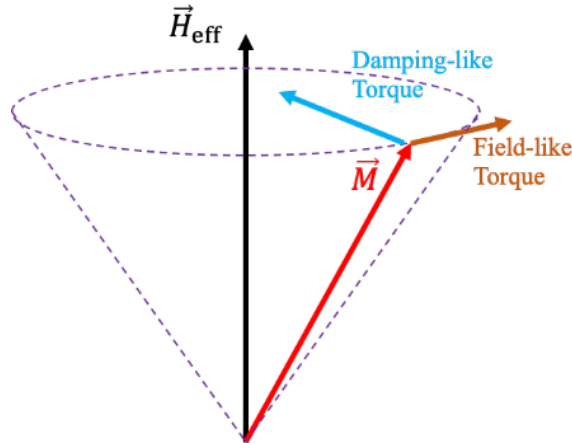


Figure 2-7: Schematic illustration of the torques exerted on the magnetization by the application of an effective magnetic field. The Field-like torque gives rise to a precession model of magnetization around the effective magnetic field. In contrast, the Damping-like torque drives the magnetization to align parallel to the effective magnetic field.

Chapter 2

For a 1-D DW in an out-of-plane magnetized wire structure with the magnetization of the form $\vec{M}(x, t) = M(\cos\varphi(x, t)\sin\theta(x, t), \sin\varphi(x, t)\sin\theta(x, t), \cos\theta(x, t))$, when an exterior field along the z -axis is applied to the system $\vec{H} = H\vec{e}_z$, by using the *LLG* equation and integrate over the entire DW region as $\theta(x, t)$ from 0 to π , the DW velocity is:

$$\frac{\partial x}{\partial t} = \Delta \frac{\gamma}{\alpha} H \quad (2.23)$$

Thus, the DW velocity will show a linear response to the exterior field application. With more extended DW width and smaller Gilbert damping parameter, under the same field application, the DW velocity will go faster.

However, the linear response to the exterior field application won't maintain when the exterior field exceeds the so-called *Walker field*. Above the Walker field, the phenomenon named *Walker breakdown* occurs as the DW can no longer sustain its configuration and a precession mode of DW motion replaces the steady motion [56]. Such a scenario is due to the magnetostatic energy by the wire structure. The total energy of DW under the application of the exterior field is written as follows:

$$\sigma = \int_{-\infty}^{\infty} \left\{ A \left(\frac{d\theta}{dx} \right)^2 + K_u^{\text{eff}} \sin^2\theta + 2\pi M^2 \sin^2\varphi \sin^2\theta - MH \cos\theta \right\} dx \quad (2.24)$$

The first and second terms are the exchange energy and uniaxial anisotropy energy, the third one is the magnetostatic energy due to the 1-D wire structure, and the fourth one is the Zeeman energy. Taking the same boundary condition for deriving the DW width in the above section, the modified DW width is then written as:

$$\Delta_0 = \Delta \times \left(1 + \frac{2\pi M^2 \sin^2\varphi}{K_u^{\text{eff}}} \right)^{-\frac{1}{2}} \quad (2.25)$$

Chapter 2

Including both the effective field and the magnetostatic energy term, the DW velocity will be in the form of:

$$v = \frac{\gamma}{\alpha} H \Delta \left[1 + \frac{\pi M^2}{K_u^{\text{eff}}} \left(1 - \sqrt{1 - \left(\frac{H}{2\pi M \alpha} \right)^2} \right) \right]^2 \quad (2.26)$$

Thus, the Walker field $H_W = 2\pi M \alpha$ is derived. Above this field, the stable solution of the DW motion will be distorted, and the azimuthal angle φ will periodically rotate from 0 to 2π with the period of:

$$T = \frac{2\pi(1 + \alpha^2)}{\gamma \sqrt{H^2 - H_W^2}} \quad (2.27)$$

And the averaged DW velocity above the Walker field is:

$$\langle v \rangle = \frac{\gamma \Delta}{\alpha} \left(H - \frac{\sqrt{H^2 - H_W^2}}{1 + \alpha^2} \right) \quad (2.28)$$

When $H \gg H_W$, the DW velocity again exhibits a linear response to the exterior field application as:

$$\langle v \rangle = \frac{\alpha \gamma \Delta}{1 + \alpha^2} H \quad (2.29)$$

The Walker breakdown has been observed in multiple ferromagnetic systems, including the out-of-plane magnetized permalloy and Co/Pt multilayers [57, 58], as shown in Figure 2.8. However, the Walker field is much larger in the latter case due to the stabilization of the Néel wall configuration by the existence of interfacial *Dzyaloshinskii-Moriya* interaction.

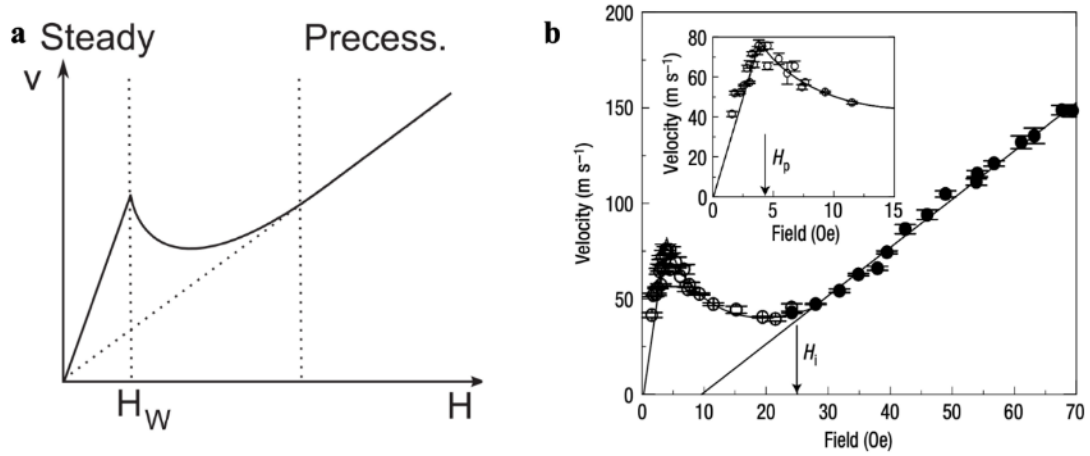


Figure 2-8: The field-driven DW motion with Walker breakdown. (a) The calculated curve of DW velocity versus the applied magnetic field from the LLG equation and (b) the measured field-induced DW motion in permalloy wires. The figure **a** and **b** are reproduced from Ref [57] and [58], respectively.

2.3. Interfacial Dzyaloshinskii-Moriya interaction in multilayer system

In the multilayer systems composed of a ferromagnetic layer (FM) on a heavy metal layer (HM), like the Co/Pt case, the DW configuration in the ferromagnetic layer is fixed as a Néel wall by the interfacial *Dzyaloshinskii-Moriya interaction* (DMI) [16, 17, 21, 27, 59]. Unlike the direct and symmetric interacting nature of Heisenberg interaction, DMI is both antisymmetric and indirect. DMI is first proposed by *Igor Dzyaloshinskii* to account for the weak ferromagnetism in anti-ferromagnets of α -Fe₂O₃ with an origin from relativistic spin-lattice and magnetic dipole interactions [19]. Later, *Toru Moriya* identified the *spin-orbit coupling* as the microscopic mechanism for this antisymmetric exchange interaction [20]. In a system dominated by DMI, the neighboring spins do not directly interact with each other, but through a third ligand, as illustrated in Figure 2.9, and has the form of:

$$H_{DMI} = -\mathbf{D}_{ij} \cdot (\mathbf{S}_i \times \mathbf{S}_j) \quad (2.30)$$

The DMI constant vector of \mathbf{D}_{ij} reflects both the direction and amplitude of DMI and is determined by the relative arrangement of both the spins and the ligand. Unlike in a system dominated by the Heisenberg interaction, where neighboring spins tend to align parallel or anti-parallel in the same direction, in a DMI dominated system, a canting state of the neighboring spins are favored.

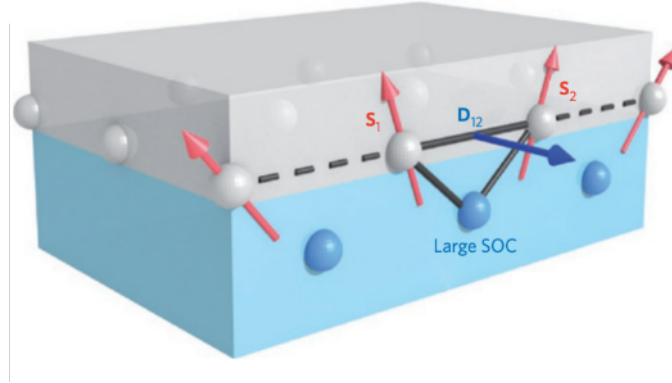


Figure 2-9: Illustration of the Dzyaloshinskii-Moriya interaction at the FM/HM interface. The canted spins in the FM layer are exchange-coupled via the atoms in the HM layer with strong spin-orbit coupling. This figure is adopted from Ref [10].

DMI in the FM/HM multilayer system arises from the symmetry breaking at the FM/HM interface. When a DW is present in the system, the magnetization is canted in the DW region, and energy density from DMI has the form [10]:

$$H_i = \sum_i \mathbf{D}_i \cdot \left(\mathbf{m} \times \frac{\partial \mathbf{m}}{\partial r_i} \right) \quad (2.31)$$

The DW orientation to the crystal axis will be deterministic for the direction of DMI vector \mathbf{D}_i here. By involving this new energy term in the DW energy in the 1-D DW model as discussed in the former section, even though the DW profile according to angle θ is still the same, the azimuth angle φ will take a value of 0 or π with the presence of DMI vector pointing in the DW plane direction. A Néel wall configuration with fixed chirality is then realized as the DW magnetization vector will always point to domain with certain magnetization, as shown in Figure 2.10.

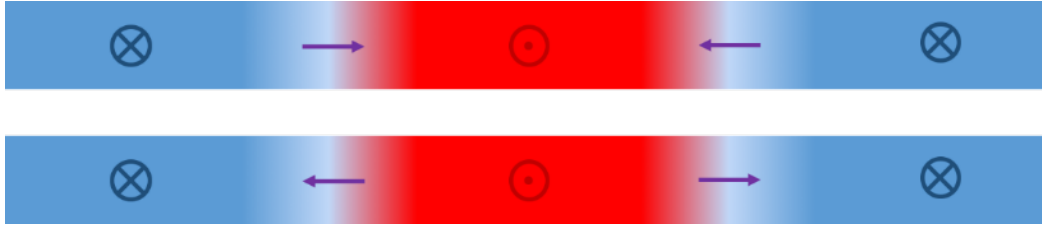


Figure 2-10: Néel walls with different fixed chirality. The interfacial fixed the magnetization inside the Néel wall configuration, always pointing to a certain domain. The above one shows a left-handed Néel wall while the bottom one shows a right-handed Néel wall.

In the field-driven DW motion case, DMI with a relatively large magnitude can effectively fix the Néel wall configuration and suppress the precession of DW, as shown in Figure 2.11. Thus, the stationary regime of DW motion is extended to a higher field, and a much larger Walker field is realized. In this case, the Walker field will have the following form [59, 60]:

$$H_W \sim \frac{\pi \alpha H_{\text{DMI}}}{2} = \frac{\pi \alpha D}{2 M_S \Delta} \quad (2.32)$$

Interestingly, in contrast to the simulation, where the precession still exists, in real experiments, the precession of DW motion above the Walker field is replaced by saturation of DW velocity. And the saturation DW velocity above the Walker field is written in the following form [59, 60]:

$$v_W = \frac{\pi}{2} \gamma_0 H_{\text{DMI}} \Delta = \frac{\pi \gamma_0 D}{2 M_S} \quad (2.33)$$

By measuring this saturation velocity combined with determining the saturation magnetization of the system, the strength of the DMI constant is successfully determined.

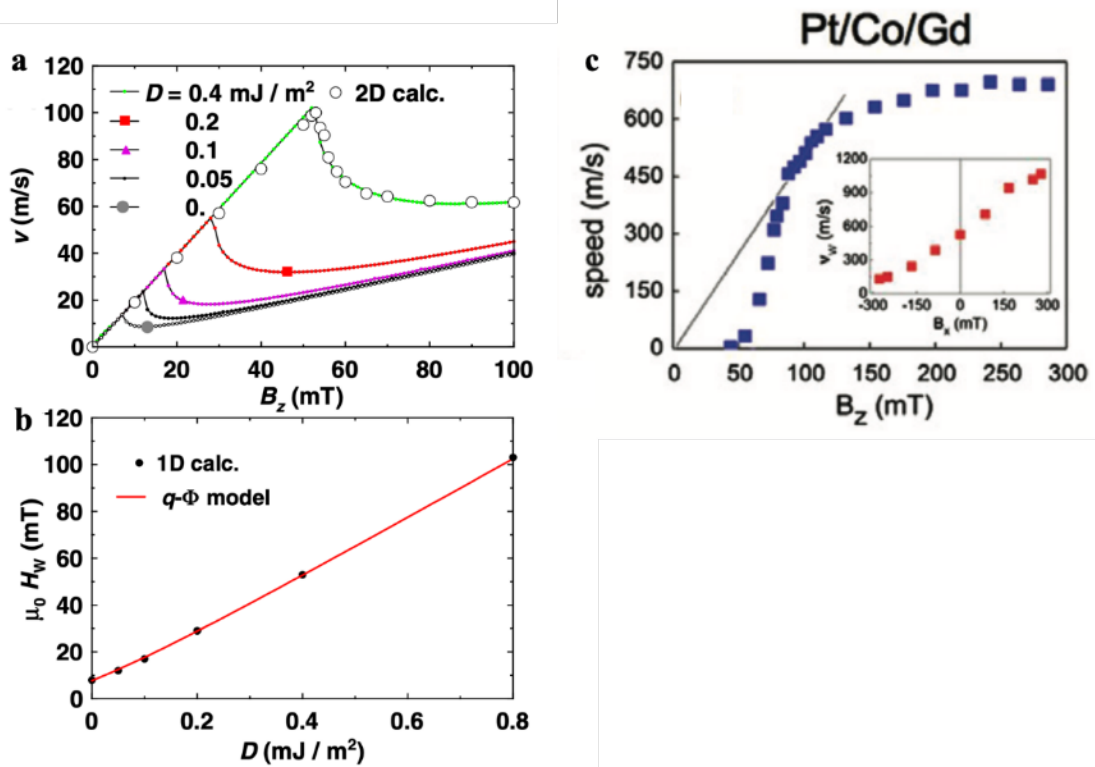


Figure 2-11: Simulation and experimental results for field-induced DW motion with the presence of DMI. With increasing the DMI constant, the Walker field increases linearly from the simulation based on the 1-D model. In real experiments of Pt/Co/Pd system, the precession of DW beyond the Walker field turns into a saturation behavior, and the saturation velocity shows a linear response to the longitudinal magnetic field. These figures are adopted from Ref [59] and [60].

2.4. Current induced domain wall motion

Even though the DW can be effectively motivated by the exterior magnetic field, the application of the exterior magnetic field not only consumes extra energy but also hampers minimizing the size of the magnetic memory devices based on DWM. By current injection, the magnetic DWs can also be effectively motivated. Two main mechanisms are responsible for this current-induced domain wall motion (CIDWM), one is the volume spin-transfer torque (STT), the other is the spin-orbit torque (SOT). The fundamental mechanism behind these two torques will be introduced, and comparisons between them will be made in the following subsections.

2.4.1. Current induced domain wall motion by spin-transfer torque

The spin-transfer current is widely used for the modification of orientations of magnetic layers in a spin valve structure (Figure 2.12). In the normal electrical current, the net spin polarization of the current is zero since the number of electrons with majority spins and minority spins are equal. When the electrical current is injected into the ferromagnetic layer with a fixed magnetization (fixed layer) in a spin valve, the number of electrons with majority spins will become more massive than the minority spins[61]. Thus, the current is spin-polarized, and a so-called spin current is generated. The polarization rate of the spin current is defined as:

$$P = \frac{\sigma_+ - \sigma_-}{\sigma_+ + \sigma_-} \quad (2.34)$$

Where the $\sigma_{+(-)}$ is the conductivity of the electrons with the majority and minority spins. When this spin current is injected into another ferromagnetic layer with different magnetization directions (free layer), the angular momentum (spins) of the electrons can be transferred to the magnetization of this layer as the *spin-transfer torque* to modify its magnetization [61-67].

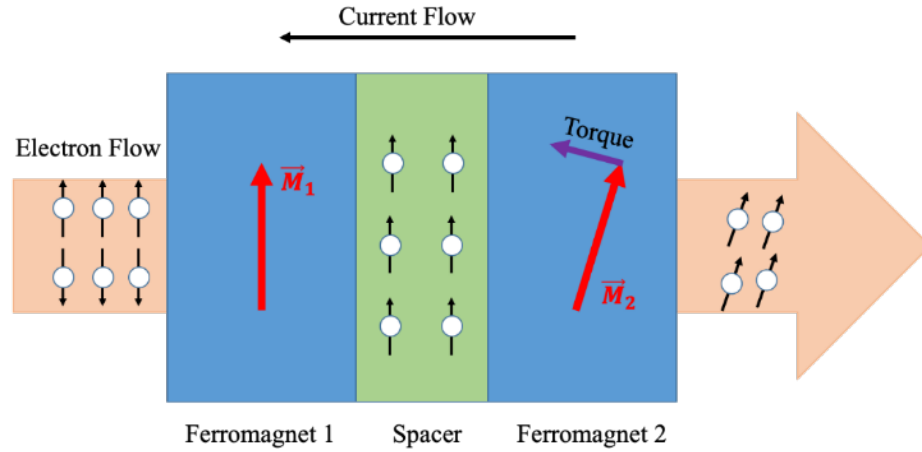


Figure 2-12: Schematic illustration of spin-transfer torque in a spin valve structure. When the current is injected from right to left, electron flow from left to right is injected through the spin valve. The electrons with equilibrium majority and minority spins will get polarized after passing through the first ferromagnetic layer. A torque is exerted by this spin current on the second ferromagnetic layer with a different magnetization to the first one.

The magnetization configuration inside a DW naturally forms a spin-valve structure, and it won't be surprising that the electrical current injection can motivate the DW through STT. When the spin-polarized current is injected through the DW, the angular momentum of the electrons is transferred to the local magnetization inside the DW adiabatically, and the DW is then motivated in the electron flowing direction. The LLG equation with the inclusion of STT has the following form [14, 67-69]:

$$d\vec{m}/dt = \gamma\vec{H}_{\text{eff}} \times \vec{m} - \alpha\gamma\vec{m} \times (\vec{H}_{\text{eff}} \times \vec{m}) - (\vec{u} \cdot \vec{\nabla})\vec{m} \quad (2.35)$$

Here, $\vec{m} = \frac{\vec{M}}{M}$ is the unit direction vector of the magnetization. The third term in the above equation is the adiabatic STT term. \vec{u} is the spin drift velocity vector $\vec{u} = \vec{j}Pg\mu_B/(2eM_S)$ with \vec{j} the electron motion vector, P the polarization rate of current, g the Landé g -factor, and μ_B

Chapter 2

the Bohr magneton constant, e the electron charge, and M_S the saturation magnetization of the material.

Apart from the adiabatic spin-transfer process, there also exists the non-adiabatic momentum transfer process. The electrons with spins do not merely go across the DW region but will be reflected due to the angle difference between electron spins and local magnetic moments. The DW will be pushed by these electrons and also moves in the electron flow direction. This non-adiabatic STT possess a damping-like torques nature, and the modified LLG equation, including the non-adiabatic STT term, is written as follows [47, 48, 63, 69, 70]:

$$d\vec{m}/dt = \gamma\vec{H}_{\text{eff}} \times \vec{m} - \alpha\gamma\vec{m} \times (\vec{H}_{\text{eff}} \times \vec{m}) - (\vec{u} \cdot \vec{\nabla})\vec{m} + \beta\vec{m} \times [(\vec{u} \cdot \vec{\nabla})\vec{m}] \quad (2.36)$$

The fourth term is the non-adiabatic STT term, and β is the dimensionless non-adiabatic STT coefficient resembling the Gilbert damping parameter α .

Taking a typical DW profile with parameters of DW position q and the magnetization angle φ , the LLG equation can then be rewritten in the following form:

$$\begin{cases} \dot{\varphi} + \frac{\alpha\dot{q}}{\Delta} = \gamma H_a + \frac{\beta u}{\Delta} \\ \frac{\dot{q}}{\Delta} - \alpha\dot{\varphi} = \frac{1}{2}\gamma H_K \sin 2\varphi + \frac{u}{\Delta} \end{cases} \quad (2.37)$$

Here, H_K is the shape anisotropy field, u is the STT velocity, and H_a is the applied exterior field. At a zero exterior field condition, the above equation sets can be simplified as:

$$\begin{cases} \dot{\varphi} = \frac{\alpha}{1 + \alpha^2} \left[\frac{\beta - \alpha u}{\alpha \Delta} - \frac{\gamma H_K}{2} \sin 2\varphi \right] \\ \dot{q} = \frac{\beta u}{\alpha} - \frac{\Delta \dot{\varphi}}{\alpha} \end{cases} \quad (2.38)$$

If a non-zero β is present, as soon as the current is injected into the system, the DW begins to move. When the injected current density is small, as $|u| < \frac{\pi\gamma H_K \Delta \alpha}{8|\beta - \alpha|}$, the DW velocity exhibits a

Chapter 2

linear dependence on the injected current density as $\dot{q} = \frac{\beta u}{\alpha}$ in the steady motion ($\dot{\phi} = 0$) but has no relationships with the DW width. By comparison with the field-driven DW motion case, the STT terms are introduced into the LLG equation with an equivalent field of $H_{\text{STT}} = \frac{\beta u}{\gamma \Delta}$. With further increase in injected current density as increasing u , the Walker breakdown behavior also occurs for the STT-driven CIDWM case, as shown in Figure 2.13.

However, if there exists no non-adiabatic torque, by putting a zero-value β into the above equation sets leads to:

$$\begin{cases} \dot{\phi} = \frac{\alpha}{1 + \alpha^2} \left[-\frac{u}{\Delta} - \frac{\gamma H_K}{2} \sin 2\phi \right] \\ \dot{q} = -\frac{\Delta \dot{\phi}}{\alpha} \end{cases} \quad (2.40)$$

The steady motion region of CIDWM no longer exists, since when $\dot{\phi} = 0$, \dot{q} is also zero. Thus, only the precession motion will exist. By solving the first equation and put it back to the second one, the averaged velocity has the form:

$$\langle \dot{q} \rangle \propto \sqrt{\left(\frac{u}{\Delta}\right)^2 - \left(\frac{\gamma H_K}{2}\right)^2} \quad (2.41)$$

As indicated from the above equation, the DW won't move until the spin drift velocity is over a certain value, which means there exist an intrinsic threshold current density [14, 61, 68, 69]. Recalling that $u = JPg\mu_B/(2eM_S)$, the threshold current density is then proportional to the shape anisotropy term and DW width $J_{\text{th}} \propto \Delta H_K M_S$. Indeed, this shape anisotropy term determines the energy difference between the Néel wall and Bloch wall. Thus, such an intrinsic threshold can be diminished when the two types of DW has the same energy [69, 71].

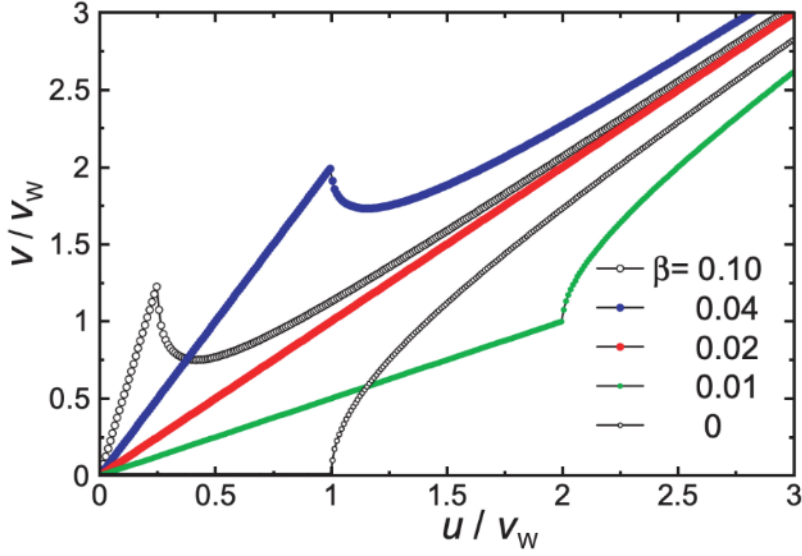


Figure 2-13: Simulation results of CIDWM velocity as a function of spin drift velocity. With increasing the non-adiabatic STT coefficient β , the slope of DW velocity to the spin drift velocity u is varied with a linear dependence on β . When $\beta = 0$, there exist an intrinsic threshold that is not observed when the non-adiabatic STT is present. This figure is adopted from Ref [68].

In conclusion, when a polarized spin current is injected through the DW, the spin-transfer torque with both adiabatic and non-adiabatic nature will be exerted on the DW, and a CIDWM in the electron flowing direction is realized. In the adiabatic STT case, there exists an intrinsic threshold current density, while in the non-adiabatic STT case, no intrinsic pinning exists. With the inclusion of both STTs, the CIDWM shows a much resemblance to the field-driven DW case under the application of an effective field of $H_{\text{STT}} = \frac{\beta u}{\gamma \Delta}$. The contrast difference is that the CIDWM has no dependence on DW width, and the non-adiabatic STT coefficient β dominates the velocity.

2.4.2. Current induced domain wall motion by spin-orbit torque

The spin-orbit torque, as recognized by its name, originates from the spin-orbit coupling (SOC) and is widely found in the heterostructures consisted of the FM layer and HM layer [3, 16, 17, 21, 59, 72-78]. The electrical current injected in the FM/HM system is converted into spin current either through the *inverse spin galvanic effect* (ISGE) due to inversion symmetry breaking at the FM/HM interface or the bulk *spin Hall effect* (SHE) in the HM layer. Such spin current is further absorbed by the FM layer and can well manipulate the magnetization of the FM layer [16, 75, 77].

Spin galvanic effect, a name originating from the analogy to the galvanic cell, describes the generation of electrical current from spin polarization and is first observed in an asymmetrically confined two-dimensional electron gas in the GaAs quantum well [79]. When a steady spin polarization is introduced to the system, the different populations in the majority and minority spin sub-bands, together with a shift of both sub-bands in momentum space because of the inversion symmetry breaking, leads to an inherent asymmetry in the spin-flip scattering events between the two sub-bands and in turn an electrical current is generated [73, 79]. Inversely, an injection of electrical current and scattering-induced redistribution of carriers in the Fermi surface will give rise to a uniform non-equilibrium spin density [80]. At the FM/HM interface, where the *Rashba* type spin-orbit coupling exists, an electrical current in one direction will give rise to the accumulation of spin current with the polarization direction orthogonal to the electrical current injection direction [77, 78, 81]. Figure 2.14 gives a schematic illustration of the above mechanisms.

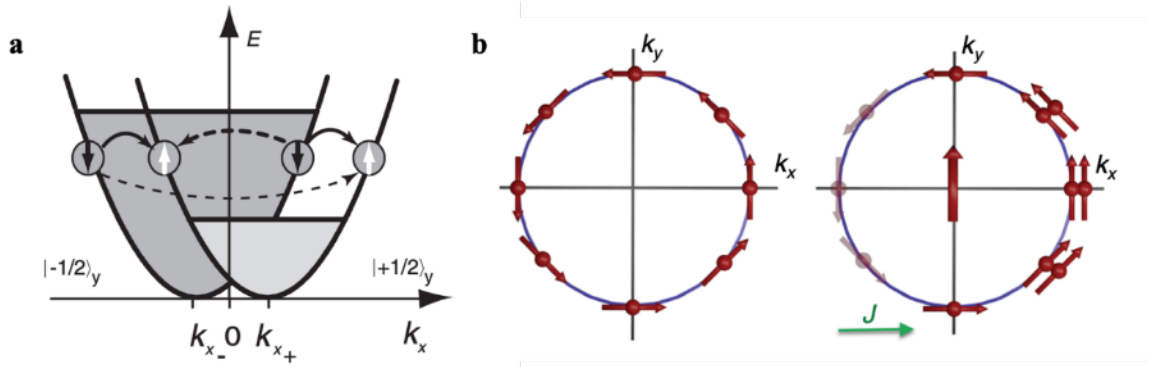


Figure 2-14: Microscopic origin of the spin galvanic effect and inverse spin galvanic effect. (a) The injection of the non-equilibrium spin current into the system will give rise to the splitting of sub-bands occupied by electrons with majority spins and minority spins in the k -space. The spin-flip process of electrons between both subbands indicated by the arrow causes an asymmetric occupation of both subbands. Thus, a current flow is generated. (b) The electrical current injection into the Rashba type spin texture with zero net spin polarization causes a non-equilibrium redistribution of eigenstate, and a non-zero spin density is generated due to broken inversion symmetry of the spin texture. This figure is adopted for Ref [73].

The *Spin Hall effect* borrows the physics and mechanisms directly from the *anomalous Hall effect* (AHE) [82-85]. Both effects originate from the relativistic spin-orbit interaction, while AHE correlates it with the charge degrees of freedom, and SHE associates both the charge and spin degrees of freedom. As illustrated in Figure 2.15, in AHE, when the electrical current is injected into the ferromagnetic system, a transverse polarized electrical current will be created because of the population difference of electrons with the majority and minority spins. In SHE, the injection of electrical current into heavy metals gives rise to a pure transverse spin current with the polarization direction orthogonal to both the spin current and electrical current direction. In a system with SHE, there also exists the *inverse spin Hall effect*, as the pure spin current injection will give rise to a transverse electrical current [86, 87].

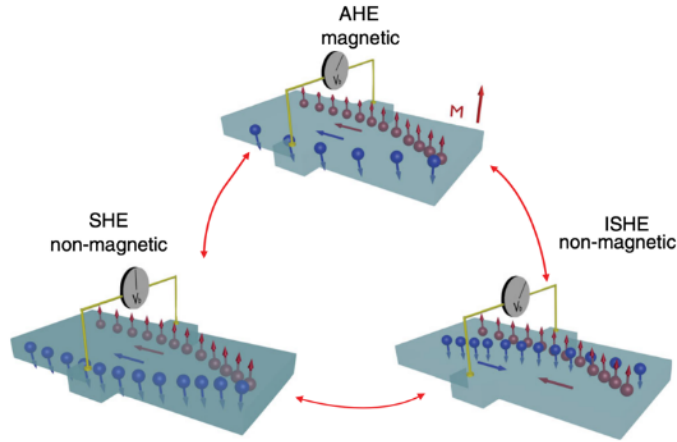


Figure 2-15: Illustration of the anomalous Hall effect, spin Hall effect, and inverse spin Hall effect. When the electrical current is injected into the magnetic material, the electrons with majority spins and minority spins will be deflected and accumulated at the different edge with different amounts, which in turn gives rise to an AHE voltage. The SHE shows an electrical current injected into a non-magnetic system possessing strong spin-orbit coupling results in a spin accumulation at each end of the film but with a zero electrical voltage. The ISHE shows a spin current injected in the longitudinal direction gives rise to a voltage in the transverse direction. This figure is adopted for Ref [73].

Resembling the AHE, the origin of SHE can also be attributed to two categories as intrinsic and extrinsic [73, 88]. Intrinsic SHE results from the band splitting due to strong spin-orbit coupling. Such band splitting gives rise to an effective magnetic field from the *Berry phase* [83, 85], and a spin-dependent scattering effect akin to the normal Hall effect happens. The extrinsic mechanisms of SHE are the spin-dependent scattering of electrons by the impurities through spin-orbit interaction and can be categorized of skew scattering and side-jump mechanisms [84]. No matter the intrinsic or extrinsic origin, the spin current generated by SHE can be described as:

$$\vec{J}_s = \theta_{SH} \vec{\sigma} \times \vec{J} \quad (2.42)$$

Where θ_{SH} is the spin Hall angle describing the efficiency of charge to spin conversion, and $\vec{\sigma}$ is the spin polarization unit vector.

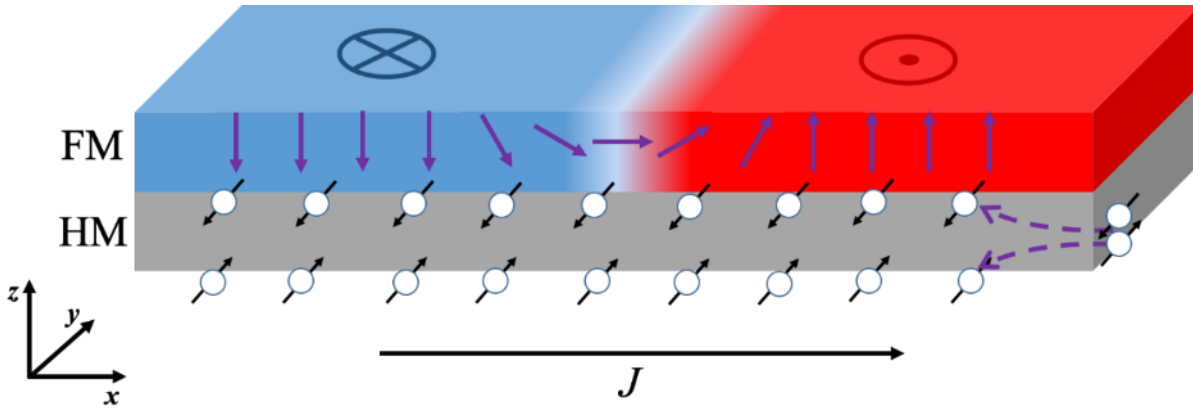


Figure 2-16: Schematic illustration of spin current generated from the SHE of the HM layer in the FM/HM system. According to the description of Eq.2.42, the spin current with the polarization direction along the y -axis is generated from an in-plane current injection and absorbed by the adjacent FM layer, which in turn gives rise to a Damping-like torque on the magnetization.

Since each electron can only carry the spins of $\frac{1}{2}$, the spin current generated from the traditional way as injecting electrical current through ferromagnetic materials is limited [76]. However, in the spin current generated by spin-orbit torque, there exists no such limit, and the only deterministic parameter is the strength of spin-orbit coupling. Thus, a following large torque will be exerted on the magnetic moments. In real experiments of CIDWM by SOT, the DW velocity is 1 or 2 orders larger than in the STT-driven CIDWM case. For example, in the Co/Pt heterostructure system, the SOT-driven CIDWM velocity can reach ~ 300 m/s [16, 17, 21]. In contrast, in the solely Co layer, the STT-driven CIDWM velocity is usually ~ 20 m/s [71, 89].

Chapter 2

The SOT exerted on DW from both the ISGE and SHE in the FM/HM heterostructure are written with the following forms [90]:

$$\begin{aligned}\vec{\tau}_{\text{ISGE}} &= -\gamma\vec{m} \times \vec{H}_R + \gamma\beta\vec{m} \times (\vec{m} \times \vec{H}_R) \\ \vec{\tau}_{\text{SH}} &= \gamma\vec{m} \times (\vec{m} \times \vec{H}_{\text{SH}})\end{aligned}\quad (2.43)$$

Here, \vec{H}_R is the effective field from the Rashba effect and has the form: $\vec{H}_R = \frac{\alpha_R P J}{\mu_B M_s} \vec{e}_y$, α_R is the strength of Rashba spin-orbit coupling, and P is the polarization ratio; \vec{H}_{SH} is the effective field of SHE and has the form: $\vec{H}_{\text{SH}} = \frac{\mu_B \theta_{\text{SH}} J}{\gamma e M_s t_{\text{FM}}} \vec{e}_y$, t_{FM} is the thickness of the ferromagnetic layer. The torque generated from ISGE has both the Field-like and Damping-like term, while the SHE torques only have the Damping-like term [59, 90].

Unlike the STT-driven CIDWM, where the DW moves in the electron flowing direction regardless of DW configuration, in the SOT-driven CIDWM, the DW moves in the current flowing direction and has a very strong dependence on the DW configuration [17, 59, 74, 91]. As illustrated by both experiments and simulation, only the Néel type DW can be effectively motivated by the damping-like SOT. In FM/HM structures, with the presence of interfacial DMI, the Néel wall configuration will be fixed, as shown in Figure 2.16. Implementing the DMI and SOT from the SHE and ignoring the STT term since DW velocity in SOT case is much larger, taking a typical Néel DW profile with parameters of DW position q and the magnetization angle φ , the dynamic description of the CIDWM can be written as:

$$\begin{cases} \dot{\varphi} + \frac{\alpha \dot{q}}{\Delta} = \gamma H_{\text{SHE}} \cos \varphi \\ \frac{\dot{q}}{\Delta} - \alpha \dot{\varphi} = \gamma H_{\text{DMI}} \sin \varphi \end{cases}\quad (2.44)$$

Taking the steady-state as $\dot{\varphi} = 0$, the DW velocity dominated by chiral SOT can be described as:

Chapter 2

$$v = \Delta\gamma \frac{H_{\text{SHE}}H_{\text{DMI}}}{\sqrt{H_{\text{SHE}}^2 + \alpha^2 H_{\text{DMI}}^2}} = \frac{v_D}{\sqrt{1 + \left(\frac{J_D}{J}\right)^2}} \quad (2.45)$$

Here, $v_D = \gamma\Delta H_{\text{DMI}} = \frac{\gamma\pi D}{M_S}$, and $J_D = 2\alpha t_{\text{FM}}eD/(\hbar\theta_{\text{SH}}\Delta)$. With increasing the injected current density, the DW velocity will increase and finally saturates at v_D as the DW configuration turning from the Néel wall to the Bloch wall (Figure 2.17). Interestingly, the final velocity has nothing to do with the SOT term but is only determined by the DMI and DW width [59, 60].

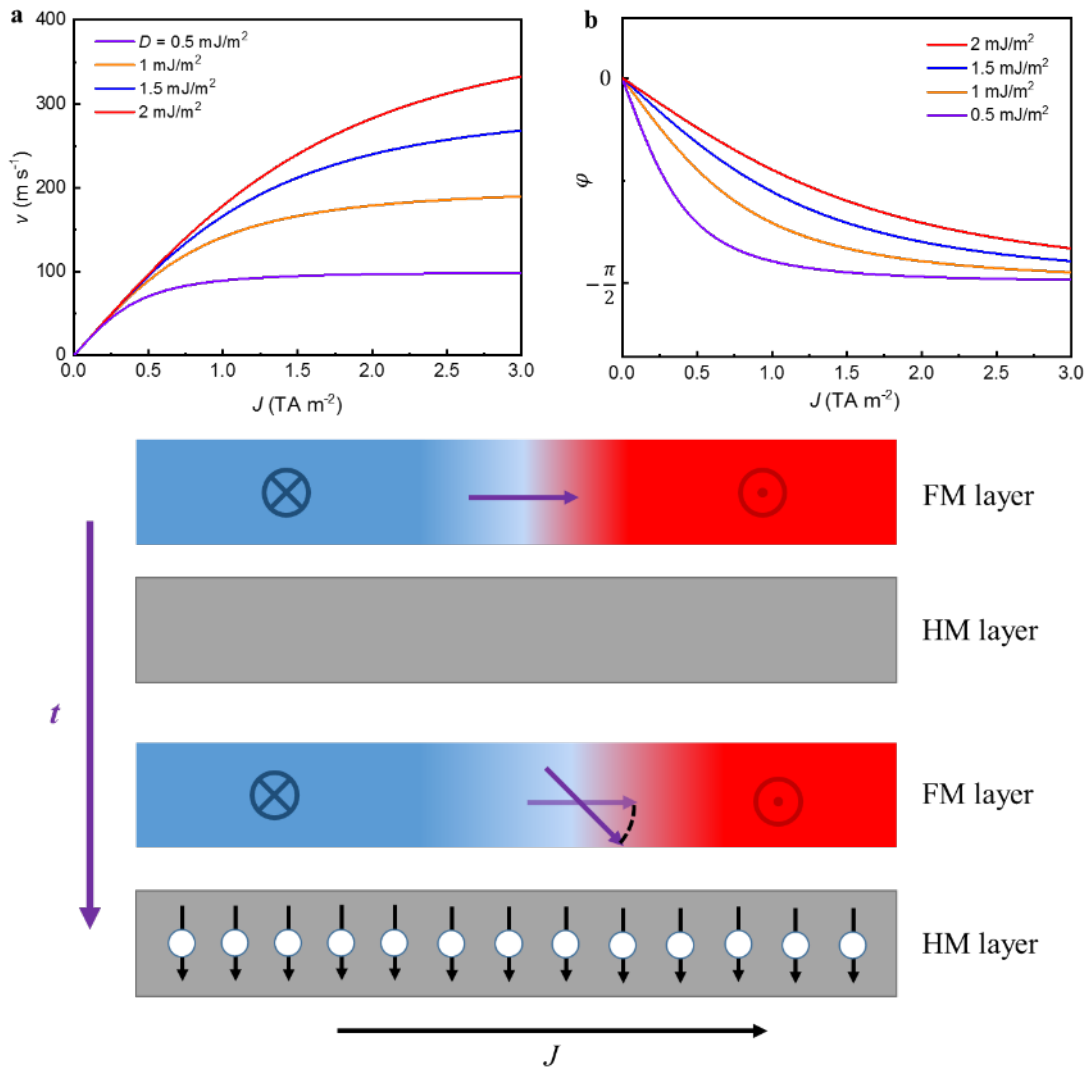


Figure 2-17: SOT-driven DWM with the presence of interfacial DMI. The DW velocity plotted as a function of the injected current density shows a saturating behavior, and the saturation velocity increases with increasing the DMI. In the very tiny current density region, the curves overlap each other, indicating that at the vicinity of zero current density, the DW velocity is irrelevant to the DMI. In the steady motion of the SOT-driven chiral DW, the DW angle will tilt from the initial state. With increasing the injected current density, the azimuthal angle φ turns from π (0) to $\frac{\pi}{2}$ ($\frac{3\pi}{2}$), the final saturation indicates a DW configuration of a Bloch wall instead of the initial Néel wall.

Chapter 2

When an in-plane magnetic field in the longitudinal direction is applied to the system, the modification could be viewed as varying the DMI effective field. A linear relationship is usually observed when the DW velocity at a fixed current density is plotted against the longitudinal field. When the longitudinal field application cancels the DMI effective field, the DW velocity will turn to zero as a Bloch wall configuration is formed, and no SOT can be exerted on the DW [17, 21, 59]. In the vicinity of $H_{\text{DMI}} \sim 0$, the velocity is proportional to H_{DMI} , regardless of the current density [59]. By increasing the injected current density, the region of the linear relationship between the DW velocity and H_{DMI} expands, and the slope is fixed at $\Delta\gamma$.

In conclusion, in the FM/HM systems inbounded with profound spin-orbit interactions, the Néel type DW fixed by interfacial DMI can be efficiently motivated by SOT generated from both SHE and ISGE. Unlike in the STT-driven CIDWM case, where the DW moves in the electron flowing direction and is independent of the DW configuration, the SOT-driven CIDWM moves in the current flowing direction and relies tightly on the DW configuration as both the DW type and DW width. The collaborative contributions of SOT, DMI, and K_u^{eff} (through DW width) to the SOT-driven CIDWM makes it a complicated magnetic dynamical phenomenon but with a great potential for improvement.

2.4.3. Current induced domain wall motion in the synthetic anti-ferromagnet structure

Recently, spintronics based on anti-ferromagnets (AFM) has attracted more and more attention since its potential to vastly reduce energy consumption and increase the device density and velocity. The anti-ferromagnetic materials have advantages over the ferromagnets, including but not limited to: robustness against exterior magnetic field perturbation, elimination of stray fields, ultrafast magnetic dynamics, and capability of generating large transport signals [92]. Synthetic anti-ferromagnets (SAF), consisting of two ferromagnetic layers antiferromagnetically exchange-coupled through a spacer layer by the long-range oscillatory RKKY interaction, shares the similar magnetic properties with AFM and can be well optimized for the requirements of different devices and measurement methods [12, 49, 50, 93]. Former research has observed the ultra-fast CIDWM in the SAF structure with distinct features compared to the CIDWM in FM/HM structures [12, 93]. In the following section, the mechanism of the CIDWM in the SAF structure will be discussed, and the additional driving force of the exchange coupling torque resulting from the exchange coupling between two magnetic sub-layers will be introduced.

2.4.3.1 DW configuration, energy, and dynamics in SAF structure

In a typical SAF structure, the magnetizations in the two magnetic sub-layers align antiparallely to each other. When the two magnetic sub-layers are identical, just like in the AFM case, the total dipole energy term will be eliminated. Thus, there exists no net shape anisotropy term, and the energy difference between the Bloch wall and Néel wall goes to zero [12]. Because of the strong interlayer exchange coupling, the DW position and the magnetic profile inside the DWs will be locked up in both layers. In a typical structure as used through this thesis as SAF structure with two magnetic sub-layers of Co/Ni/Co with PMA and exchange-coupled through the Ru spacer on top of the Pt layer, the interfacial DMI from the bottom Co/Pt interface will induce two coupled Néel wall configuration with the same chirality

and width, as shown in Figure 2.18. With the presence of the interlayer exchange interaction, the energy density of two exchange-coupled DW will be written as follows:

$$\begin{aligned}
 w = & 2A_L t_L \frac{\sin^2 \theta_L}{\Delta^2} + t_L (K_L^{\text{eff}} + K_L^u \cos^2 \varphi_L) \sin^2 \theta_L - M_L H_L^{\text{lg}} \cos \varphi_L \sin \theta_L + 2A_U t_U \frac{\sin^2 \theta_U}{\Delta^2} \\
 & + t_U (K_U^{\text{eff}} + K_U^u \cos^2 \varphi_U) \sin^2 \theta_U - M_U H_U^{\text{lg}} \cos \varphi_U \sin \theta_U \\
 & - 2J_{\text{ex}} [\sin \theta_L \sin \theta_U \cos(\varphi_L - \varphi_U) + \cos \theta_L \cos \theta_U] \quad (2.45)
 \end{aligned}$$

Where the subscripts of U and L correspond to the upper and lower magnetic sub-layer, A_i is the exchange stiffness, t_i is the layer thickness, K_i^{eff} is the effective anisotropy energy, K_i^u is the shape anisotropy energy (In each sub-layer, they still possess a ferromagnetic nature. Thus, the shape anisotropy of individual layer still exists), θ_i and ψ_i are the corresponding azimuthal angles, M_i is the saturation magnetization, H_i^{lg} is the longitudinal effective magnetic field, including the DMI effective field of each layer, J_{ex} is the exchange coupling constant. The total energy combines the DW energy of each layer and the exchange coupling energy between them. The effective field is derived from the equation of $H_{\text{eff}}^i = \frac{\partial w}{\partial M_i}$.

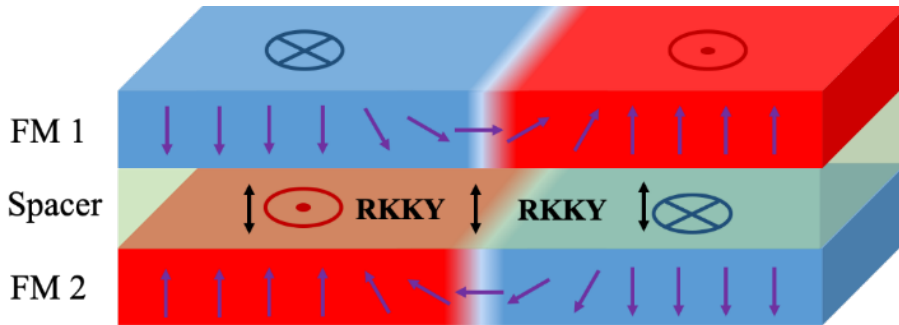


Figure 2-18: Antiferromagnetically coupled Néel DWs in the SAF structure. Since the two magnetic sublayers are tightly antiferromagnetically coupled, the magnetization configurations inside the DWs are mirrored to each other. Thus, the same DW width in two sublayers is assumed.

When the spin current generated from the SHE in the bottom Pt layer is injected into the upper SAF structure, the SOT exerted on the two sublayers will be different. The SHE spin

Chapter 2

current will experience the spin depolarization process as going through the lower FM layer and Ru layer, so the effective spin Hall field exerted on the two sub-layers have the following relationships:

$$H_{\text{SHE}}^U = H_{\text{SHE}}^L \exp\left(-\frac{t_L}{\lambda_L} - \frac{t_S}{\lambda_S}\right) \quad (2.46)$$

Where λ_L is the spin decoherence length of the lower magnetic layer, and λ_S is the spin diffusion length of the spacer layer. The LLG equation describing the individual layer driving by SOT is then written as:

$$\begin{aligned} \frac{\partial \mathbf{M}_i}{\partial t} = & -\gamma \mathbf{M}_i \times \mathbf{H}_i^{\text{eff}} + \frac{\alpha_i}{m_i} \mathbf{M}_i \times \frac{\partial \mathbf{M}_i}{\partial t} - b_j^i \mathbf{M}_i \times \mathbf{M}_i \times \frac{\partial \mathbf{M}_i}{\partial t} - \beta_i b_j^i \mathbf{M}_i \times \frac{\partial \mathbf{M}_i}{\partial x} \\ & + H_{\text{she}}^i \mathbf{M}_i \times \mathbf{M}_i \times \hat{y} \end{aligned} \quad (2.47)$$

By integrating with the DW profile of both layers and the dynamic description of the CIDWM in SAF structure based on the DW position $q(x, t)$ and azimuthal angle of DW magnetization $\varphi_i(x, t)$ are written as:

$$\begin{aligned} \dot{q} = & \frac{\alpha_L \alpha_U}{\alpha_U M_L (1 + \alpha_L^2) + \alpha_L M_U (1 + \alpha_U^2)} \left[-M_L \left(\frac{1}{\alpha_L} + \beta_L \right) u_L \right. \\ & - M_U \left(\frac{1}{\alpha_U} + \beta_U \right) u_U \\ & \mp \frac{\gamma \Delta M_L}{\alpha_L} \left\{ \frac{H_L^k}{2} \sin 2\varphi_L - \frac{\pi}{2} H_L^{\text{lg}} \sin \varphi_L \right. \\ & \left. \left. - \frac{2J_{\text{ex}}}{M_L} \sin(\varphi_L - \varphi_U) + \frac{\alpha_L \pi H_L^{\text{SH}}}{2} \cos \psi_L \right\} \right. \\ & \left. \pm \frac{\gamma \Delta M_U}{\alpha_U} \left\{ \frac{H_U^k}{2} \sin 2\varphi_U - \frac{\pi}{2} H_U^{\text{lg}} \sin \varphi_U \right. \right. \\ & \left. \left. - \frac{2J_{\text{ex}}}{M_U} \sin(\varphi_U - \varphi_L) + \frac{\alpha_U \pi H_U^{\text{SH}}}{2} \cos \varphi_U \right\} \right] \end{aligned} \quad (2.48)$$

$$\begin{aligned}
 \dot{\varphi}_L = & \pm \frac{1}{\Delta} \frac{\alpha_U}{\alpha_U M_L (1 + \alpha_L^2) + \alpha_L M_U (1 + \alpha_U^2)} \left[-M_L \left(\frac{1}{\alpha_L} + \beta_L \right) u_L \right. \\
 & - M_U \left(\frac{1}{\alpha_U} + \beta_U \right) u_U \\
 & \mp \frac{\gamma \Delta M_L}{\alpha_L} \left\{ \frac{H_L^k}{2} \sin 2\varphi_L - \frac{\pi}{2} H_L^{\text{lg}} \sin \varphi_L - \frac{2J_{\text{ex}}}{M_L} \sin(\varphi_L - \varphi_U) \right. \\
 & \left. + \frac{\alpha_L \pi H_L^{\text{SH}}}{2} \cos \varphi_L \right\} \\
 & \pm \frac{\gamma \Delta M_U}{\alpha_U} \left\{ \frac{H_U^k}{2} \sin 2\varphi_U - \frac{\pi}{2} H_U^{\text{lg}} \sin \varphi_U - \frac{2J_{\text{ex}}}{M_U} \sin(\varphi_U - \varphi_L) \right. \\
 & \left. + \frac{\alpha_U \pi H_U^{\text{SH}}}{2} \cos \varphi_U \right\} \left] + \frac{\gamma}{\alpha_L} \left[\frac{H_L^k}{2} \sin 2\varphi_L - \frac{\pi}{2} H_L^{\text{lg}} \sin \varphi_L \right. \right. \\
 & \left. \left. - \frac{2J_{\text{ex}}}{M_L} \sin(\varphi_L - \varphi_U) \right] \pm \frac{u_L}{\alpha_L \Delta} \right.
 \end{aligned} \tag{2.49}$$

$$\begin{aligned}
 \dot{\varphi}_U = & \mp \frac{1}{\Delta} \frac{\alpha_L}{\alpha_U M_L (1 + \alpha_L^2) + \alpha_L M_U (1 + \alpha_U^2)} \left[-M_L \left(\frac{1}{\alpha_L} + \beta_L \right) u_L \right. \\
 & - M_U \left(\frac{1}{\alpha_U} + \beta_U \right) u_U \\
 & \mp \frac{\gamma \Delta M_L}{\alpha_L} \left\{ \frac{H_L^k}{2} \sin 2\varphi_L - \frac{\pi}{2} H_L^{\text{lg}} \sin \varphi_L - \frac{2J_{\text{ex}}}{M_L} \sin(\varphi_L - \varphi_U) \right. \\
 & \left. + \frac{\alpha_L \pi H_L^{\text{SH}}}{2} \cos \varphi_L \right\} \\
 & \pm \frac{\gamma \Delta M_U}{\alpha_U} \left\{ \frac{H_U^k}{2} \sin 2\varphi_U - \frac{\pi}{2} H_U^{\text{lg}} \sin \varphi_U - \frac{2J_{\text{ex}}}{M_U} \sin(\varphi_U - \varphi_L) \right. \\
 & \left. + \frac{\alpha_U \pi H_U^{\text{SH}}}{2} \cos \varphi_U \right\} \left] + \frac{\gamma}{\alpha_U} \left[\frac{H_U^k}{2} \sin 2\varphi_U - \frac{\pi}{2} H_U^{\text{lg}} \sin \varphi_U \right. \right. \\
 & \left. \left. - \frac{2J_{\text{ex}}}{M_U} \sin(\varphi_U - \varphi_L) \right] \pm \frac{u_U}{\alpha_U \Delta} \right.
 \end{aligned} \tag{2.50}$$

Chapter 2

Compared to the former ferromagnetic case, the additional term $\frac{2J_{\text{ex}}}{M_i} \sin(\varphi_U - \varphi_L)$ originating from the exchange coupling shows up. This term is called the exchange coupling torque, which is the deterministic driving force responsible for the ultrafast DW velocity in the SAF structure. Due to the oscillatory nature of the RKKY exchange coupling, the spacer thickness will be crucial for the DW velocity as well as the relative magnitude of the saturation magnetization in both magnetic sub-layers. The more identical of the two sub-layers, the faster the DW velocity will be.

The complicated dependence of the various magnetic parameters of both magnetic sub-layers results in the delicate nature of the CIDWM and sensitive responses to any modification on the magnetic properties. When the longitudinal field is applied to the system, instead of a linear response, a peaked curve of the DW velocity is observed since the DW structure in both layers will be modified [12, 93]. The more identical of the two sub-layers in SAF structure is, the less difference of the longitudinal field dependence of DW velocity between an up/down or down/up DW are seen, as shown in Figure 2.19.

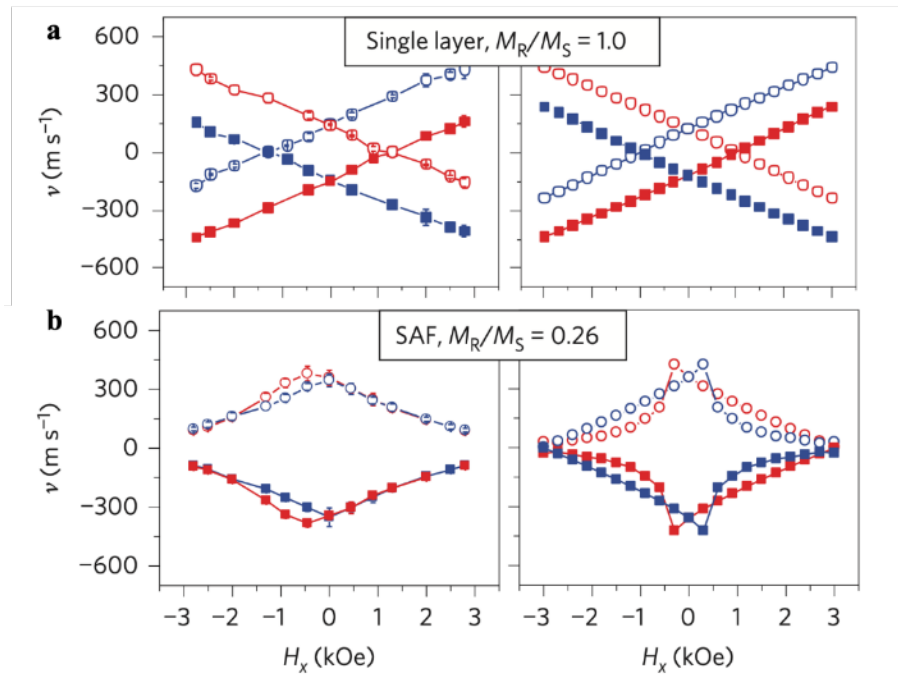


Figure 2-19: The current-induced DW velocity in the FM/HM case and SAF case plotted as a function of the exterior longitudinal magnetic field. The red and blue symbol indicates the DW in a $\uparrow\downarrow$ and $\downarrow\uparrow$ domain configuration, respectively. In the SAF case, the difference between $\uparrow\downarrow$ and $\downarrow\uparrow$ DWs become smaller. Since in a perfect AFM case, the zero magnetization results in no difference between \uparrow and \downarrow domains and thus the DW. This figure is adopted for Ref [12].

2.4.3.2 Exchange coupling torque

When the SHE spin current is injected into the system, the motion of DW in both layers will give rise to a DW magnetization rotating from the equilibrium direction. Once the two DWs' magnetizations no longer antiparallelly aligned to each other, the exchange coupling torque (ECT) is exerted on both DW magnetic moments [3, 12, 24, 93]. From the exchange coupling effective field, which is in the direction orthogonal to the magnetization direction, the exchange coupling torque is perpendicular to the magnetization plane since the torque has the form as $-\gamma \mathbf{M}_i \times \mathbf{H}_i^{\text{eff}}$, as shown in Figure 2.20.

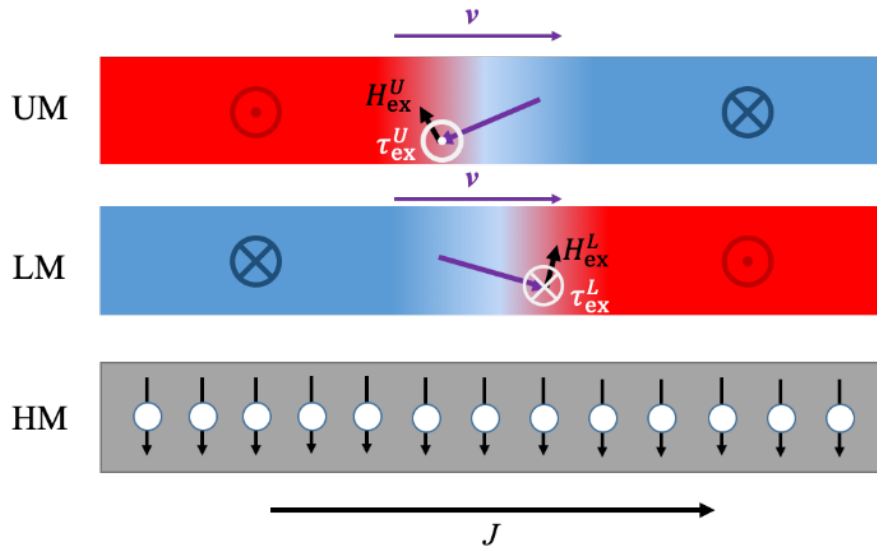


Figure 2-20: Exchange coupling torques in the SAF structure. When the DW magnetization inside the magnet sublayers deviates from each other, the ECT in each sub-layer gives rise to the velocity in the same direction and boosts the DW in the SAF case with high speed.

By increasing the current density injected in the system, the angle between the two DW magnetization will further deviate from their equilibrium position and a larger ECT indicated from the expression $\frac{2J_{\text{ex}}}{M_i} \sin(\varphi_U - \varphi_L)$ is then exerted. The ECT will take a maximum when the angle between the two magnetization forms an angle of $\frac{\pi}{2}$. To reach a higher DW velocity

Chapter 2

in the exchange-coupled system, a higher exchange coupling constant is required. In the ferrimagnets and anti-ferromagnets, the ECT is also the underlying mechanism for the ultra-fast DW velocity observed in these systems [24, 92]. In this strongly exchange-coupled system, the tiniest variation of the two DW magnetizations combined with the very large exchange coupling constant will give rise to a very fast DW velocity.

In conclusion, the CIDWM in SAF structure shows distinct behavior comparing to the SOT-driven CIDWM in the ferromagnetic case as a much faster velocity and non-linear response to longitudinal field application. The main reason for these differences lies in the presence of the exchange coupling torque originating from the large exchange coupling between the two magnetic sub-layers.

3. Experimental methods

In this chapter, the experimental methods for sample deposition, device fabrication, and measurement for current-induced domain wall motion with differential Kerr microscopy are introduced.

3.1. Sample preparation and lithography

The sample films are prepared by DC magnetron sputtering in an AJA sputtering system at room temperature on a Si (100) wafer with a naturally oxidized SiO_x layer (~30nm). Two identical sample structures are prepared for the magnetic Kerr microscopic measurement: the film structure with a single ferromagnetic layer consisting of Co(3Å)/Ni(7Å)/Co(1.5Å) sandwiched by a Pt underlayer (15Å) and Ru upper layer (8.5Å), hereafter referred as the FM structure and a synthetic antiferromagnet structure deposited on the same Pt (15 Å) underlayer and consisting of a lower ferromagnetic layer of Co (3 Å)/Ni (7 Å)/Co (1.5 Å) and an upper ferromagnetic layer of Co (5 Å)/Ni (7 Å)/Co (1.5 Å) antiferromagnetically exchange-coupled through a Ru (8.5 Å) spacer, hereafter referred to as a SAF structure. A TaN seed layer ~20Å is deposited before the deposition of Pt under layer to guarantee the *fcc* 111 structure of the films. For the prevention of oxidization, a TaN capping layer ~50Å is further deposited. A series of atomically thin layers (hereafter referred to as dusting layers, DL) of Pd, Ir, Rh, and Ru with thicknesses varying from 1 to 7 Å is inserted directly onto the Pt underlayer in both structures before the ferromagnetic materials are deposited. Figure 3.1a is the schematic images of the FM and SAF structures with DLs; Figure 3.1b illustrates the atom stacking and DL material parameters, and Figure 3.1c shows the cross-sectional high-resolution transmission electron microscopy (HRTEM) image of an FM structure with a 1Å Pd DL, which presents a highly (111) oriented structure of the face-centered cubic (*fcc*) thin-film structure. The detailed atomic

Chapter 3

force microscope topologies and x-ray diffraction patterns of the films are present in the Appendix B.

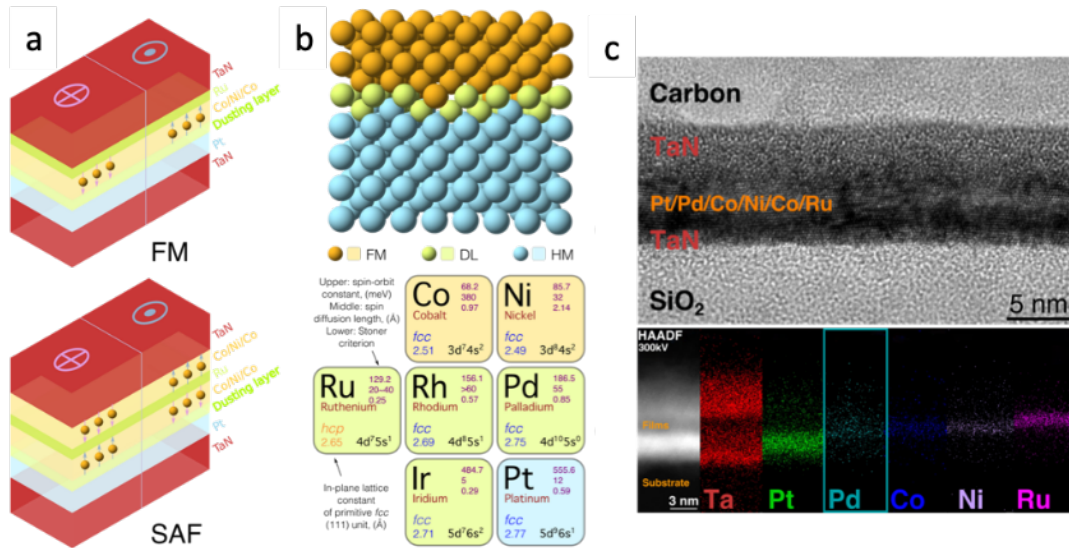


Figure 3-1: FM and SAF structure with DL insertions. (a) The FM and SAF stacking structures with DL insertions; (b) Atom stackings of FM/DL/HM interface and detailed parameters for DL materials; (c) The cross-sectional high-resolution transmission electron microscopy (HRTEM) image and High-angle annular dark-field imaging (HAADF) of an FM structure with a 1 Å Pd DL.

Chapter 3

The films are further fabricated into racetrack devices through standard photolithography procedures [12, 17, 21]. A $2\mu\text{m}$ -thick positive photo resist of ARP3540T is spin-coated on the films and baked at 375K for 1min. The racetrack patterns are made on to the film through the photolithography and developing process with a diluted AZ351B (1:4 Deionized water). The remnant films that are not covered by the photoresist is removed through Ar-ion milling. After a lift-off procedure using solvents of Acetone and Ethanol, the remaining photoresist are removed, and only the films of racetrack devices remain. Figure 3.2a illustrates the device fabricating process and typical SEM (*Scanning Electron Microscope*) images of racetrack devices with a $3\mu\text{m}$ -wide and $50\mu\text{m}$ -long wire is presented in Figure 3.2b.

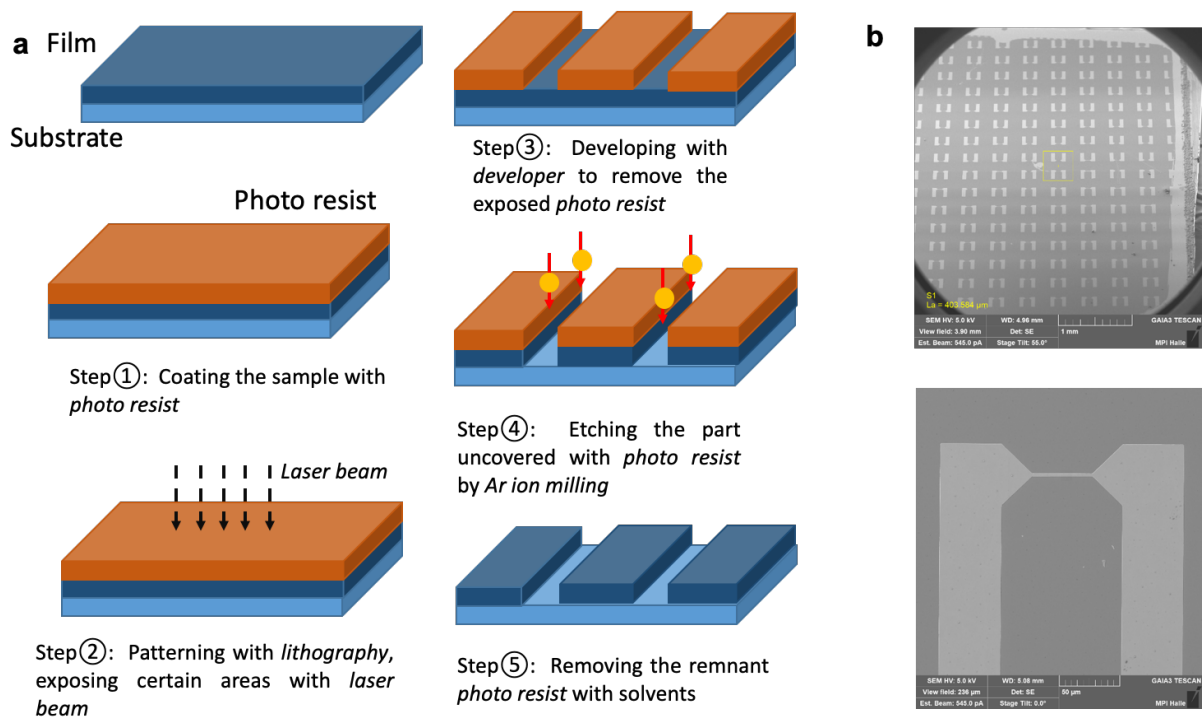


Figure 3-2: The device fabrication process with photolithography and SEM images of racetrack devices.(a) The standard procedures to fabricate the device by photolithography with positive photoresist; (b) The SEM image of the patterned sample and the racetrack device with a nanowire size of $3\mu\text{m}$ -wide and $50\mu\text{m}$ -long.

3.2. Differential Kerr Microscopy based on Magnet-Optic Kerr Effect

When a linearly polarized light reflects on the surface of a magnetic material, both the polarization and intensity will be changed depending on the magnetization vector of the magnetic material. These changes from the reflection on the magnetic surface are called the *magnet-optic Kerr effect* (MOKE). Based on the MOKE, a Kerr microscope could be built to distinguish the different magnetic domains with different magnetizations. The working mechanism is summarized as follows: after the illuminating light is emitted from the light source, it will go through a polarizer that gives certain polarization to the incident light. When the incident light reaches the magnetic surface and gets reflected, it will then pass through an analyzer before it finally goes through a regular microscope. Because of the MOKE, when the polarized light is reflected from the magnetic surface, a change, including the Kerr rotation, Kerr ellipticity, or polarized amplitude will occur. The analyzer could convert such invisible changes into changes in visible light intensity. Since the different magnetic domains will give different changes to their locally reflected light, the different magnetic domains could be imaged by the intensity difference. Figure 3.3 shows the typical Kerr image of the perpendicular magnetized FM sample with different domains; the dark and light parts represent the up (\uparrow) and down (\downarrow) magnetization domains. With higher magnetization, such intensity difference or the contrast of different domains will be higher.

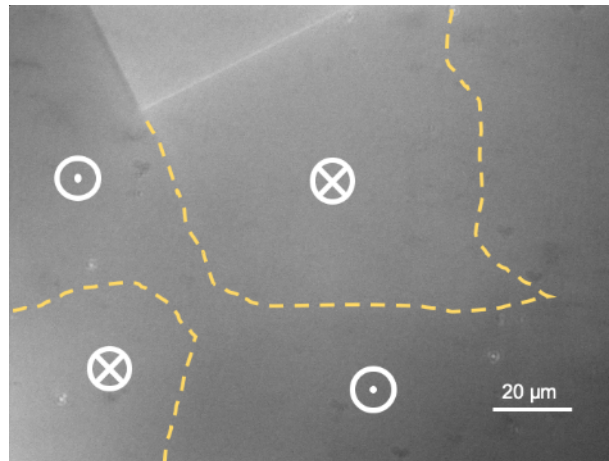


Figure 3-3: The Kerr microscope image of a typical FM structure. The dark and bright parts represent the up and down domains; the yellow lines represent the domain boundaries.

Chapter 3

To better view the dynamics in magnetization through domain wall motion, a method called the differential Kerr microscopy is used. The Kerr microscopy reference image of the original magnetic structure is saved digitally before any operations; after some operations, e.g., the current-induced domain wall motion or merely the magnetic field application, the final image of the magnetic structure will also be saved. By subtracting the reference image from the final image, the changes in the magnetic structure compared to the original state can be seen. This method could effectively avoid the non-magnetic signal and increase the contrast from different magnetic domains, so only the magnetic structure is observed. In the domain wall motion case, as shown in Figure 3.4, when a DW moves from the \uparrow domain to a \downarrow domain, a DW displacement with dark contrast is exhibited; when the DW moves from \downarrow domain to \uparrow domain, a displacement with bright contrast is viewed vice versa. Such contrast could be further enhanced by further increase the amplitude of the differential image obtained, which is widely used for the SAF case since the remnant magnetization is extremely small.

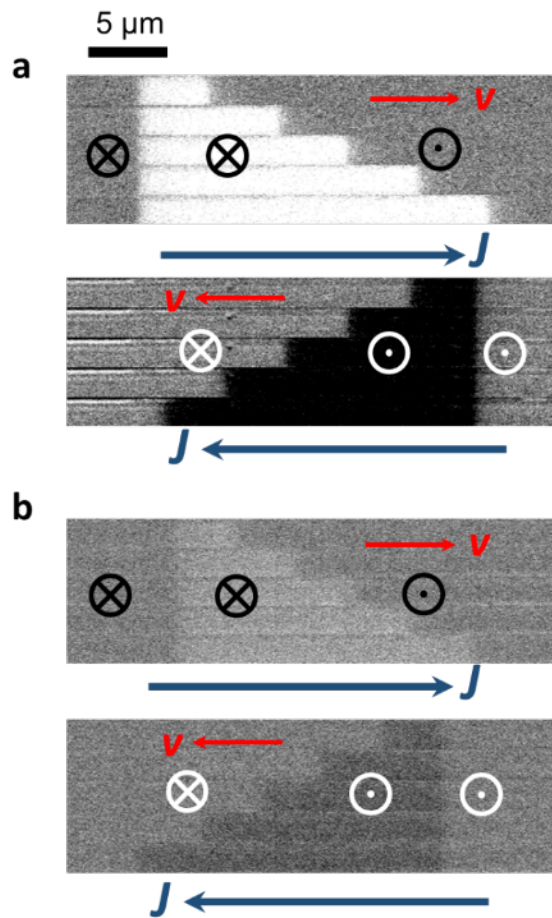


Figure 3-4: Current-induced domain wall motion measured under differential Kerr microscopy. (a) a DW in FM structure is coming from a down(up) domain to an up(down) domain by a series of 5×10 ns current pulses; (b) a DW in SAF structure coming from down(up) domain to up(down) domain by a series of 5×10 ns current pulses.

3.3. Set-up for Current-induced Domain Wall Motion

The typical pattern of the racetrack device composes of two electrode pads for pulse voltage injection and a nanowire for the magnetic domain wall motion between them. A DW is injected into the nanowire by either a magnetic field application (FM case) or by current-induced magnetization switching with an exterior field application (SAF case). A voltage pulse with nanosecond pulse length is generated from an Avtech pulse generator and injected into one of the pads to motivate the domain wall while the other pad is grounded. Because of the device geometry, the pulsed voltage will be mainly applied to the nanowire part. Because we mainly obtain the differential Kerr microscopy image in the time length of a millisecond, the DW velocity by these nanosecond timescale pulses could only be measured by the DW displacement. After a series of pulse applications, the DW velocity is determined by dividing the DW displacement l by the total pulse length t_p as $v = l/t_p$. To obtain the more accurate DW velocity and decrease the system error, a linear fitting of serial DW displacement against voltage pulse length is used to determine v in real experiments.

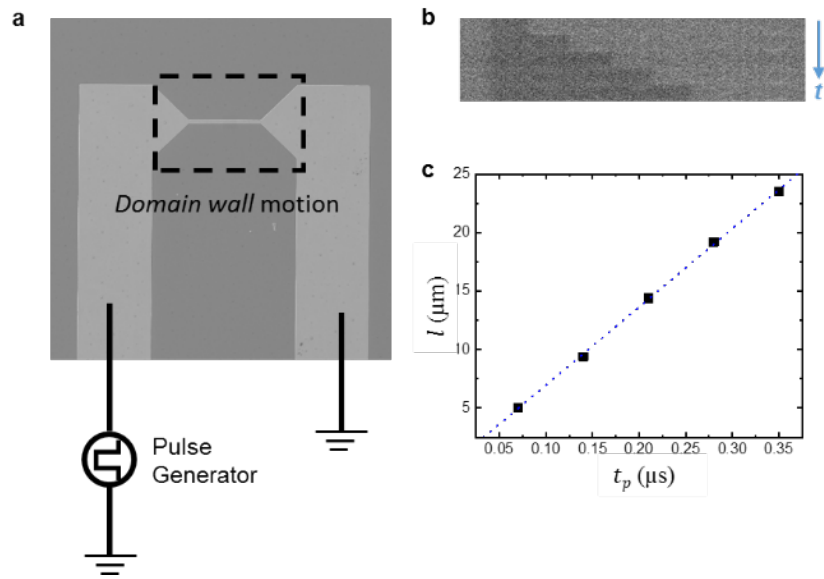


Figure 3-5: The set-up for current-induced domain wall motion. (a) Circuit diagram of a racetrack device for CIDWM; (b) The measured CIDWM in a typical SAF structure with series of $5 \times 10\text{ns}$ pulse injections; (c) The linear fitting of cumulative DW displacement and pulse length for determination of DW velocity.

4. CIDWM in FM and SAF structures with 4d and 5d DL insertions

In this chapter, CIDWM measurements for FM (4.1) and SAF (4.2) structure with various DL insertions are present. The threshold current density (J_{th}), DW mobility around the threshold current density (ξ_{DW}), and DW velocity at certain current density (v_c) is compared to give a full scope of the DL material and thickness effects on the CIDWM in both structures. The longitudinal field dependence of the DW velocity at certain current density with different DL insertions is also examined. Additional temperature, pulse length, and size effects on CIDWM are discussed in the FM structure.

4.1. Current-induced chiral DW motion in FM structure with DL insertions

As described in the former chapter, the current-induced chiral domain wall motion in a racetrack device with the nanowire size of $3\mu\text{m}\times 50\mu\text{m}$ composed of typical FM structure with DL insertions as Pt(15Å)/DL(0~7Å)/Co(3Å)Ni(7Å)Co(1.5Å)/Ru(8.5Å) is examined. The temperature, pulse length, and racetrack size dependence of CIDWM in reference FM structure with no DL insertions is also compared with a 2Å Pd DL insertion FM structure.

4.1.1. DL thickness and material dependence of CIDWM in FM structure

Since the very interfacial nature of the spin-orbitronic parameters (e.g., DMI, K_u^{eff} and spin Hall angle), by insertion of DLs, these parameters are significantly modified. Since the deterministic role of these spin-orbitronic parameters in the CIDWM, significant changes will be introduced regarding the DL thickness and materials. Here, DLs of both 4d (Pd, Rh, and Ru) and 5d(Ir) materials are used. As shown in Figure 4.1, the chiral DW always moves along the electrical

Chapter 4

current injection direction, independent of the DL materials and thicknesses. For the case of both Pd and Rh DLs, the threshold current density J_{th} is significantly decreased for DL as thin as only 1 Å (Figure. 4.1a & b), and the DW velocity, v , is increased for all current densities considered. With increasing the DL thickness, a descending trend in v is observed, but the J_{th} remains smaller compared to the reference FM structure. In the Ir case, however, a smaller J_{th} , together with a negligible increase in v , could only be observed when Ir DL is 1Å thick. As the Ir DL gets thicker, a large decrease in v and a remarkable increase in J_{th} occurs. In the Ru case, however, due to the lattice structure difference (in all other materials, an *fcc* 111 structure is favored while Ru is *hcp*), the PMA of the film quickly diminish, and sizable CIDWM could only be observed in Ru DL 1Å case with a smaller J_{th} . Due to the decrease of PMA in all thicker DL cases, the maximum current density that can be applied to the racetracks is limited by the formation of multiple magnetic domains. Such a scenario can be attributed to an increase in temperature of the nanowire by high current density injection, as has previously been observed in nanowires of comparable resistance.

Chapter 4

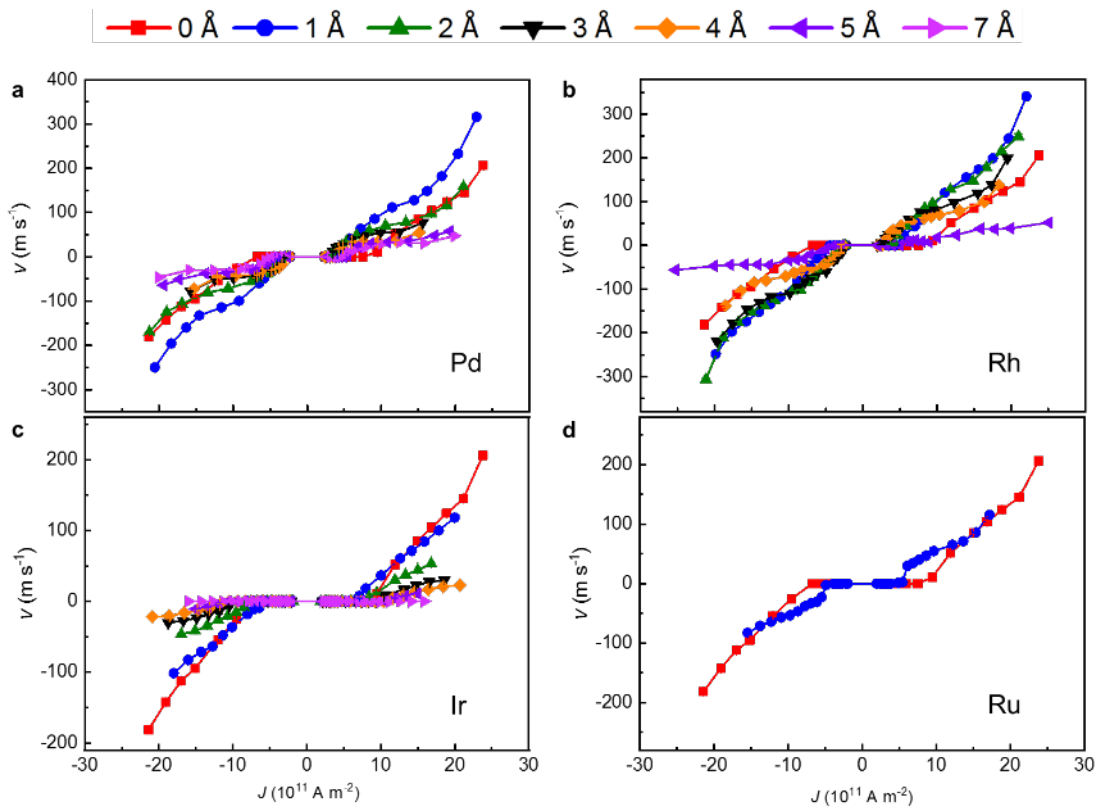


Figure 4-1: Current-induced chiral domain wall motion in FM structure with various DLs. The DW velocity v is plotted as a function of injected current density J in FM structure samples with Pd (a), Rh (b), Ir (c), and Ru (d) DLs of different thicknesses.

Chapter 4

To give a full scope of the influence of DL on the CIDWM, (i) J_{th} , (ii) DW mobility around J_{th} (ξ_{DW}), and (iii) v at a given current density of 1.2×10^{12} A m⁻² (v_C) are plotted in Pd, Rh and Ir DL cases against the DL thickness (as depicted in Figure. 4.2). To distinguish from creeping and depinning progress of DW at small current density, we redefine the J_{th} here as the current density where DW velocity exceeds 5m/s, which is also applicable for the later SAF case. The DW mobility ξ_{DW} is defined as the slope of the v - J curve around J_{th} as a linearly fitting is used here. For Pd and Rh DLs, a decreased J_{th} together with an increased ξ_{DW} is observed for thin DLs (1-4 Å), as shown in Figure. 4.2a and 4.2b. A decrease in J_{th} of up to 30% and an increase in ξ_{DW} of more than 200 % is found. For Ir DLs, although a slight decrease in J_{th} is found for the thinnest DLs, substantial reductions in ξ_{DW} are observed. For Pd and Rh DLs, the dependence of v_C on t_{DL} is similar: v_C initially increases significantly and then drops monotonically as t_{DL} is increased from zero; by comparison, a monotonic drop in DW velocity is observed with increasing t_{DL} for Ir DLs (Fig. 4.2c).

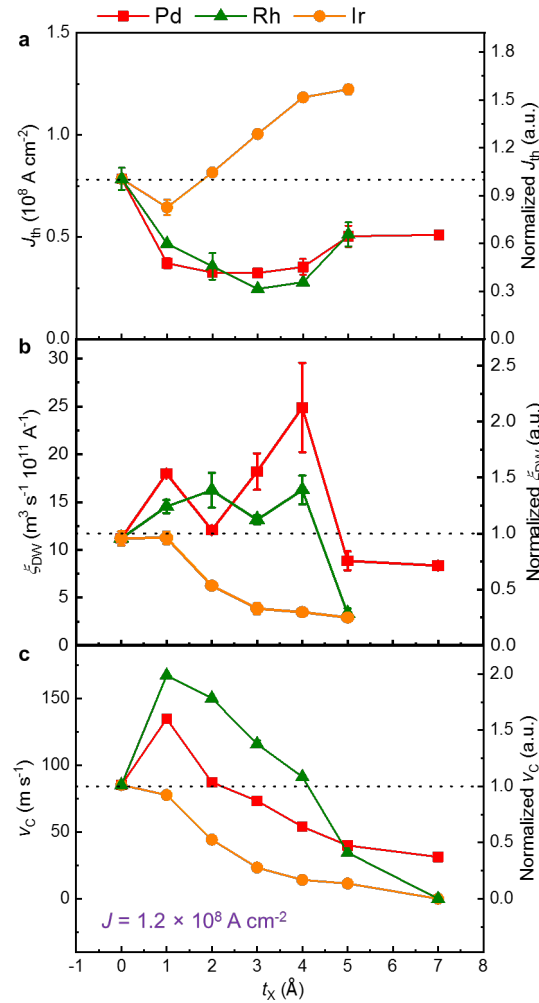


Figure 4-2: The DL thickness dependence of threshold current density, DW mobility, and DW velocity at a fixed current density in FM structures with DL insertion. The threshold current (J_{th}) (a), DW mobility (ξ_{DW}) (b), and DW velocity at a fixed current density of $1.2 \times 10^{12} \text{ A m}^{-2}$ (v_c) (c) are plotted as a function of DL thickness. The right panel corresponds to the renormalized value concerning the reference FM sample. The dashed lines are the corresponding value of the reference FM sample.

4.1.2. Temperature, pulse length, and device size dependence of CIDWM in FM structure

Since the magnetic properties sensitively depend on temperature, the CIDWM could be well affected when the temperature is varied. CIDWM in the reference FM sample, together

Chapter 4

with the sample with 2Å Pd DL, is measured at the temperature varied from 100K to 295K with the injected voltage pulse length of 10ns (Figure. 4.3a and b). When the temperature decreases, v decreases while J_{th} increases. Interestingly, J_{th} shows a linear dependence on the temperature in both samples with almost the same slope, as illustrated in Figure. 4.3c. Such behavior could be interpreted as the increase of magnetization together with a thermally dependent pinning strength. J_{th} will increase by $0.4 \times 10^{11} \text{ A/m}^2$ when the temperature rises 10K.

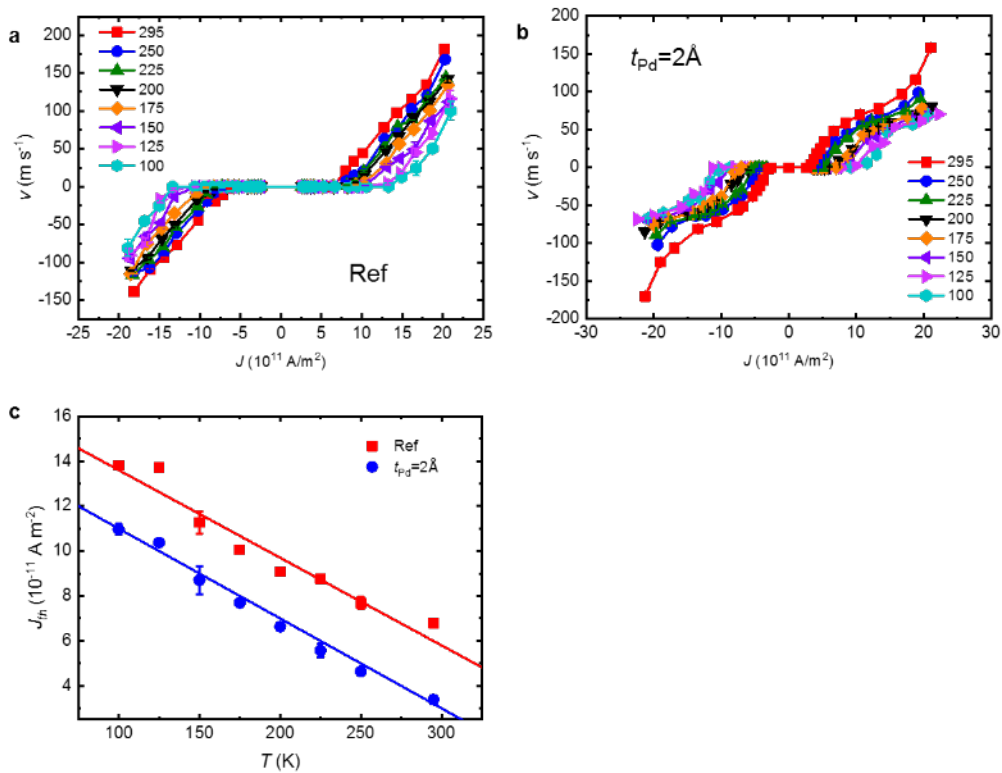


Figure 4-3: Temperature dependence of CIDWM in FM structure. The v - J curve at various temperatures of the reference FM sample (a) and 2Å Pd DL sample (b) are plotted. The threshold current density plotted as a function of temperature (c), the solid lines are the linear fitting for the data points.

When the current pulses are injected into the system to motivate the DW, the temperature in the device will inevitably increase due to the Joule heating. Voltage pulses with different pulse lengths ranging from 5ns to 50ns are compared to investigate the Joule heating effect on the CIDWM in the same samples used in the former temperature dependence measurement (Figure. 4.4). The J - v curves in both samples are observed to have modest changes

Chapter 4

when the pulse length is varied, as shown in Figure 4.4a and b. When J_{th} is subtracted and plotted against the pulse length, again, very much alike behaviors of the two samples but with some offset are presented in Figure 4.4c: J_{th} firstly decreases and saturates with an increasing pulse length. Such behavior could be explained in the following ways: Temperature increase by the Joule heating is only introduced to the system when the current pulses are injected into the system, and will quickly drop by heat conduction after the pulse, so the longer the pulses are, the higher the temperature will reach. But when the pulse length is long enough, the increase of the temperature will result in a lower J_{th} , and such lower J_{th} will give a feedback as a more limited increase of temperature, so a saturating behavior will thus occur. Comparing the saturating value of J_{th} with the J_{th} value when 10ns pulses are used, a temperature increase of 40K at the J_{th} in reference FM sample and 20K temperature increase in 2Å Pd DL are anticipated.

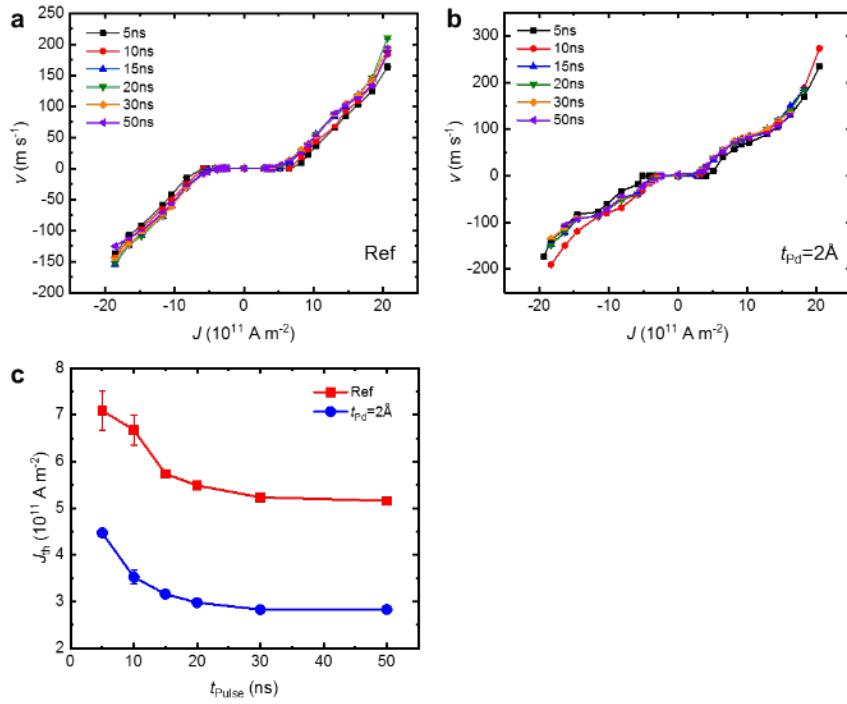


Figure 4-4: Dependence of the CIDWM on pulse length in FM structure. The DW velocity (v) is plotted as a function of current density (J) with various pulse lengths in reference FM sample (a) and 2Å Pd DL sample (b). The threshold current density (J_{th}) summarized from (a) and (b) is plotted against the pulse length (c).

Chapter 4

In real applications, to realize high-density memory storage, compact racetrack devices are required. Thus, reducing the size of the racetrack devices is of great importance to be examined. Different sizes of the nanowires varying from 200nm to 1.7 μ m are prepared, and CIDWM are measured in both the reference FM sample and 2Å Pd DL sample (Figure. 4.5). J_{th} is also summarized regarding the wire width, as shown in Figure 4.5c. Two similar linear relationships have again been observed for the two distinct samples. When the wire goes narrower, the CIDWM performance degrades with an increasing J_{th} and decreasing ν . Unlike J_{th} changes induced by the intrinsic demagnetizing energy change in spin-transfer torque driven DWM case, here an extrinsic cause from edge roughness in the nanowire is attributed to. Because of the limitation of the lithography process, a perfect wire with an ultra-smooth edge is tough to realize. In narrower wires, the role of edge roughness becomes more dominant since the roughness area to wire area ratio increases. Thus, extrinsic pinning becomes stronger in thinner wires, and J_{th} is consequently increased.

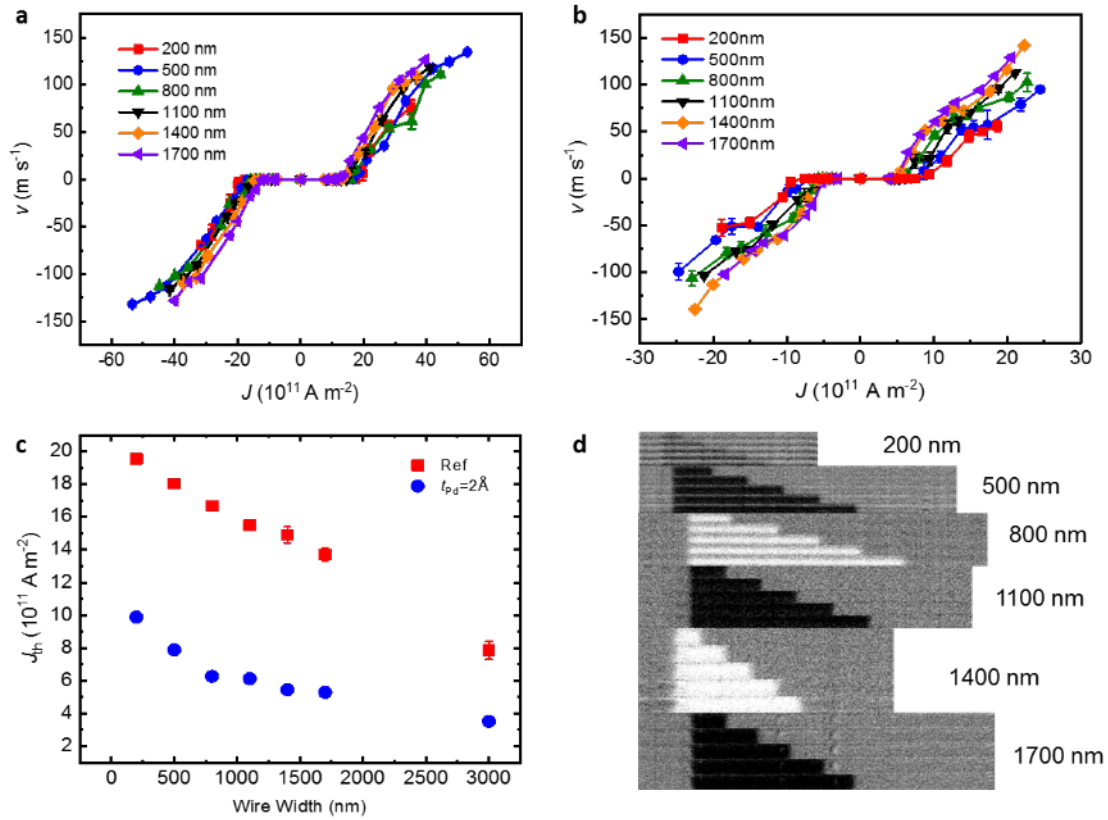


Figure 4-5: Wire width dependence of CIDWM in FM structure. (a) The CIDWM in reference FM sample of different wire width. (b) The CIDWM in the FM sample with 2 \AA Pd DL of different wire width. (c) The summarized threshold current density versus wire width in both samples from (a) and (b). (d) The differential Kerr microscopy images of CIDWM with different wire width in the reference FM sample. The data point at a wire width of 3000nm is obtained from Figure. 4.2a.

4.1.3. Longitudinal field dependence of CIDWM in FM structure with DLs

As mentioned in the previous chapter and previous work[ref], in the spin-orbit torque driven chiral DW motion case, by application of external magnetic field in the longitudinal direction (parallel/antiparallel to the current injection direction), the Néel DW structure fixed by interfacial DMI will be modified. A linear response of DW velocity to the exterior field will be observed in FM structures. The DW velocity v for both up/down and down/up DWs at a fixed current density of 1.2×10^{12} A/m² is plotted as a function of the exterior field in Figure 4.6 with various DL insertions. As can be seen in Figure 4.6, both the slope of the v - H_X curves and the magnitude of H_X where v turns to zero (DMI effective field H_{DMI}) strongly depend on the variety and thickness of DLs. A linear fitting is used to determine the H_{DMI} , as shown in Figure 4.6g. The summarized H_{DMI} is also plotted as a function of DL thicknesses for Pd, Rh, and Ir DLs in Figure 4.7. A clear descending trend of H_{DMI} is observed when DL thickness increases except for the Rh DL 1Å case. Such a trend could be readily understood since none of the Co/Pd, Co/Rh, and Co/Ir interfaces have larger DMI than Co/Pt interfaces. The summarized H_{DMI} together with latterly measured saturation magnetization M_S and uniaxial magnetic anisotropy energy K_u^{eff} are used to calculate the effective DMI constant in Chapter 5.

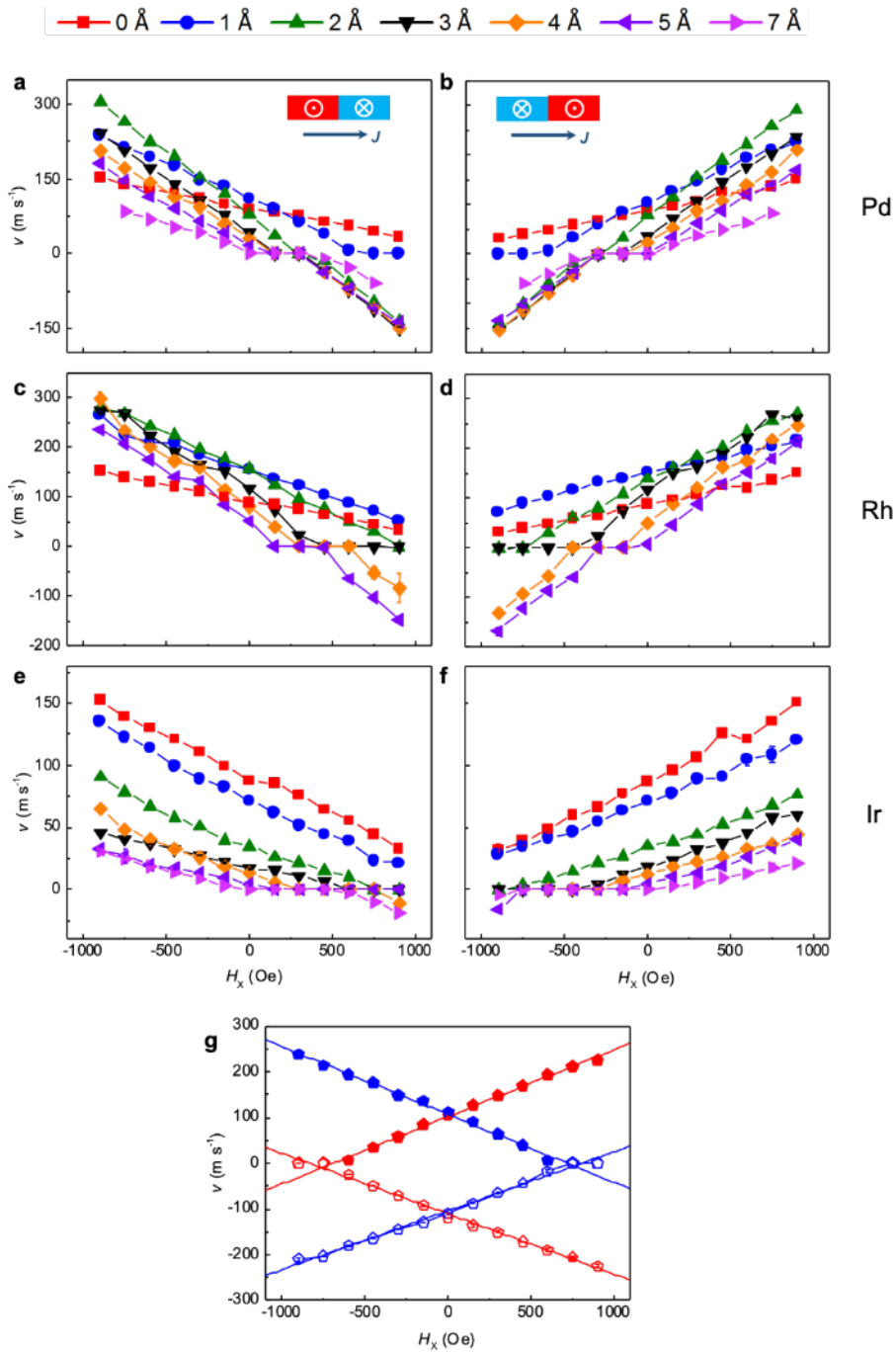


Figure 4-6: Longitudinal field dependence of the DW velocity in FM structure with various DLs. The DW velocity is plotted as a function of H_x in Pd (a and b), Rh (c and d), and Ir (e and f) DL insertions. The left (right) column shows the up/down(down/up) DW configuration. The linear fitting of the v - H_x curve is used for the determination of H_{DMI} (g).

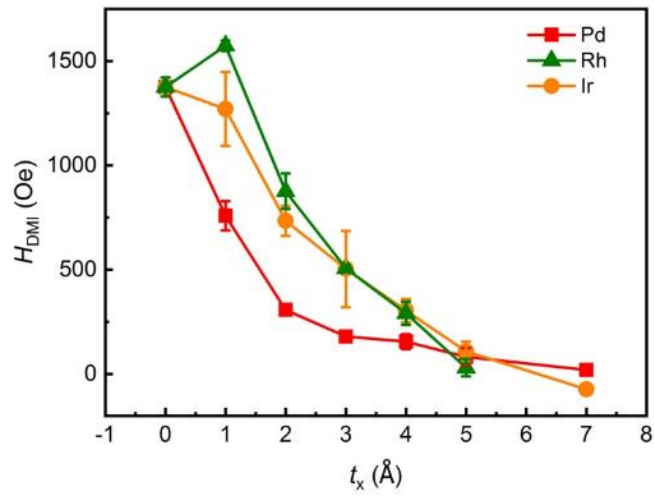


Figure 4-7: DL thickness dependence of DMI effective field in FM structures. The red square, olive triangle, and orange circle correspond to Pd, Rh, and Ir DL, respectively.

4.2. Current-induced chiral DW motion in SAF structure with DL insertions

In this chapter, the CIDWM in a racetrack device with the nanowire size of $3\mu\text{m}\times 50\mu\text{m}$ composed of the typical structure of SAF structure with DL insertions as Pt(15Å)/DL(0~7Å)/Co(3Å)Ni(7Å)Co(1.5Å)/Ru(8.5Å)/Co(5Å)Ni(7Å)Co(1.5Å) is examined. Dependence of threshold current density, DW mobility, and DW velocity on DL materials and thicknesses are also investigated. The longitudinal field dependence of CIDWM is also measured.

4.2.1. DL thickness and material dependence of CIDWM in SAF structure

Compared to the CIDWM in the FM structure, the CIDWM in SAF structure has even more delicate dependence on the interfacial modifications since its complicated film structure. When plotting the DW velocity (v) as a function of injected current density (J), as shown in Figure 4.8, distinct behavior could be observed for the SAF structure. In all the following measurements, a pulse length of 10ns is used. The performance of the CIDWM is improved for all Pd DL thicknesses considered and is maximized for a Pd DL that is just ~ 2 Å thick. The DW velocity is increased to ~ 1000 m/s (Figure. 4.8a), which is ~ 3.5 times higher than that of the reference SAF at the same current density. For the Rh DL case, the DW velocity is also increased for ultra-thin DLs (1 & 2 Å), but the maximum v achieved was lower (~ 600 m/s), as shown in Figure 4.8b. For the Ir DL case, a systematic deterioration of the CIDWM occurs as soon as an Ir DL is inserted (Figure. 4.8c). However, it is worth noticing that J_{th} drops smoothly for Ir DLs with thicknesses up to 5 Å but then increases dramatically for thicker layers. Unlike the former three DL insertion cases where the DW always moves along the current injection direction, when the thickness of Ru DL increases, the DW performance quickly deteriorates and finally moves along the electron flow direction (Figure 4.8d).

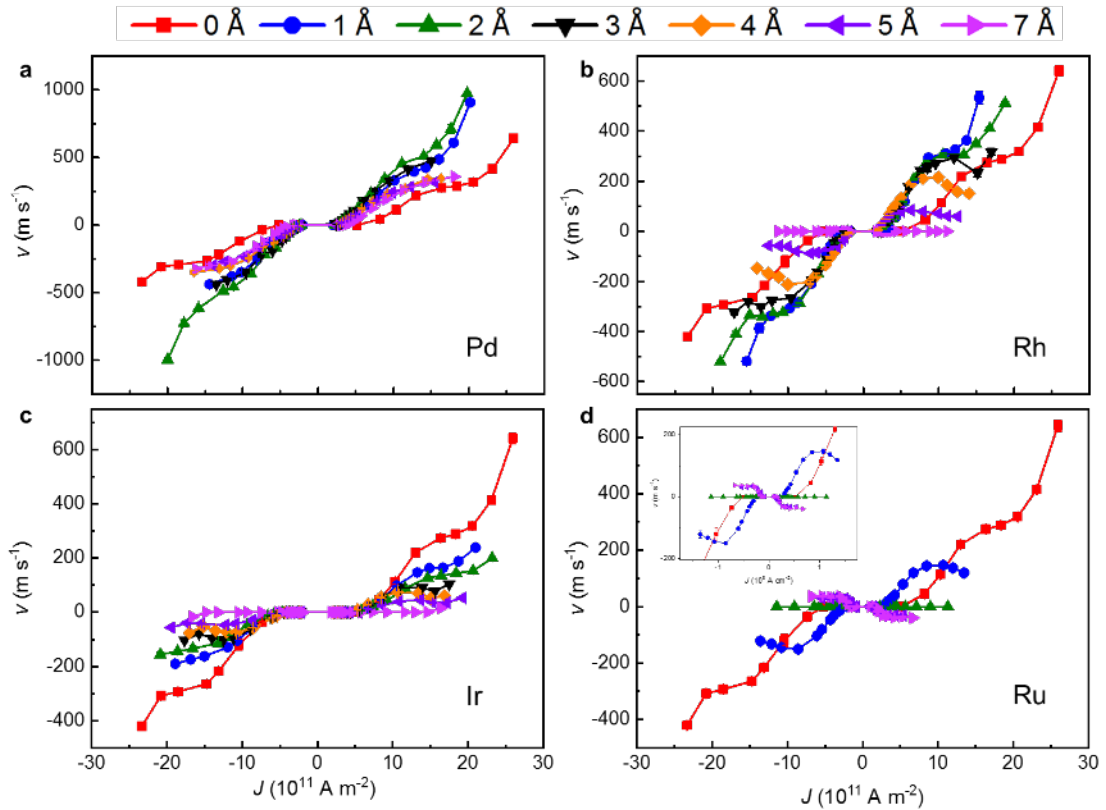


Figure 4-8: Current-induced chiral domain wall motion in SAF structure with various DLs. The DW velocity v is plotted as a function of injected current density J in SAF structure samples with Pd (a), Rh (b), Ir (c), and Ru (d) DLs of different thicknesses.

Like in the FM structure, threshold current density (J_{th}), DW mobility around J_{th} (ξ_{DW}), and DW velocity at $1.2 \times 10^{12} \text{ A/m}^2$ (v_C) are plotted against the DL thickness in Pd, Rh, and Ir DL cases. Similar to the FM structure with Pd and Rh DLs, a decrease in J_{th} of up to 30% and an increase in ξ_{DW} of more than 200% is found for the SAF structure. For Ir DLs, a vastly decreased J_{th} compared to the Reference SAF sample is maintained until the thickness of Ir DL goes over 5 \AA , substantial decreases in ξ_{DW} are observed. The dependence of v_C on t_{DL} also resembles the FM structure: for Pd and Rh DLs, v_C initially increases significantly and then drops monotonically as t_{DL} is increased from zero; for Ir DLs, a monotonic drop in DW velocity is observed with increasing t_{DL} (Figure 4.9c).

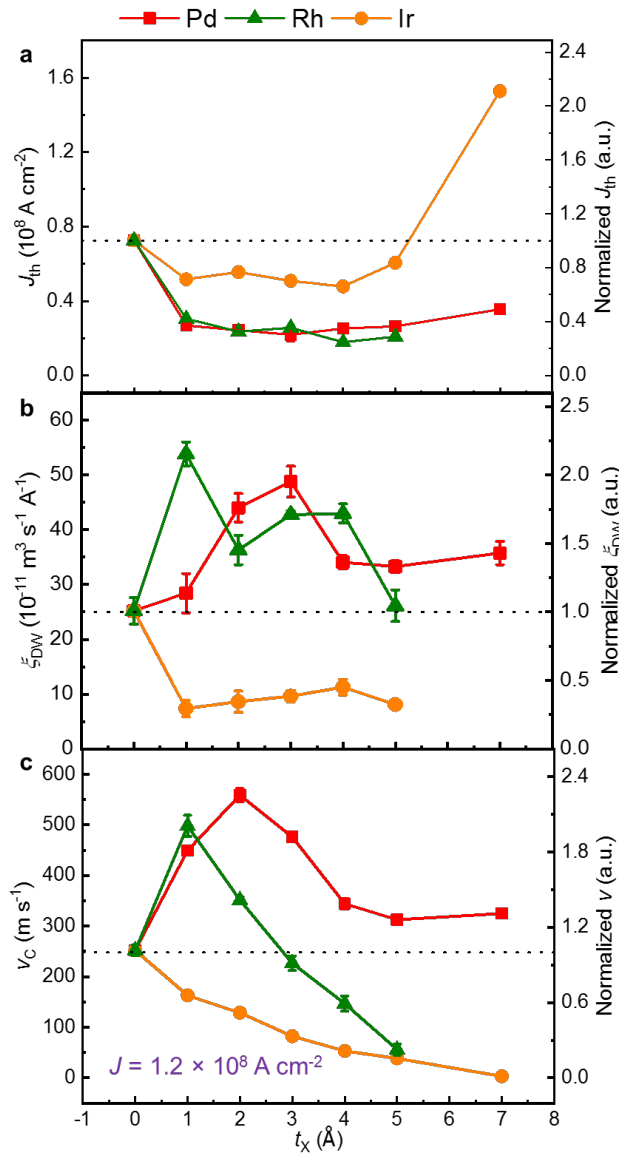


Figure 4-9: The DL thickness dependence of threshold current density, DW mobility, and DW velocity at a fixed current density in SAF structures with DL insertion. The threshold current (J_{th}) (a), DW mobility (ξ_{DW}) (b), and DW velocity at a fixed current density of $1.2 \times 10^{12} \text{ A m}^{-2}$ (v_c) (c) are plotted as a function of DL thickness. The right panel corresponds to the renormalized value concerning the reference SAF sample. The dashed lines are the corresponding value of the reference SAF sample.

4.2.2. Longitudinal field dependence of CIDWM in SAF structure with DLs

In SAF structures, because of the existence of two magnetic sub-layers that are exchange-coupled through RKKY interaction, the response of the DW velocity to longitudinal field shows a much more complicated non-linear nature rather than the linear relationship as observed in the FM structure. All the peaks like v - H_x curves of both up/down and down/up DW configurations motivated by a positive current pulse injection in SAF structure with different DLs are summarized in Figure 4.10. An interesting finding is that, when Ir DLs are thick enough ($> 5\text{\AA}$), the shape of the curve will be mirrored compared to the thin Ir DL cases. Even though these curves have very complex dependence on multiple parameters, they are latterly further understood in Appendix B by fitting them with a I - D model combining both the spin-orbit torque and exchange coupling torque. The peak velocity v_{lg} that a SAF DW could reach by the assist of the longitudinal field is also summarized according to DL materials and thicknesses in Figure 4.10g. A saturating behavior of v_{lg} is observed in the Pd and Rh DL insertion cases, while in the Ir DL case, a monotonic decrease in v_{lg} is present.

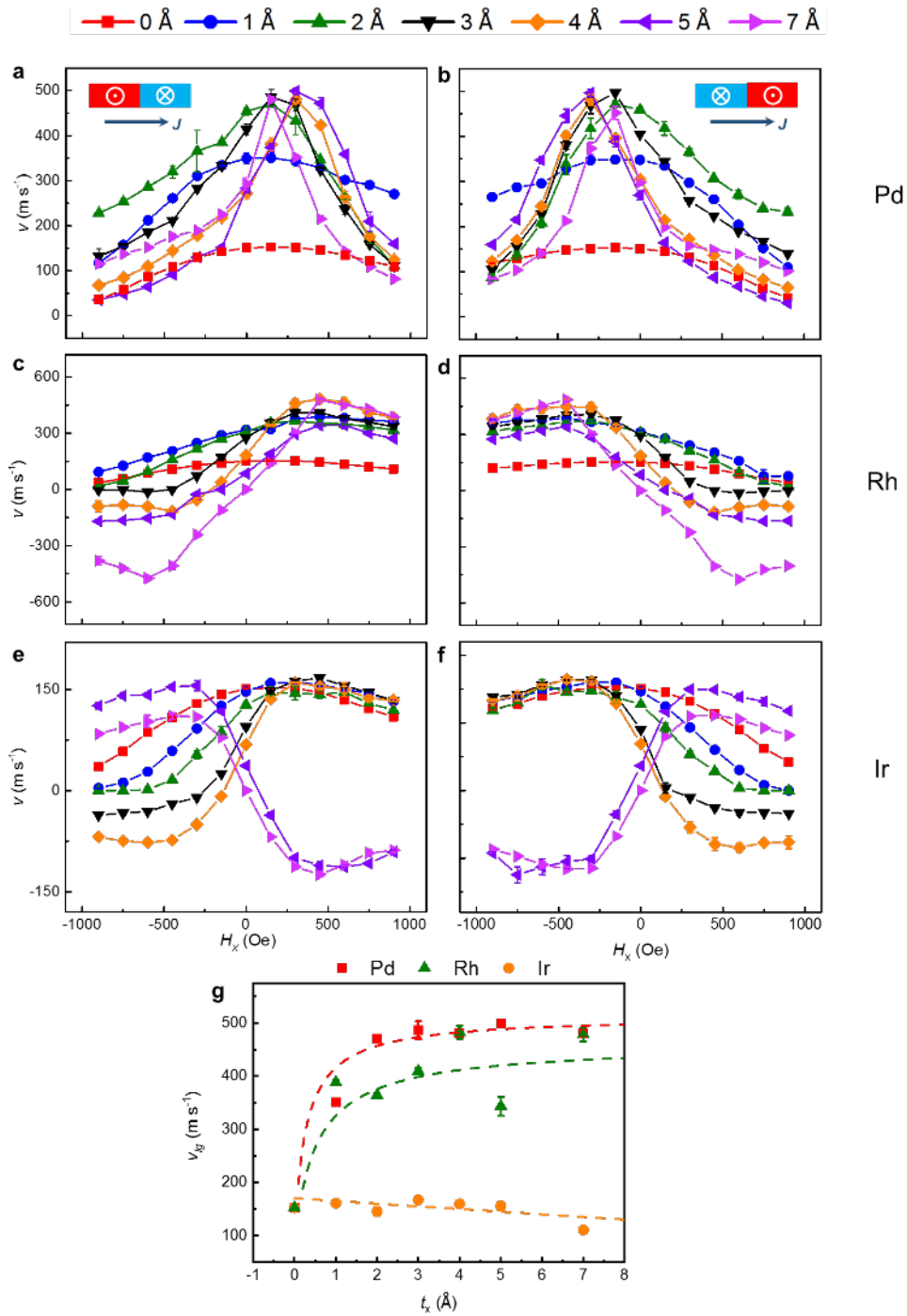


Figure 4-10: Longitudinal field dependence of the DW velocity in SAF structure with various DLs. The DW velocity is plotted as a function of H_x in SAF structure with Pd (a and b), Rh (c and d), and Ir (e and f) DL insertions. The left (right) column shows the up/down (down/up) DW configuration. The v_{lg} versus DL thickness is summarized according to different DLs (g).

5. Discussions of CIDWM in FM and SAF structures with DL insertions

In Chapter 4, when DLs which are atomically thin are inserted into both the FM and SAF structure, the CIDWM is well enhanced with a 70% decrease in threshold current density and over 150% increase in DW mobility and velocity. The following descending of the CIDWM efficiency when DLs are thick corresponds well with the former research where DLs are served as HM.

In this Chapter, discussions and analysis are made to investigate the inner mechanism for this enhancement in both FM and SAF structures. The magnetic properties of raw films are measured with SQUID measurement to obtain some critical magnetic parameters as saturation magnetization M_S , effective uniaxial magnetic anisotropy energy K_u^{eff} in FM structure, and remnant magnetization (magnetization at zero fields) to saturation magnetization (magnetization at the high out-plane field of 1.5T) ratio M_R/M_S in SAF structure. The interfacial DMI constant D is also calculated based on the H_{DMI} obtained in Chapter 4. A simplified model for ECT driven DWM in the SAF case is also present, and an effective pinning potential that directly relates to the threshold current density is defined based on the DW mobility and 1-D model. The effective SOT motivating the DW is also calculated based on the 1-D model for both FM and SAF structure. The longitudinal field dependence of the DW velocity in the SAF case is also examined by simulations based on the 1-D analytical model.

5.1. SQUID measurement for the magnetic properties of FM and SAF structures with DLs

Samples of the raw film are prepared, and magnetic hysteresis loops in both in-plane and out-of-plane direction in FM structures and out-of-plane direction in SAF structures are measured to obtain the saturation magnetization M_S , effective anisotropy field H_{eff} , effective uniaxial magnetic anisotropy energy K_u^{eff} in FM structure, and remnant magnetization to saturation magnetization ratio M_R/M_S in SAF structure.

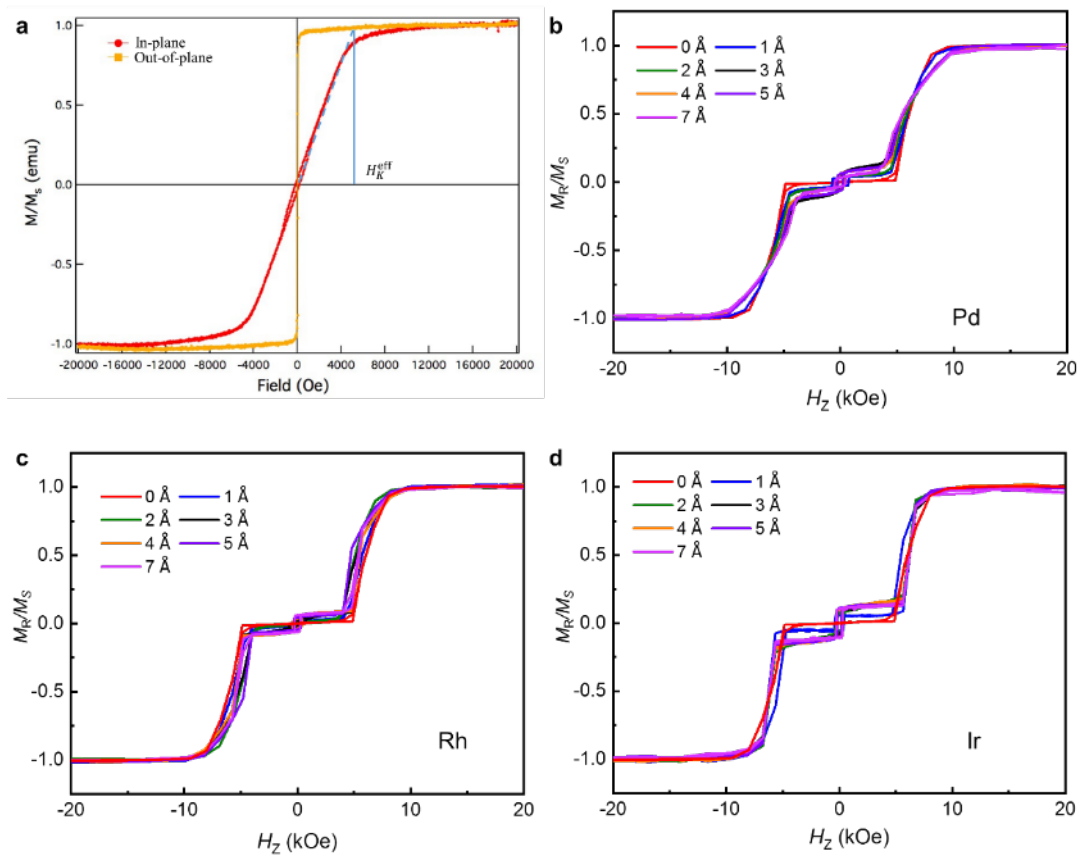


Figure 5-1: The magnetic hysteresis loops in FM and SAF structures. H_K^{eff} and M_S are determined by measuring the hysteresis loop with the in-plane field application (a). The hysteresis loop of SAF structures with an out-of-plane magnetic field application is used to determine the M_R/M_S ratio.

Chapter 5

In the FM structure, as can be seen in Figure 5.2, M_S varies little with Pd DL, while a monotonic drop for the Ir and Rh DLs cases is observed. Proximity induced magnetic moments (PIM) in heavy metals can contribute considerably to the M_S of ferromagnet/HM systems [21, 94]. Based on the Stoner criterion (Figure. 3.1b), it would not be surprising if the PIM decreases when the Ir and Rh DLs are inserted between the Co and Pt layers. On the other hand, we suppose that there may be a considerable PIM in the Pd DL itself since Pd is very close to the Stoner criteria for magnetism [95, 96]. A monotonic drop in H_{eff} can be observed with increasing t_{DL} in all cases and K_u^{eff} , which is calculated from $K_u^{\text{eff}} = \frac{1}{2} u_0 H_{\text{eff}} M_S$, also follows the same trend.

The dependence of M_R/M_S on t_{DL} is shown in Figure. 5.2d. The changes in M_R/M_S with t_{DL} are predominantly due to the variation of M_S in the lower sub-layer of the SAF structure, as found for the FM case in Figure. 5.2a. It has previously been shown that CIDWM in SAF structures is primarily derived from a giant ECT. The more similar are the two sub-layer moments, i.e., $M_R/M_S = 0$, the larger is the ECT. Note that the reference SAF sample has been optimized so that M_R/M_S is close to zero. As discussed above, the efficiency of CIDWM is increased with several angstrom-thick DLs even though the introduction of the DL causes M_R/M_S to deviate from zero (due to changes in the PIM). Thus, even faster CIDWM in the DL engineered racetracks is anticipated when M_R/M_S is reduced to zero by small modifications to the moments of the upper or lower ferromagnetic layers in the SAF structure.

The magnetization hysteresis loops are also measured for the Ru case, as shown in Figure 5.3. The PMA rapidly decreases in FM structure, and the M_R/M_S rapidly increases with Ru DL thickness increase. Interestingly, when Ru is thick ($> 3\text{\AA}$), even though no PMA could be sustained in the FM case, it could still be maintained in the SAF case, which could be attributed to the interlayer exchange coupling from the upper magnetic sub-layer.

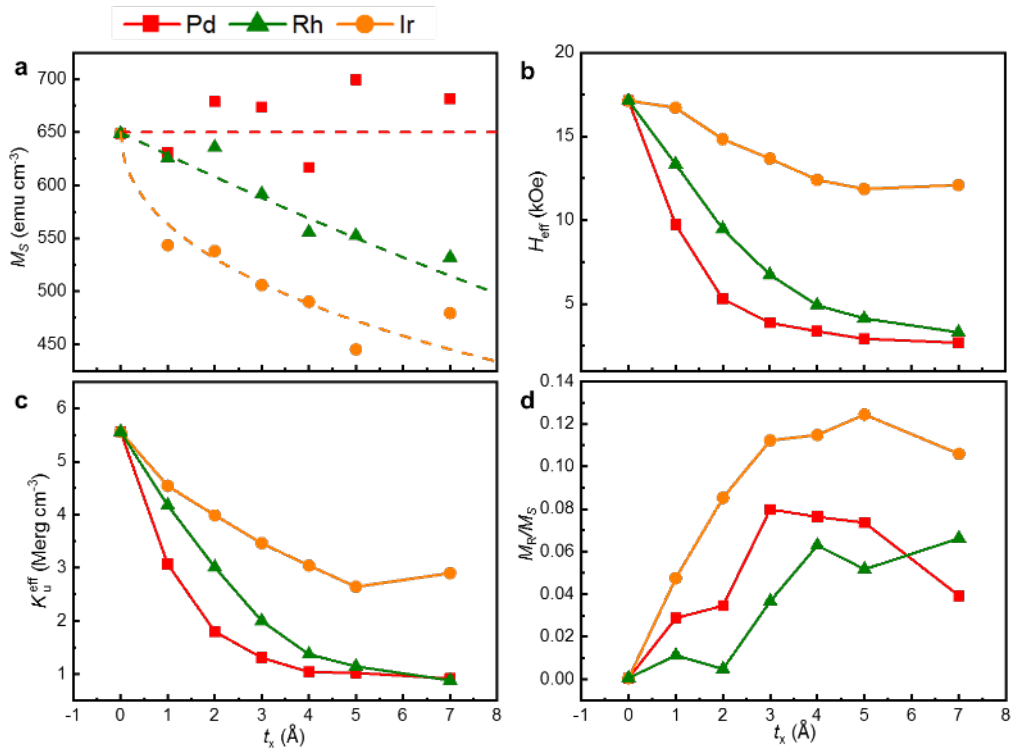


Figure 5-2: Magnetic properties obtained from the Magnetization Hysteresis loop in FM and SAF structures. The thickness dependence of M_S (a), H_{eff} (b), and K_u^{eff} (c) in FM structures and M_R/M_S (d) in SAF structures. The red square, olive triangle, and orange circle correspond to Pd, Rh, and Ir DL, respectively.

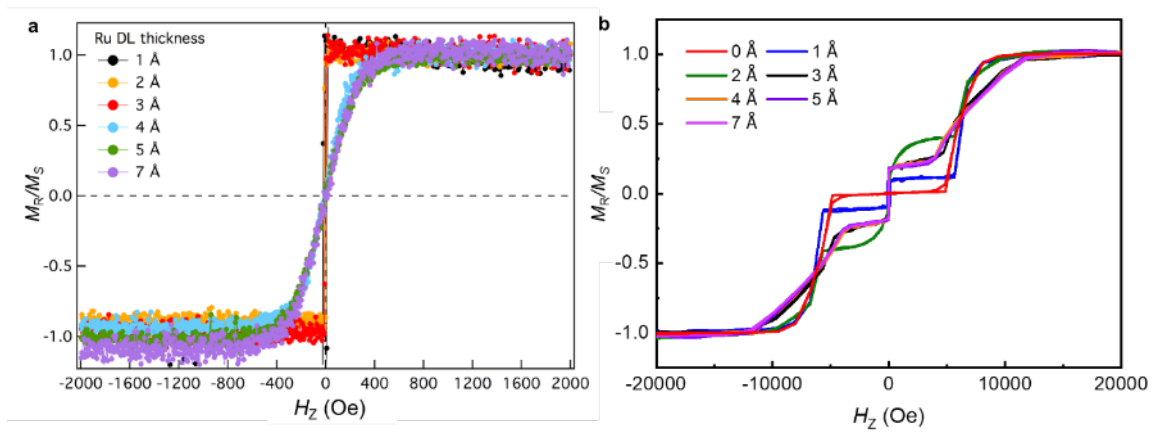


Figure 5-3: Magnetic hysteresis loop of samples with Ru DL insertion. The magnetic hysteresis loop of FM samples (a) and SAF samples (b), with Ru DL insertions.

5.2. Calculation of interfacial DMI constant of FM structures with DLs

Since the effective magnetic uniaxial anisotropy energy K_u^{eff} has been calculated, the DW width in all samples is thus calculated by the equation $\Delta = \sqrt{A/K_u^{\text{eff}}}$, where the exchange stiffness A is set to be 1×10^{-6} erg cm⁻¹ obtained from the weighted average of the Co and Ni layer ($A_{\text{Co}} = 1.8 \times 10^{-6}$ erg cm⁻¹ and $A_{\text{Ni}} = 0.8 \times 10^{-6}$ erg cm⁻¹) [12, 21]. Since the descending trend of the K_u^{eff} , the DW width increases with increasing DL thickness in all samples (Figure. 5.4a). Based on the DW width and H_{DMI} value obtained in Chapter 4, the interfacial DMI constant is also calculated. A monotonic drop in D is observed with increasing t_{DL} except for a slight increase for the Rh ~ 1 Å case (Figure. 5.4b). It is worth noting that, as the Ir DL thickness is increased, there is an evident sign change of D . It has been previously reported as the D at the Co/Ir interface, and the one at Co/Pt interface has the opposite sign to each other [27, 28, 31]. When the D is plotted against K_u^{eff} , for each DL D varies linearly with K_u^{eff} , as shown in Figure 5.5. Interestingly, a similar slope for all DLs is found, but split into two groups with different intercepts corresponding to the $4d$ elements, on the one hand, and the $5d$ elements, on the other. Since both D and K_u^{eff} originate from the interfacial spin-orbit coupling, the linear relationship between them is thus rational. The observed two distinct groupings of $4d$ and $5d$ DLs are attributed to the different contributions of the orbital angular moments of the $4d$ and $5d$ electrons, as revealed both theoretically and experimentally in prior work [97, 98].

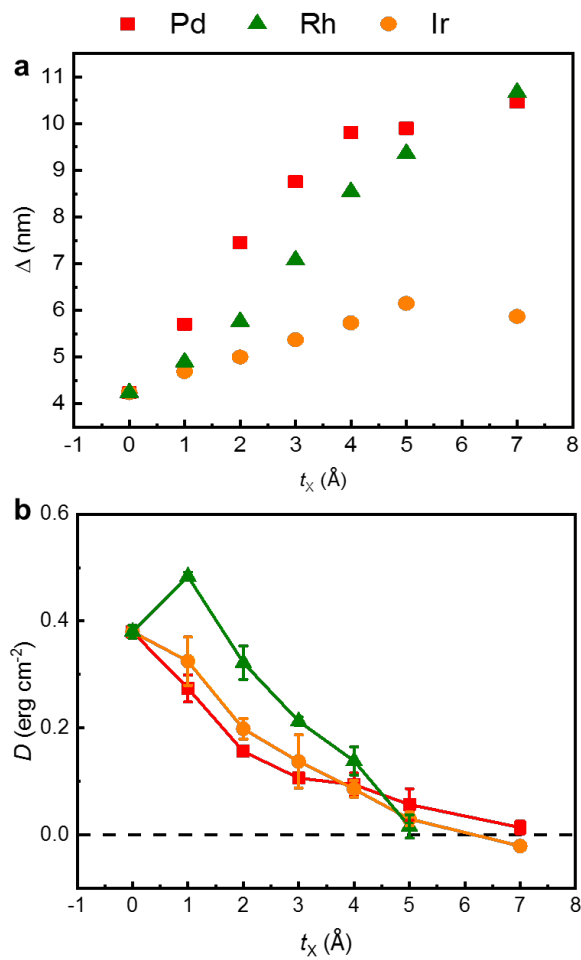


Figure 5-4: DL thickness dependence of DW width and interfacial DMI constant. The DL thickness dependence of DW width (a) and the interfacial DMI constant D (b). The red squares, olive triangles and orange circles represent the Pd, Rh and Ir DLs, respectively.

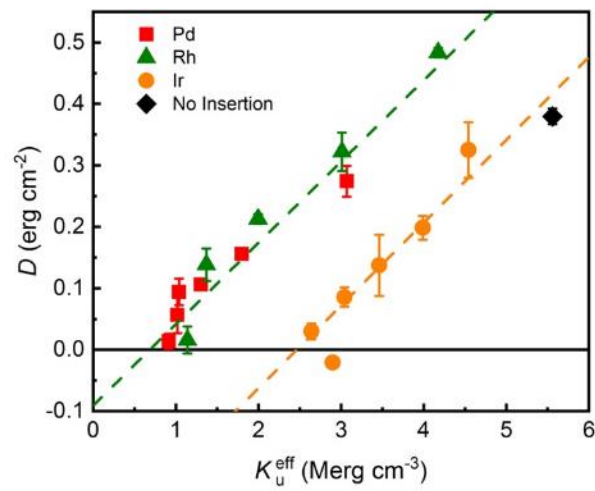


Figure 5-5: Interfacial DMI constant as a function of effective uniaxial anisotropy. The dashed lines are the linear fitting of the FM samples with 4d and 5d insertions. The red square, olive triangle, orange circle, and the black diamond represents the Pd, Rh, Ir DL, and reference FM samples, respectively.

5.3. Fitting of the v - J curve in FM structures with DLs using a simplified 1-D model

From the ideal 1-D model for the SOT-driven chiral DWM in FM structure, there is no threshold current density. When the 1-D model only involves the SOT term and DMI effective field without any STT-term, demagnetization term, and thermal terms, the DW velocity could be well described with the following form: $v = \frac{v_D}{\sqrt{1+(J_D/J)^2}}$, where $v_D = \pi\gamma_0 D/M_S$ and $J_D = 2\alpha t e D / (\hbar \theta_{SH} \Delta)$ [59]. Here, γ_0 is the gyromagnetic ratio, α is the Gilbert damping parameter, t is the thickness of the ferromagnetic layer, e is the elementary charge, \hbar is the Planck constant, and θ_{SH} the effective spin Hall angle of the combined DL/Pt layer. Because of the complicated nature of the DL inserted interface, which may include either the modification of interfacial transparency for spin current transportation or the extra scattering which may give rise to the extra spin current generation, here an effective spin Hall angle to account for the spin current absorbed by the ferromagnetic layer is used. Because of the Joule heating term in the high current density regime, the thermal term will also contribute to the CIDWM. Thus, after subtracting J_{th} , only low current density region of the v - J^* ($J^* = J - J_{th}$) curves of all the FM samples ($< 1.5 \times 10^{12}$ A m⁻²) is used for the fitting with the equation $v = \frac{v_D}{\sqrt{1+(J_D/J)^2}}$ to obtain both v_D and J_D , as shown in Figure 5.6.

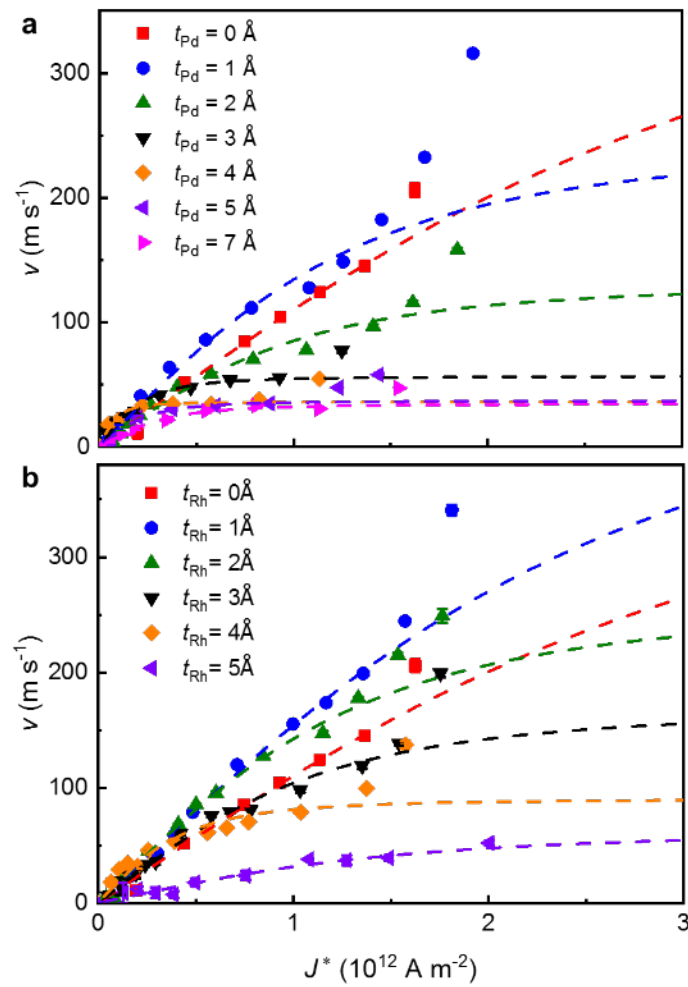


Figure 5-6: The fitting curve of the v - J curve under the subtraction of J_{th} in FM structures with DLs. The fitted curves using the I - D model of FM structures with Pd (a) and Rh (b) DLs. The fitting region is current density below $1.5 \times 10^{12} \text{ A m}^{-2}$.

Chapter 5

After fitting the v - J curve, the obtained v_D and J_D are plotted against the DL thickness, as shown in Figure 5.7, and a descending trend of both parameters is observed. Since $v_D = \pi\gamma_0 D/M_S$, the DMI constant obtained in this way could also be compared to the D obtained by the longitudinal field dependence of DW velocity. Since the CIDWM could be written in the form of $v = \frac{v_D}{\sqrt{1+(J_D/J)^2}}$, at a very low current density ($J \ll J_D$), the equation could be expanded, and DW velocity has the form $v = v_D J/J_D = \frac{\pi\gamma_0 \hbar \theta_{SH} \Delta}{2\alpha e t M_S} J$. The interesting thing is that, here, the no explicit DMI relevant term is included (as shown in the former section 5.1, D is linear related to K_u^{eff} , which is associated with DW width Δ). Also, the DW mobility at the low current density has the form of v_D/J_D and is thus related to the DW width Δ , saturation magnetization M_S and effective spin Hall angle θ_{SH} . The DW mobility ξ_{DW} obtained from Chapter 4 is plotted against the fitted value of v_D/J_D and a linear relationship with a slope of 1 is observed. An excellent correspondence of both D and ξ_{DW} obtained in two different ways manifests the robustness of the fitting and the simplified 1-D model.

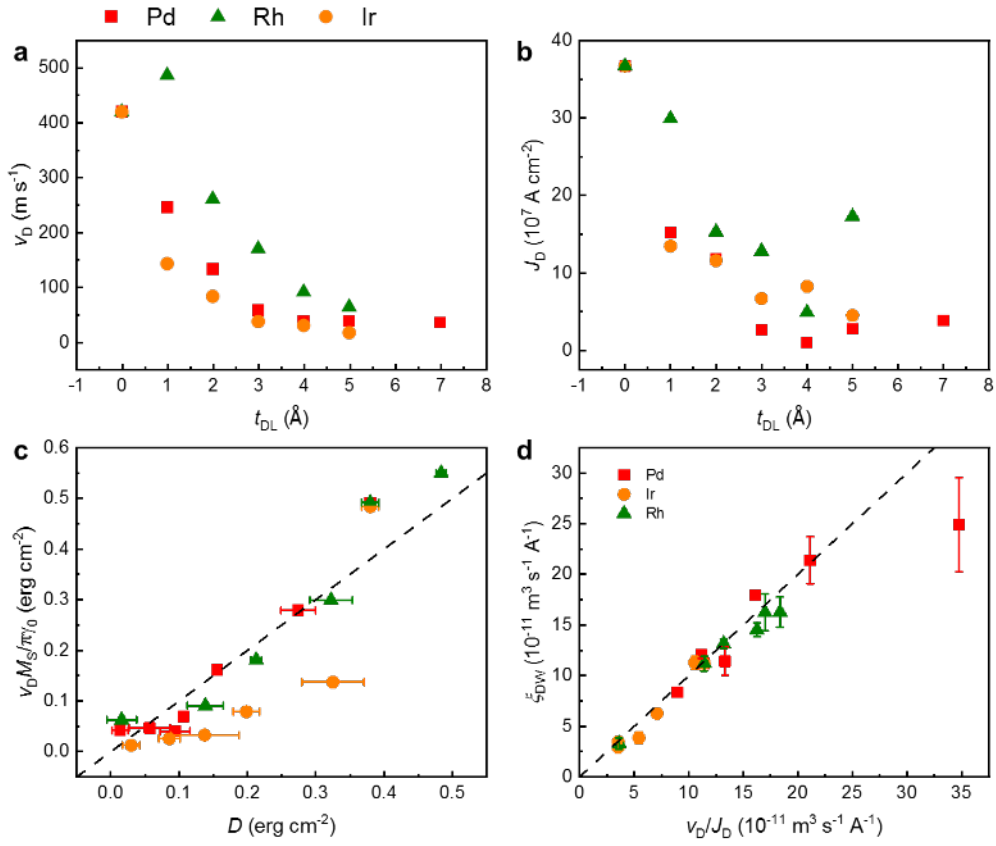


Figure 5-7: DL thickness dependence of v_D and J_D obtained from the $1-D$ model fitting and comparison of D s. The DL thickness dependence of v_D (a) and J_D (b). The calculated D from the fitted v_D is plotted against the D obtained from longitudinal field dependence (c); the dashed line is the line with a slope of 1. The DW mobility ξ_{DW} obtained from the slope of v - J curve at low current density is plotted against the v_D / J_D , the dashed line has a slope of 1.

5.4. Threshold spin current density based on DW mobility in FM structures with DLs

In the STT-driven DWM without any non-adiabatic torque case, because the effective momentum transfer from absorption of spin current, there exists intrinsic pinning in the form of $J_{\text{th}} = \frac{2eK\Delta}{\pi hP}$, where P is the polarization ratio, and K is the hard axis anisotropy. Such threshold current density shows its very intrinsic nature since it originates only from the magnetic textures [68, 69, 71, 76]. However, in the model of both SOT and ECT driven DWM, no threshold current density is included. Also, the threshold current density term J_{th} itself obtained in this work has no apparent correlations with a single spin-orbitronic parameter like either D or K_u^{eff} , as revealed in Figure 5.8. From the view of both application and physics, it will be of great importance to understand the origin of the J_{th} in both SOT and ECT-driven DWM cases.

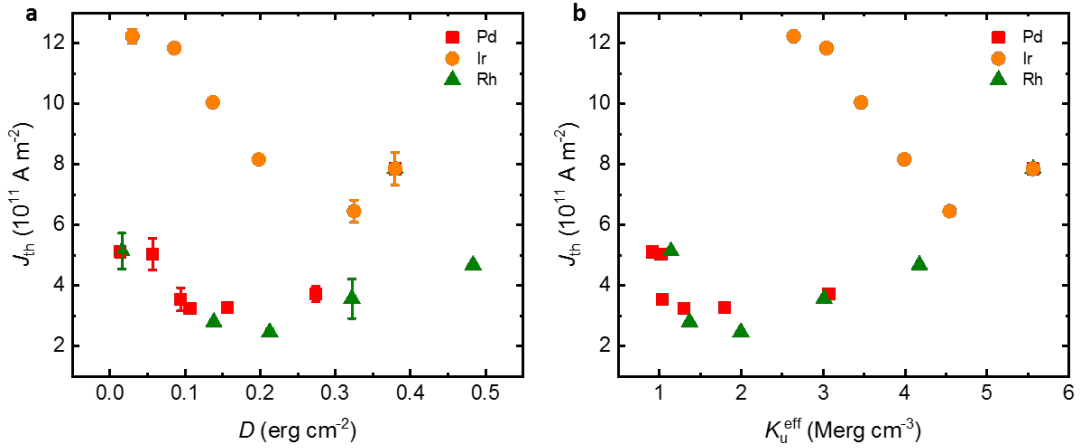


Figure 5-8: Threshold current density in FM structures plotted as a function of DMI constant and effective uniaxial anisotropy energy. The threshold current density is plotted as a function of interfacial DMI constant (a) and effective uniaxial anisotropy energy (b).

Chapter 5

Here, a threshold spin current density in the SOT driven case is defined in the following way: $J_{\text{th}}^s = \theta_{\text{SH}} J_{\text{th}}$. At the threshold current density, when the DW is about to move, the effective spin Hall field exerted on the DW has the form of $\frac{H_{\text{SHE}}}{J} J_{\text{th}}$, combining the saturation magnetization of the system, energy barrier that is responsible to J_{th} is thus defined. From the above derivation in section 5.2, the effective SOT efficiency term $M_S \frac{H_{\text{SHE}}}{J}$ or the effective spin Hall angle is proportional to $\alpha M_S \xi_{\text{DW}} / \Delta$, by plotting this term against the DL thickness, very different behavior could be observed in different DL materials, as shown in Figure 5.9. Here, the Gilbert damping parameter α is measured from the Optical Ferromagnetic resonance, and details of the measurements is contained in Appendix B.3. Unlike in the Ir case, where a monotonic decrease of the spin Hall effective field is observed with increasing DL thickness, in the Pd and Rh DL case, the spin Hall effective field will have a small increase once DL is introduced to the system and decreases with further increase in DL thickness. These behaviors could be understood in the following ways: in the Ir DL case, since the short spin diffusion length, the spin current generated from the Pt layer will be largely diffused; apart from this, the opposite spin Hall angle of Ir layer will further decrease the net spin current; in the Pd and Rh DL case, the long spin-diffusion length and negligible spin Hall angle of Rh layer makes the spin current generated from the Pt layer will be largely preserved, the slight increase of the thinnest DL thickness may be due to the enhancement of interfacial transparency for spin current as the replacing the $3d/5d$ interface (Co/Pt) to a $3d/4d$ interface (Co/Pd and Co/Rh).

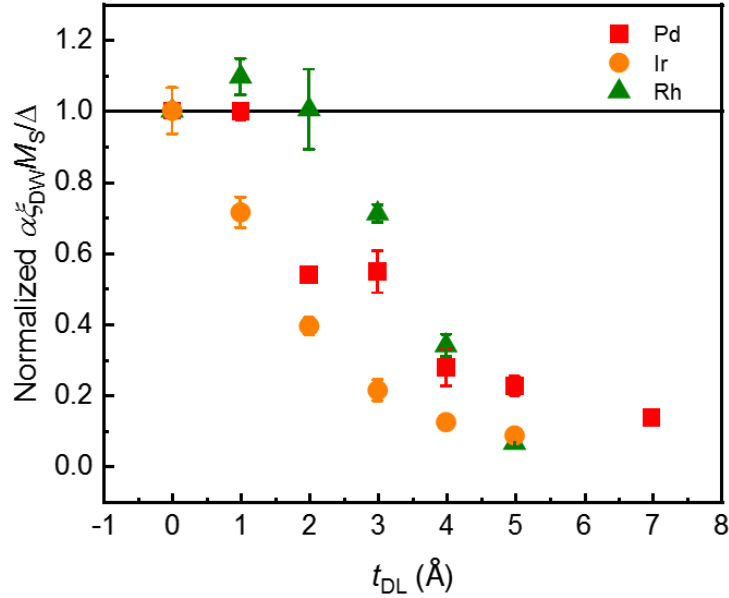


Figure 5-9: DL thickness of the effective θ_{SH} obtained from the DW mobility around the threshold current density.

From the above derivation, the threshold spin current density is thus proportional to the parameter of $\alpha \xi_{DW} M_S J_{th} / \Delta$. Interestingly, when the pinning potential is plotted against the effective magnetic anisotropy energy K_u^{eff} , two different linear relationships could be observed for $4d$ and $5d$ DLs. The value of K_u^{eff} where the pinning potential turns to zero in both linear fittings is exact the same value where D turns to zero in the $D-K_u^{eff}$ relationships, as shown in Figure. 5.5. When the pinning potential is plotted against the interfacial DMI constant D , a linear relationship crossing the origin, including all the samples, could be observed. Such a scenario could be understood in the following way: in the SOT-driven DWM case, the DW could only be motivated when a Néel wall configuration is fixed; in this work, since the interfacial DMI constant is obtained from CIDWM, once no sizable CIDWM could be detected, a zero-value D will then be detected—considering the $D-K_u^{eff}$ correlation revealed in Section 5.1 and Figure 5.5, it won't be surprising to find that two different relationships for the $4d$ and $5d$ are shown in Figure 5.10a.

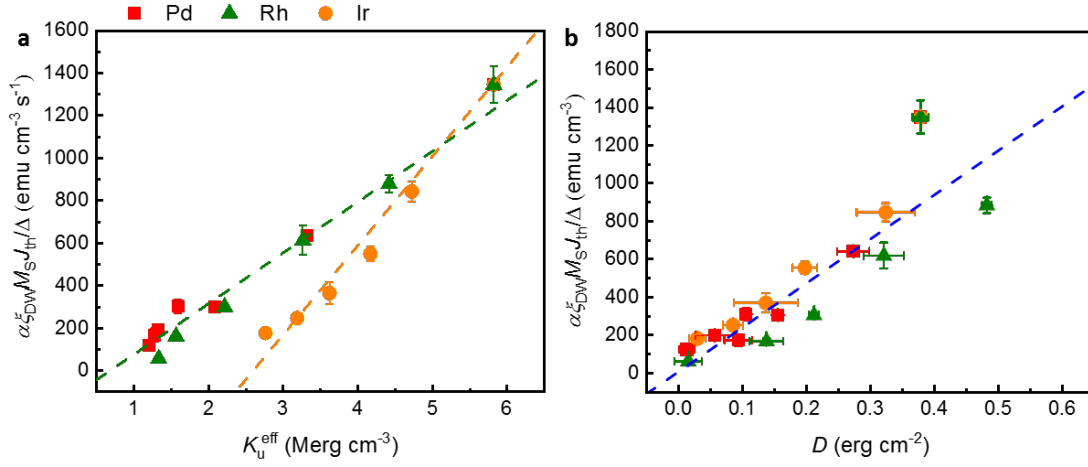


Figure 5-10: The pinning potential plotted as a function of effective uniaxial anisotropy energy and interfacial DMI constant. The dashed lines are the linear fittings of the 4d (olive) and 5d (orange) DLs for $\xi_{\text{DW}} M_S J_{\text{th}} / \Delta$ plotted as a function K_u^{eff} (a). The blue dashed line is the linear fitting of all samples for $\xi_{\text{DW}} M_S J_{\text{th}} / \Delta$ plotted as a function D (b).

	Pd/Rh	Ir
K_u^{eff} value where $\frac{\alpha \xi_{\text{DW}} M_S J_{\text{th}}}{\Delta} = 0$	0.68 Merg cm ⁻³	2.6 Merg cm ⁻³
K_u^{eff} value where $D = 0$	0.687 Merg cm ⁻³	2.531 Merg cm ⁻³

Table 5.1: Values of K_u^{eff} corresponding to zero threshold spin current density for CIDWM and $D=0$ for FM structures with 4d and 5d DLs.

5.5. Simplified 1-D model for ECT driven DWM and threshold spin current density based on DW mobility in SAF structures with DLs

By utilizing the same method in the FM structures discussed in Section 5.3, an effective pinning potential could also be defined in the SAF case. In the ECT-driven DWM model, since both layers may have different spin-orbitronic parameters, here, in simplicity, two identical magnetic sub-layers are not strongly coupled together with none exterior magnetic fields, STT-transfer terms, DMI-related terms, and demagnetizing terms are assumed. Thus, the LLG equation describing the ECT driven DWM can be rewritten in the following form:

$$\dot{q} = \frac{1}{2\alpha} \left[\mp \frac{\gamma\Delta\pi H_L^{SH}}{2} \cos\psi_L \pm \frac{\gamma\Delta\pi H_U^{SH}}{2} \cos\psi_U \right]$$

$$\dot{q} = \mp\gamma\Delta \left[-\frac{2J_{\text{ex}}}{M} \sin(\psi_L - \psi_U) \right]$$

$$\dot{q} = \pm\gamma\Delta \left[-\frac{2J_{\text{ex}}}{M} \sin(\psi_U - \psi_L) \right]$$

Solving the above equation sets lead to:

$$\dot{q} = \frac{1}{2\alpha} \left[\mp \frac{\gamma\Delta\pi H_L^{SH}}{2} \cos\psi_L \pm \frac{\gamma\Delta\pi H_U^{SH}}{2} \cos\psi_U \right]$$

$$\dot{q} = \mp\gamma\Delta \frac{2J_{\text{ex}}}{M} (-\sin\psi_L \cos\psi_U + \sin\psi_U \cos\psi_L)$$

Since when the DW is motivated, the magnetization in both layers could take arbitrary angles, the following relationship is then expected:

$$H_L^{SH} = \frac{8\alpha J_{\text{ex}}}{\pi M} \sin\psi_U$$

$$H_U^{SH} = \frac{8\alpha J_{\text{ex}}}{\pi M} \sin\psi_L$$

So, the DW velocity will have the following form:

Chapter 5

$$\dot{q} = \pm \frac{\pi\gamma\Delta}{4\alpha} \left[H_L^{SH} \sqrt{1 - \left(\frac{H_U^{SH}}{H_{ex}}\right)^2} + H_U^{SH} \sqrt{1 - \left(\frac{H_L^{SH}}{H_{ex}}\right)^2} \right]$$

where $H_{ex} = \frac{8\alpha J_{ex}}{\pi M}$ is defined as the exchange coupling torque field. From the above derivations, a conclusion could be reached as that: the DW velocity is proportional to $J \sqrt{1 - \left(\frac{J}{J_{ECT}}\right)^2}$ ($J_{ECT} = \frac{16e\alpha J_{ex}}{\pi\hbar\theta_{SH}}$) and has a maximum value of $\frac{2\gamma\Delta J_{ex}}{M}$ when the magnetizations in the upper and lower DWs are perpendicular to each other, which differs a lot with the SOT-driven DWM as shown in Figure 5.11. When the current is further increased, the DW velocity will quickly drop and goes to zero when $H_L^{SH} = \frac{8\alpha J_{ex}}{\pi M}$. One thing worth noting is that when the current density is low, the velocity is approximately linearly proportional to J with a fixed slope, which depends only on the SOT term. In the low current density region as $J \ll J_{ECT}$, DW velocity is written as $\dot{q} = \pm \frac{\pi\gamma\Delta}{4\alpha} \left(\frac{H_L^{SH} + H_U^{SH}}{J}\right)J$, so the DW mobility around this region will be proportional to the net SOT exerted on the whole system independent of the exchange coupling constant J_{ex} .

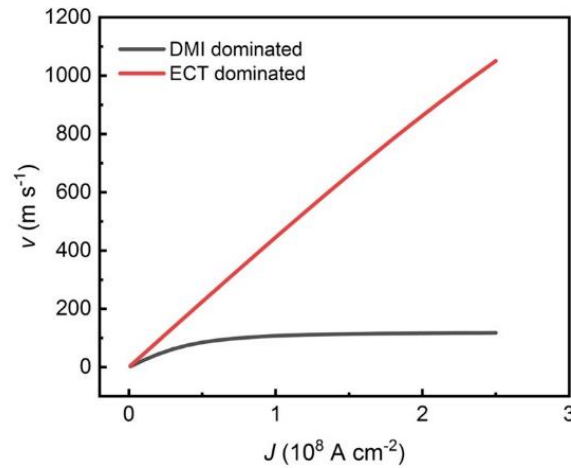


Figure 5-11: The illustration of the v - J curve of SOT-driven DW motion and ECT-driven DW motion.

Chapter 5

Based on the above derivation, the threshold spin current density will be defined in the same way as $J_{\text{th}}^S = \theta_{\text{SH}} J_{\text{th}}$, since the effective SOT field exerted on the DW around the J_{th} is $\frac{H_L^{\text{SH}} + H_U^{\text{SH}}}{J} J_{\text{th}}$ from above derivation, here, the M_S is the sublayer saturation magnetization. With some deduction, the pinning potential U_{th} is also proportional to $\alpha \xi_{\text{DW}} M_S J_{\text{th}} / \Delta$ (the DW width used here is the corresponding Δ in FM structures with the same DLs). By plotting this term against K_u^{eff} in corresponding FM structures with DL insertions, as shown in Figure 5.12, two different linear relationships could be observed for 4d and 5d DLs, a distinct difference from the FM structure is that the two linear fittings go across the origin. Besides, when plotting the pinning potential against D in the corresponding FM structures, no clear relations could be observed. These results indicate the pinning potential ECT-driven DWM has limited dependence on D but still depends on the sub-layer K_u^{eff} . It is rational since the anti-ferromagnetic coupling in SAF structure causes the small remnant magnetization, the demagnetization field is thus much smaller, and the Néel wall configuration is more easily fixed.

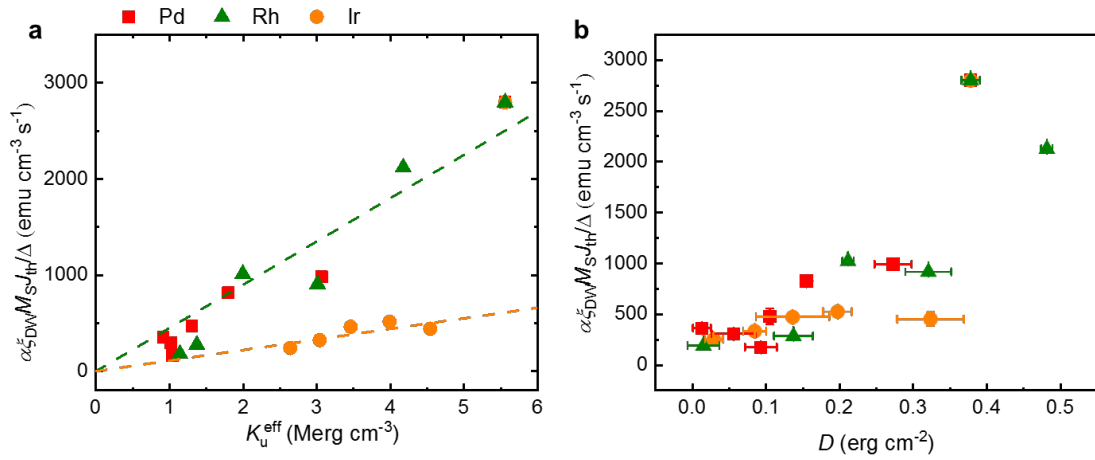


Figure 5-12: The threshold spin current density plotted as a function of effective uniaxial anisotropy energy and interfacial DMI constant of the lower magnetic layer. The threshold spin current density is plotted as a function of the effective uniaxial anisotropy energy (a) and interfacial DMI constant (b).

5.6. Illustration of v_{1g} by simulations from the 1-D analytical model for CIDWM under longitudinal magnetic field in SAF structure

The 1-D analytical model is further utilized to discuss the meaning of v_{1g} by simulating the longitudinal field dependence of the SAF CIDWM. The simulation parameters used are shown in Table 5.2. From the simulation results in Figure. 5.13, as the current density is increased, the spin Hall effective field and STT-related velocity also increase, so that the peak DW velocity v_{1g} is located at the point where the magnetization of the lower layer is oriented at an angle $\psi_L \sim \pi$ for a fixed up-down DW configuration (both the spin Hall effective field used in simulation and experiments are tiny compared to the exchange coupling field). (Note that for the up-down DW configuration $\psi_L \sim 0$). Such a scenario is understandable since, at this DW magnetization angle, the DW velocity contributed by the SOT is maximized in the lower layer (which has a larger SOT compared to the upper layer). Indeed, with increased current density, the peak position of the v - H_x curve becomes closer to zero field. When the current gets still larger as the velocity from SOT is comparable to $\gamma\Delta \frac{2J_{ex}}{M}$, the above assertion is broken, and v_{1g} will no longer be realized at $\psi_L = 0$ or π but fixed at the zero-field case. Also, note that the DW velocity contribution from the ECT ($-\frac{2J_{ex}}{M_L} \sin(\psi_L - \psi_U)$) is always dominant compared to the DMI-related contribution ($\frac{H_L^k}{2} \sin 2\psi_L - \frac{\pi}{2} H_L^D \sin \psi_L$) and the exterior longitudinal field contribution ($-\frac{\pi}{2} H_L^{lg} \sin \psi_L$). Thus, v_{1g} could be rewritten in the following form:

$$v_{1g} = \frac{\pi\gamma\Delta}{2\alpha} \left[\pm \frac{H_L^{SH}}{2} \pm \frac{H_U^{SH}}{2} \cos \psi_U \right]$$

$$v_{1g} = \pm \frac{2\gamma\Delta J_{ex}}{M} \sin \psi_U$$

$$\cos \psi_U = \frac{\pi H_U^{lg}}{2H_U^k}$$

A close correlation of the SOT exerted on the whole SAF structure and v_{1g} is revealed, which accounts for the different DL thickness dependence of v_{1g} in 4d and 5d DLs (Figure. 4.10g).

Chapter 5

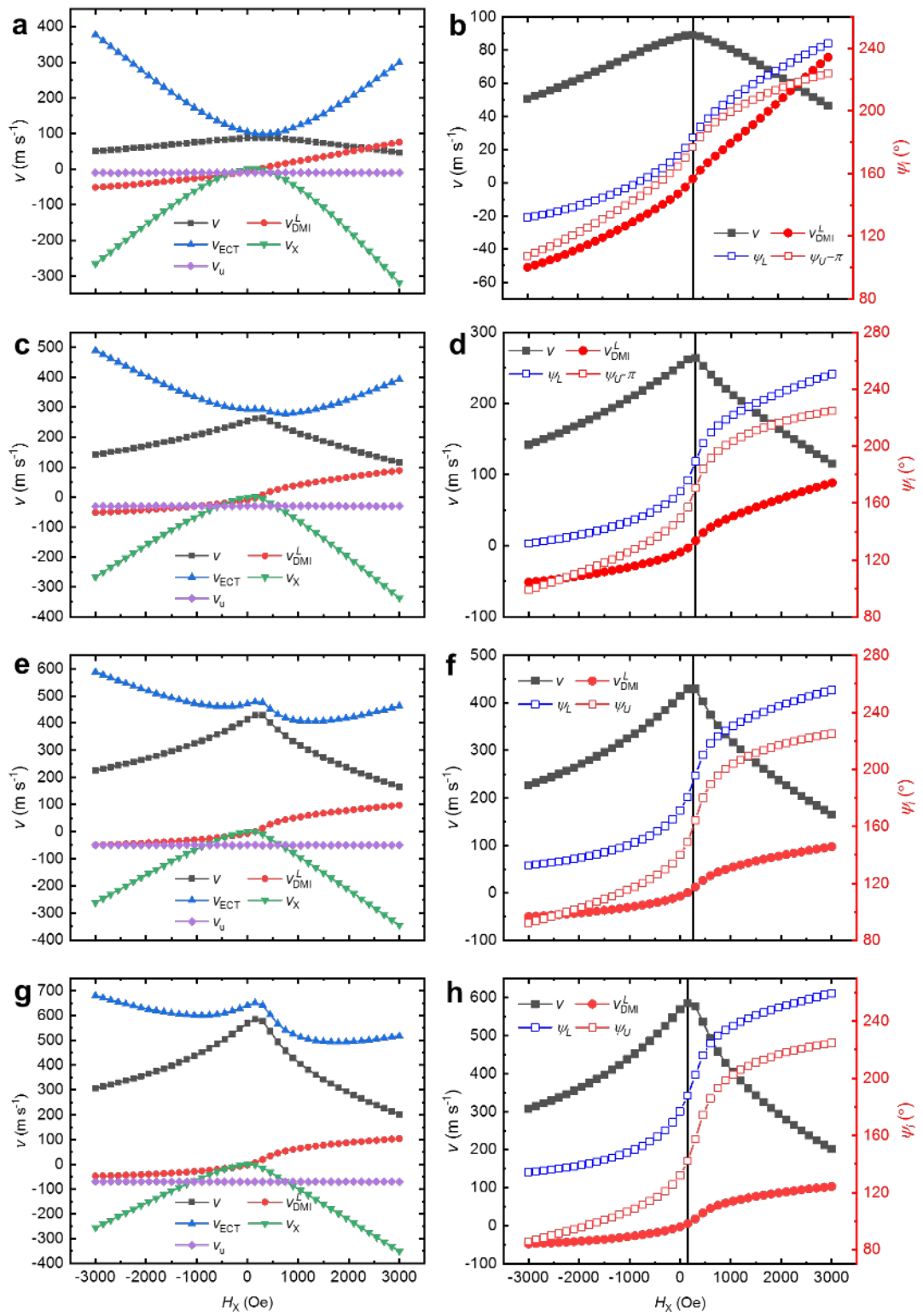


Figure 5-13: Simulation results based on a 1-D analytical model for the dependence of the SAF CIDWM versus the longitudinal field. Simulation results for the dependence of the SAF CIDWM versus the longitudinal field. (a), (c), (e), (g), and (i), contributions to the DW velocity in the lower (or upper) magnetic layer from different torques: total velocity (black square), DMI-related velocity (red circle), ECT-origin velocity (blue triangle), longitudinal-field induced velocity (green triangle) and STT-term velocity (violet diamond). (b), (d), (f), and (h), the response of SAF DW velocity (black square), DMI-related velocity (red circle), and DW magnetization angle of the upper (red unfilled square) and lower (blue unfilled square) layer to the longitudinal field.

	Figure. 5.12	(a) and (b)	(c) and (d)	(e) and (f)	(g) and (h)
1-D model simulation	Δ (nm)	4.3	4.3	4.3	4.3
	u (m/s)	10	30	50	70
	α_L	0.1	0.1	0.1	0.1
	α_U	0.1	0.1	0.1	0.1
	β_L	0	0	0	0
	β_U	0	0	0	0
	H_L^k (Oe)	1000	1000	1000	1000
	H_U^k (Oe)	1000	1000	1000	1000
	M_L/M_U	1	1	1	1
	J_{ex} (erg/cm ²)	-0.3	-0.3	-0.3	-0.3
	H_L^{SH} (Oe)	110	330	550	770
	H_U^{SH} (Oe)	40	120	200	280
	H_L^{DMI} (Oe)	-1000	-1000	-1000	-1000
	H_U^{DMI} (Oe)	400	400	400	400

Table 5.2: Magnetic parameters used in the simulation based on a 1-D analytical model for Figure. 5.12.

6. CIDWM in FM and SAF structures with Co-sputtered Pt/Pd DL insertion

In Chapters 4 and 5, CIDWM in FM and SAF structures with Pd, Rh, Ir, and Ru are investigated. Apart from the pure $4d$ and $5d$ DL materials, DL of co-sputtered Pt/Pd DL is also used for further examination of how the engineered interface changes the magnetic dynamics of CIDWM in FM and SAF structure. In this chapter, the co-sputtered Pt/Pd DL instead of pure $4d$ and $5d$ materials with a composition Pt 2.3 to Pd 1 and thickness varying from 1\AA to 7\AA is used. The same measurements of both magnetic properties and CIDWM as those in Chapters 4 and 5 are carried out. Based on these results, the comparisons with the $4d$ and $5d$ DL results are made.

6.1. Magnetic properties of FM and SAF structures with Co-sputtered $\text{Pd}_{0.31}\text{Pt}_{0.69}$

Hysteresis loop of raw FM and SAF films with $\text{Pd}_{0.31}\text{Pt}_{0.69}$ DLs are measured by SQUID with both in-plane and out-of-plane exterior field application direction to determine the saturation magnetization, effective uniaxial anisotropy field, and remnant to saturation magnetization ratio, as shown in Figure 6.1. Even though both the Pd and Pt are very close to Stoner Criteria [94-96, 99], unlike the Pd DL case where M_S oscillates around a constant value, the saturation magnetization in FM samples with $\text{Pt}_{0.5}\text{Pd}_{0.5}$ DLs shows a slightly descending trend when DLs becomes thicker. A relatively modest decrease of the effective uniaxial anisotropy field with increasing DL thickness is observed compared to Pd and Rh DL. The calculated effective uniaxial anisotropy energy K_u^{eff} in FM structures resemble the one in Ir DL case, and a relatively low M_R/M_S ratio is maintained with varying the DL thickness.

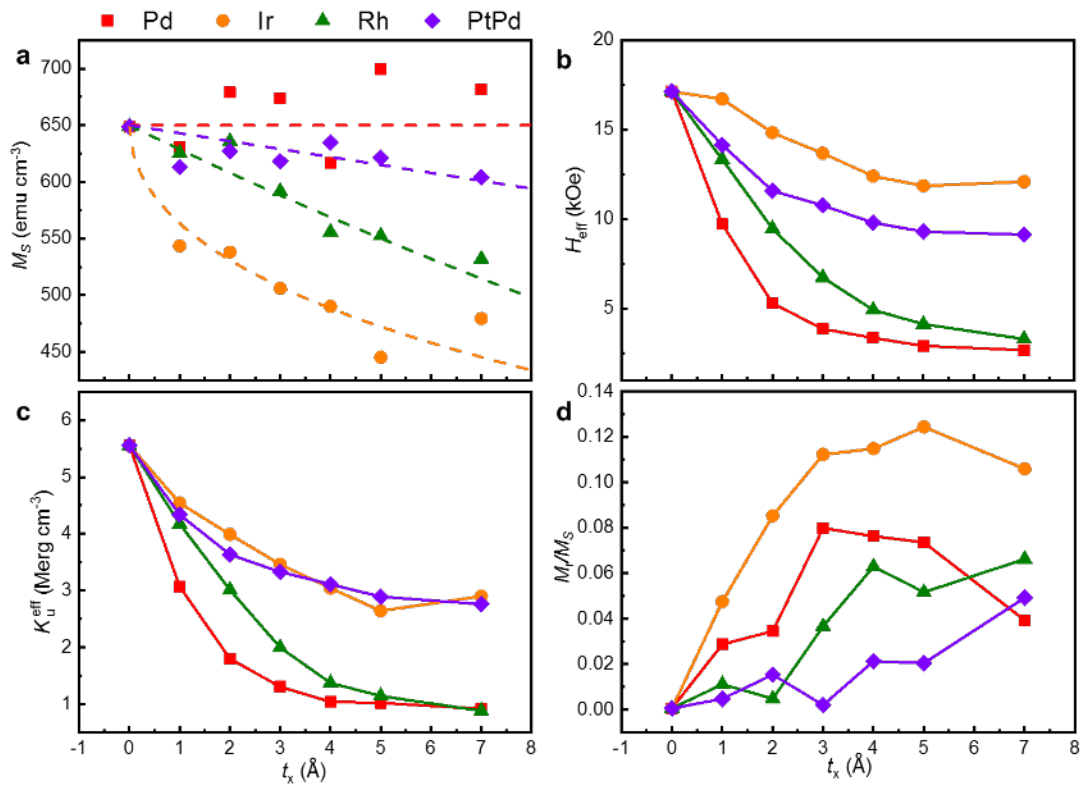


Figure 6-1: Magnetic properties obtained from the Magnetization Hysteresis loop in FM and SAF structures with co-sputtered Pd_{0.31}Pt_{0.69} DL. The thickness dependence of M_S (a), H_{eff} (b), and K_u^{eff} (c) in FM structures and M_R/M_S (d) in SAF structures. The red square, olive triangle, orange circle, and purple diamond correspond to Pd, Rh, Ir, and Pd_{0.31}Pt_{0.69} DL, respectively.

6.2. CIDWM in FM and SAF structures with Co-sputtered Pd_{0.31}Pt_{0.69} DL

The FM and SAF structures with Pd_{0.31}Pt_{0.69} DLs are patterned into the same racetrack devices with 50 μ m-long and 3 μ m-wide wire as those in other DLs cases. The CIDWM in both structures is measured by the differential Kerr microscopy with a current pulse length fixed at 10ns. Once the Pd_{0.31}Pt_{0.69} DL is introduced to the system, the CIDWM performances are well boosted with a substantial decrease J_{th} and well-improved DW velocity in both the FM and SAF structures, as shown in Figure 6.2. Unlike in the Pd and Rh case where the CIDWM quickly degrade beneath the reference when DLs are thick ($>3\text{\AA}$), the v - J curve is always above the reference FM and SAF structures.

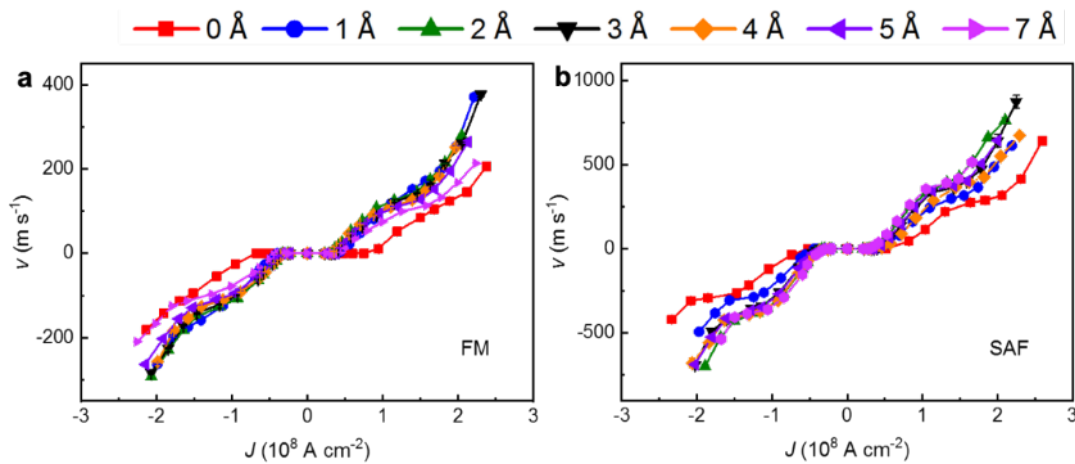


Figure 6-2: Current-induced chiral domain wall motion in FM and SAF structures with Co-sputtered Pd_{0.31}Pt_{0.69} DLs. The DW velocity v is plotted as a function of injected current density J in FM (a) and SAF (b) structure samples with Pd_{0.31}Pt_{0.69} DLs of different thicknesses.

Chapter 6

When examining the threshold current density J_{th} , DW mobility around threshold current density ξ_{DW} and DW velocity at a fixed current density ($\sim 1.2 \times 10^{12} \text{ A m}^{-2}$) v_C , distinct behaviors from the pure $4d$ DLs are observed (Figure 6.3).

In FM structure, J_{th} shows a similar trend with the $4d$ DL cases as a considerable decrease once the DL is introduced and slowly increases with increasing the DL thickness; ξ_{DW} also exhibits similar behavior with the $4d$ DL case but even when the DL thickness is thick ($> 4\text{\AA}$), ξ_{DW} still sustain a higher value than that in the reference FM sample; a more enormous increase of 150% in v_C is observed in $\text{Pt}_{0.5}\text{Pd}_{0.5}$ DL case and the descending trend is much more modest than those in Pd and Rh DL cases.

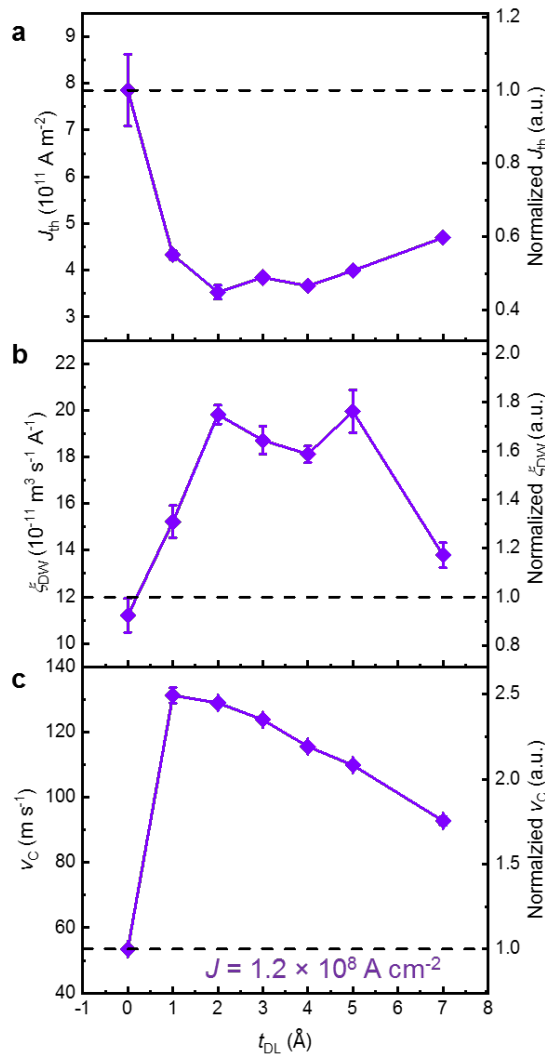


Figure 6-3: The DL thickness dependence of threshold current density, DW mobility, and DW velocity at a fixed current density in FM structures with $Pd_{0.31}Pt_{0.69}$ DL insertion. The threshold current (J_{th}) (a), DW mobility (ζ_{DW}) (b), and DW velocity at a fixed current density of $1.2 \times 10^{12} \text{ A m}^{-2}$ (v_c) (c) are plotted as a function of DL thickness. The right panel corresponds to the normalized value to the reference FM sample. The dashed lines are the corresponding value of the reference FM sample.

Chapter 6

In SAF structure, after the large decrease, unlike in the $4d$ DL case, a modest reduction still follows in J_{th} ; ξ_{DW} peaks at DL thickness of 2\AA , and then decreases with further increasing the DL thickness; v_C exhibits completely different behavior comparing to the $4d$ DL case as it remains almost constant after the initial colossal increase, as shown in Figure 6.4.

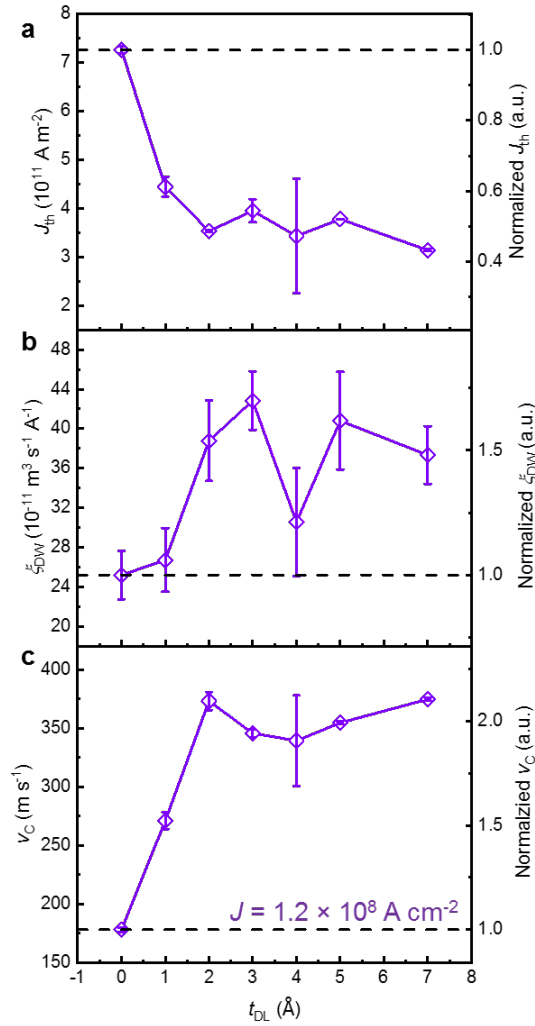


Figure 6-4: The DL thickness dependence of threshold current density, DW mobility, and DW velocity at a fixed current density in SAF structures with $\text{Pd}_{0.31}\text{Pt}_{0.69}$ DL insertion. The threshold current (J_{th}) (a), DW mobility (ξ_{DW}) (b), and DW velocity at a fixed current density of $1.2 \times 10^{12} \text{ A m}^{-2}$ (v_C) (c) are plotted as a function of DL thickness. The right panel corresponds to the normalized value to the reference SAF sample. The dashed lines are the corresponding value of the reference SAF sample.

6.3. Longitudinal field dependence of CIDWM in FM and SAF structures with Co-sputtered Pd_{0.31}Pt_{0.69} DLs

The longitudinal field dependence of CIDWM is examined to obtain the DMI effective field H_{DMI} in FM structure and fastest velocity with the assistance of longitudinal field v_{lg} in the SAF structure, as shown in Figure 6.5. The current density used in all measurements is fixed at $1.2 \times 10^{12} \text{ A m}^{-2}$, same as in the $4d$ and $5d$ DL cases.

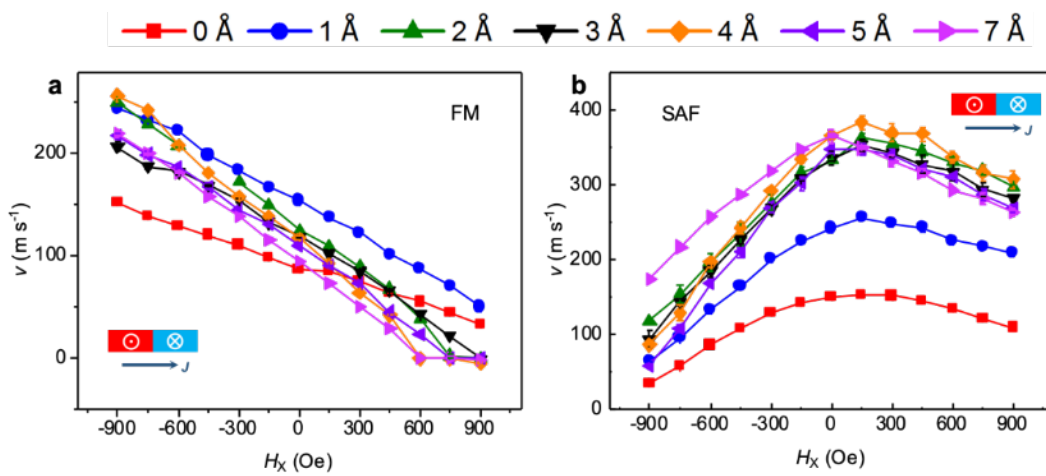


Figure 6-5: Longitudinal field dependence of the DW velocity in FM and SAF structure with different DL thicknesses. The DW velocity v is plotted as a function of exterior longitudinal magnetic field H_x in FM (a) and SAF (b) structure samples with Pd_{0.31}Pt_{0.69} DLs of different thicknesses.

Chapter 6

DMI constant D is obtained through the same calculation method as used in Chapter 5. As revealed in Figure 6.6, when D is plotted against K_u^{eff} together with other DLs, the $\text{Pd}_{0.31}\text{Pt}_{0.69}$ DL data points fall on the $4d$ DL groups and gather around the 1\AA thick pure Pd DL data point except for the 1\AA case. Interestingly, when DL gets thicker in the SAF case, the v_{lg} of $\text{Pd}_{0.31}\text{Pt}_{0.69}$ DL saturate at the value the same as the v_{lg} of 1\AA Pd DL. Such a scenario indicates that the very interfacial nature of these spin-orbitronic parameters and by changing both the composition and thickness of the alloy DL, fine-tuning of the spin-orbitronic parameters is accessible.

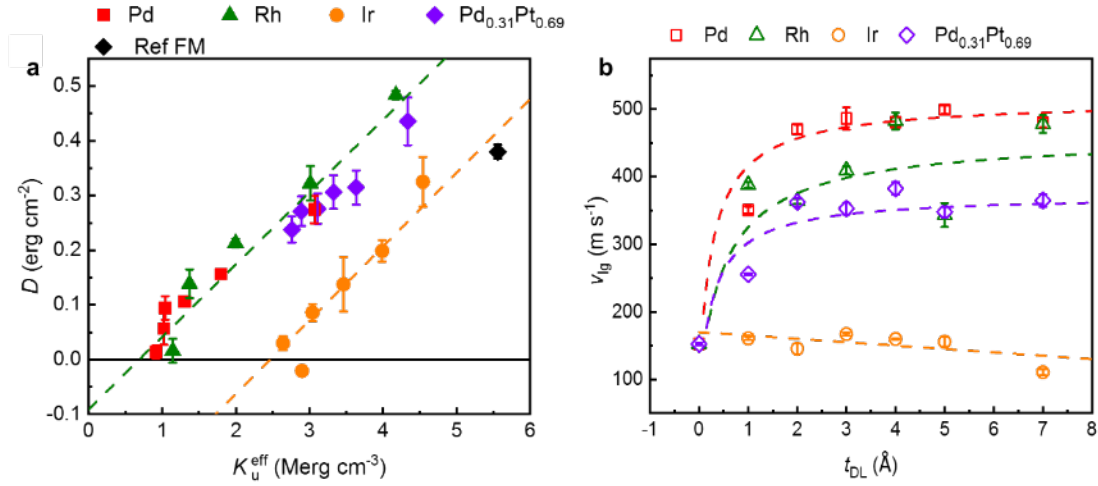


Figure 6-6: Interfacial DMI constant as a function of effective uniaxial anisotropy and DL thickness dependence of v_{lg} . The interfacial DMI constant is plotted as a function of K_u^{eff} in FM structures with all other DLs used in Chapters 4 and 5 (a); the v_{lg} in SAF structure is plotted against the DL thickness in all DL cases (b). The red square, olive triangle, orange circle, and purple diamond correspond to Pd, Rh, Ir, and $\text{Pd}_{0.31}\text{Pt}_{0.69}$ DL, respectively.

6.4. Effective spin Hall angle and threshold spin current density based on DW mobility and threshold current density in FM and SAF structures with Co-sputtered Pd_{0.31}Pt_{0.69} DLs

From the above parameters obtained from the v - J curve in both FM and SAF structures, the effective spin Hall angle ($\propto \alpha \xi_{\text{DW}} M_S / \Delta$) and threshold spin current density ($\propto \alpha J_{\text{th}} \xi_{\text{DW}} M_S / \Delta$) are also examined. Here, Gilbert damping parameter of Pd 1Å ($\alpha \sim 0.08608$) is used for the samples with DLs as the resemblance between them. As shown in Figure 6.7, interestingly, both the effective spin Hall angle exerted on the whole ferromagnetic layer show an oscillatory behavior. In FM structure, an increase up to 20% is observed when DL thickness is 2Å, which is way more extensive than those observed in $4d$ DL cases. Besides, the effective spin Hall angle is well beyond the reference FM sample until the DL thickness is 7Å. In the SAF structure, the effective spin Hall angle oscillates around the value in the reference SAF sample and peaks at the same DL thickness with FM structures where the DLs are just 1 and 2 monolayers thick.

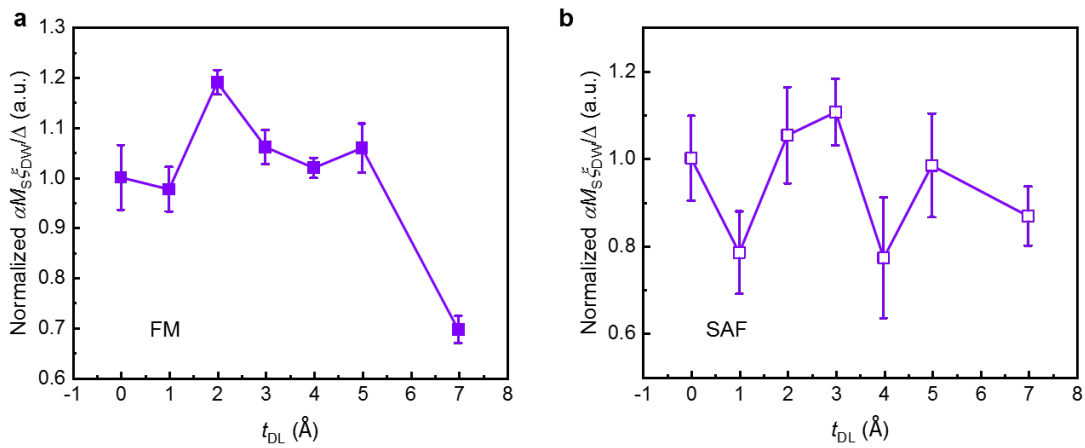


Figure 6-7: DL thickness of the effective spin Hall angle obtained from the DW mobility around the threshold current density in the FM and SAF structures. The filled and open symbols represent FM (a) and SAF structures (b), respectively.

Chapter 6

When the threshold spin current density is plotted as a function of K_u^{eff} , as shown in Figure 6.8, the $\text{Pd}_{0.31}\text{Pt}_{0.69}$ DL case falls entirely on the $4d$ DL groups in both FM and SAF structures. Comparing to the pure Pd DL case, the data points of the $\text{Pd}_{0.31}\text{Pt}_{0.69}$ DL case gathered mostly around the region of the Pd DL 1\AA region, which is consistent with the measurement results in former sections.

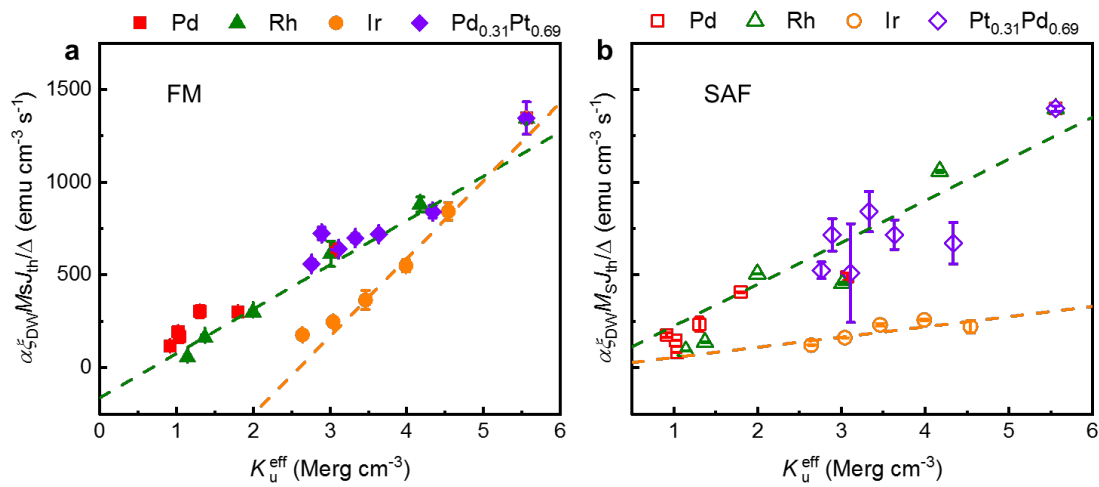


Figure 6-8: The threshold spin current density plotted as a function of effective uniaxial anisotropy energy in FM and SAF structures. The filled and open symbols represent the FM and SAF structures, respectively.

7. CIDWM in FM structure with sandwiched HM layer

In the previous chapters, the very interfacial nature of the spin-orbitronic parameters has been illustrated with the sub-atomically thin DLs composed of $4d$, $5d$ materials, and co-sputtered Pt/Pd. In this chapter, a FM/HM combination with sandwiched structure of the HM layer formed of $\text{Co}(3\text{\AA})\text{Ni}(7\text{\AA})\text{Co}(1.5\text{\AA})/\text{Pt}(x\text{\AA})/\text{Pd}(2\text{\AA})/\text{Pt}((15-x)\text{\AA})$, where $x \sim 1$ to 5 , is used to further investigate the effects of interfacial engineering on the magnetic dynamics.

7.1. Magnetic properties of FM structure with sandwiched HM layer

The hysteresis loop of raw FM films with sandwiched HM layer is measured by SQUID with both in-plane and out-of-plane exterior field application direction to determine the saturation magnetization and effective uniaxial anisotropy field. Interestingly, the saturation magnetization M_s increases with increasing upper Pt thickness and peaks at $x=3\text{\AA}$, then drops with further increasing the Pt thickness, as shown in Figure 7.1. However, the values of M_s in all these samples are very close to each other since both Pt and Pd are close to the *Stoner criteria*. The effective uniaxial anisotropy field H_K^{eff} shows an upward trend and saturates when upper Pt thickness reaches 4\AA , which is the same as the trend observed in lately calculated K_u^{eff} .

Chapter 7

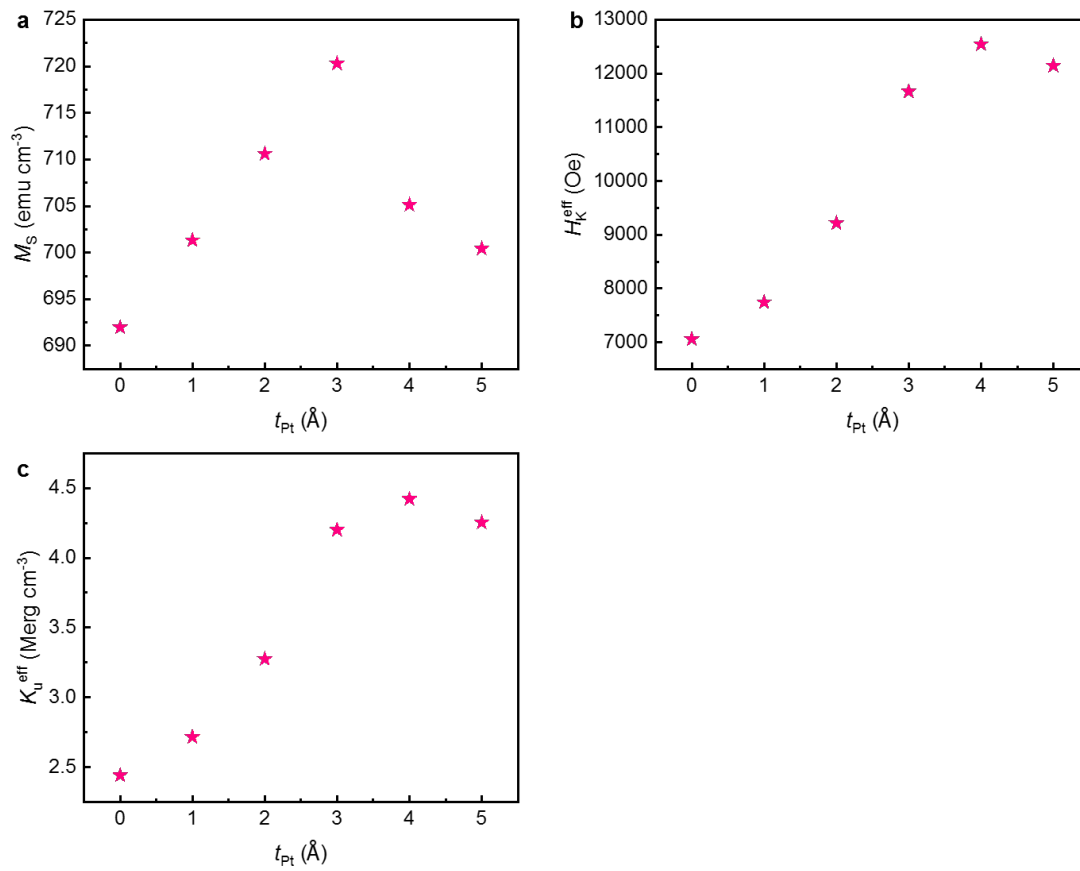


Figure 7-1: Magnetic properties obtained from the Magnetization Hysteresis loop in FM structure with sandwiched HM layer. The upper Pt layer thickness dependence of M_S (a), H_{eff} (b), and K_u^{eff} (c) in FM structures.

7.2. CIDWM in FM structure with sandwiched HM layer

After being patterned into racetrack devices of the same size in previous chapters, the CIDWM in FM structures with a sandwiched HM layer is measured with a current pulse length fixed at 10ns. With increasing the upper Pt layer thickness, the CIDWM degrades from the original Pd DL 2Å case, with an increasing threshold current, decreasing DW mobility around the threshold current density and a lowered DW velocity at a fixed current density ($1.2 \times 10^{12} \text{ A m}^{-2}$). With a thicker upper Pt layer, the sandwiched sample shows a saturation behavior that resembles the pure Pt layer case as a result of the formation of pure Co/Pt interface, as shown in Figure 7.2.

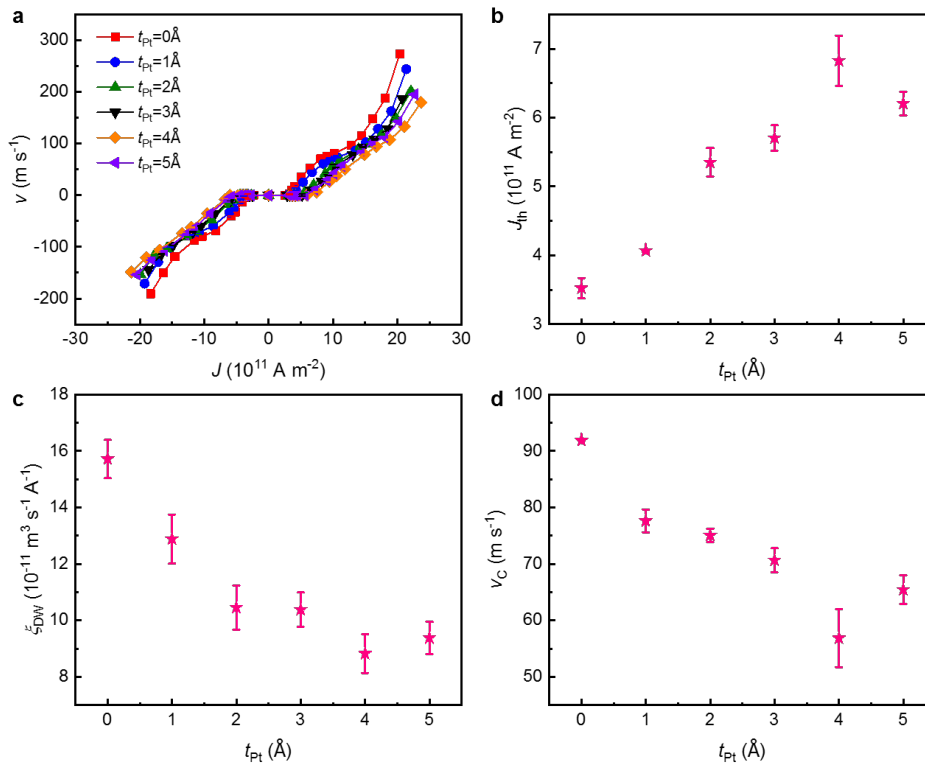


Figure 7-2: Current-induced chiral domain wall motion in FM structure with sandwiched HM layers. The DW velocity is plotted against the injected current density of samples with different upper Pt layer thickness (a); the upper Pt layer thickness dependence of J_{th} (b), ξ_{DW} (c) and v_C (d) are also summarized.

Chapter 7

When the DMI constant is determined from the longitudinal field dependence of the DW velocity and plotted as a function of uniaxial anisotropy energy K_u^{eff} , together with the $4d$ and $5d$ cases, it forms a line across the $4d$ line and the $5d$ line, as shown in Figure 7.3. Such a scenario is predictable since the Co/Pd interface is gradually replaced with the Co/Pt interface. When the upper Pt layer is thick enough, the whole system should be just like the pure Pt layer, as indicated in the v - J curves.

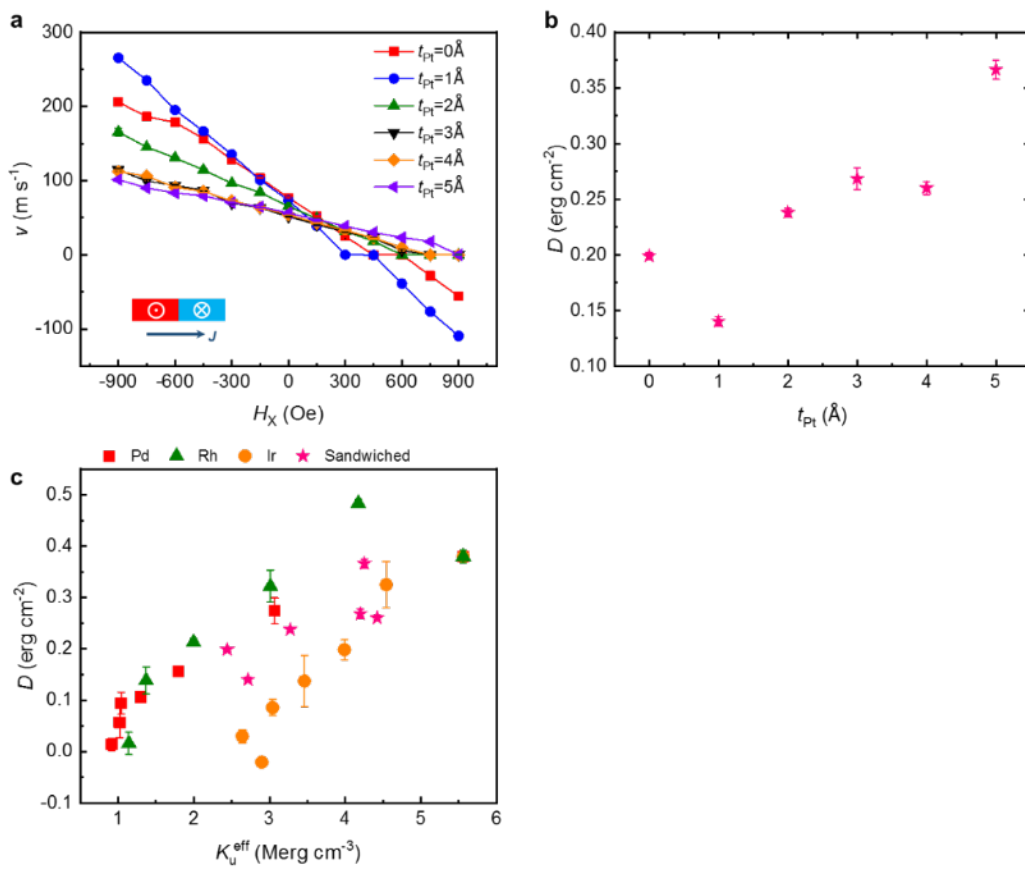


Figure 7-3: Longitudinal field dependence of the DW velocity in FM structure with sandwiched HM layer and calculated DMI constant. The longitudinal field dependence of an up-down DW driven by a positive current pulse injection is examined (a); the calculated DMI constant D is plotted against the upper Pt thickness dependence (b); K_u^{eff} dependence of D in samples with sandwiched HM layer is compared with other DL cases (c).

Chapter 7

The effective SOT efficiency and effective pinning potential are examined by the same method described in Chapter 5.4. With increasing the upper Pt thickness, again, the effective SOT efficiency also shows a small peak when upper Pt thickness is around one monolayer thick (3Å). Just like in the D - K_u^{eff} relationship, where the sandwiched samples belong to neither the $4d$ nor $5d$ groups, for the pinning potential, not surprisingly, the data points also go across the two groups.

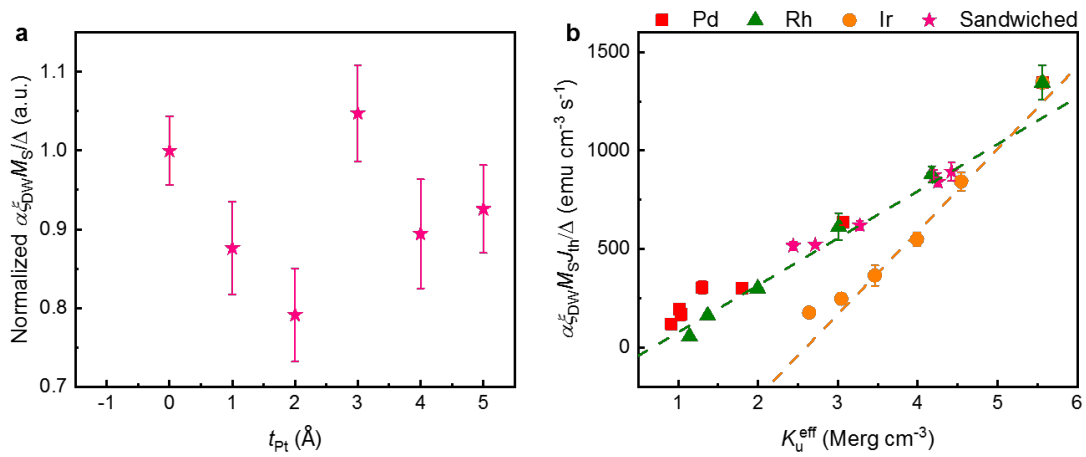


Figure 7-4: The upper Pt layer thickness dependence of effective spin Hall angle and threshold spin current plotted as a function of effective uniaxial anisotropy energy in FM structure with sandwiched Pt HM.

8. Transport measurement for FM structure with DL insertions

After measuring the CIDWM in both FM and SAF structures with different DL insertions, the transport properties of the FM structure with DL insertions are also examined. In this Chapter, results obtained from transport measurements, including Hall measurement, second harmonic measurement of the same FM structures with DLs used in the former Chapters are present. Modification of the interface by the introduction of DLs causes significant changes in the anomalous Hall resistivity, planar Hall resistance, and spin-orbit torques at the FM/DL/HM interfaces.

8.1. Hall measurement for the FM structure with DL insertions

The transverse resistance (anomalous Hall resistance) and the longitudinal resistance is determined by a typical Hall measurement in a Hall bar device processed by photolithography and Ar ion milling. Electrodes composed of Au(20nm)/Ru(2nm) are deposited at the end of the Hall channel by DC-sputtering and lift-off process. A DC of 10 μ A is applied along the x -direction of the device, and the Hall signal in the y -direction together with the longitudinal resistance is measured through a four-terminal method with sweeping the exterior magnetic field in the out-of-plane direction, as shown in Figure 8.1a.

The measured anomalous Hall resistance (R_{xy}) and the longitudinal resistance (R_{xx}) is plotted as a function against the applied exterior z -field. A clear hysteresis loop in R_{xy} could be observed due to the ferromagnetic nature of the samples, as shown in Figure 8.1b. The following equations determine the anomalous Hall resistivity and longitudinal resistivity [84, 100, 101]:

$$\rho_{xy} = R_{xy}t$$

$$\rho_{xx} = R_{xx}tw/l$$

Chapter 8

Where t is the thickness of the whole metallic layer, w is the channel width, and l is the channel length. With increasing the DL thickness, both the ρ_{xy} and ρ_{xx} are decreasing no matter the DL type. This phenomenon is attributed to the change of interfacial scattering conditions due to the modifications by DL insertions at the Co/Pt interface.

There are three main mechanisms responsible for the anomalous Hall signal: the intrinsic mechanism, the extrinsic mechanism of skew scattering and side-jump [73, 84, 100, 101]. Different behaviors in the relationship between ρ_{xy} and ρ_{xx} could be observed when dominant mechanisms are different. In a skew scattering dominating system, ρ_{xy} is often proportional to ρ_{xx} , which means $\beta = 1$. In the side-jump and intrinsic mechanism dominating case, ρ_{xy} is proportional to ρ_{xx}^2 , that is, $\beta = 2$. At room temperature, when ρ_{xy}/ρ_{xx} is plotted against ρ_{xx} in FM samples with different DLs in Figure 8.1c, a linear relationship is observed in the Pd and Rh DL cases, but for the Ir DL case, a non-linear curve is present. Once the Ir DL is introduced to the system, the data points immediately deviate from the reference FM sample and form a distinct group by itself.

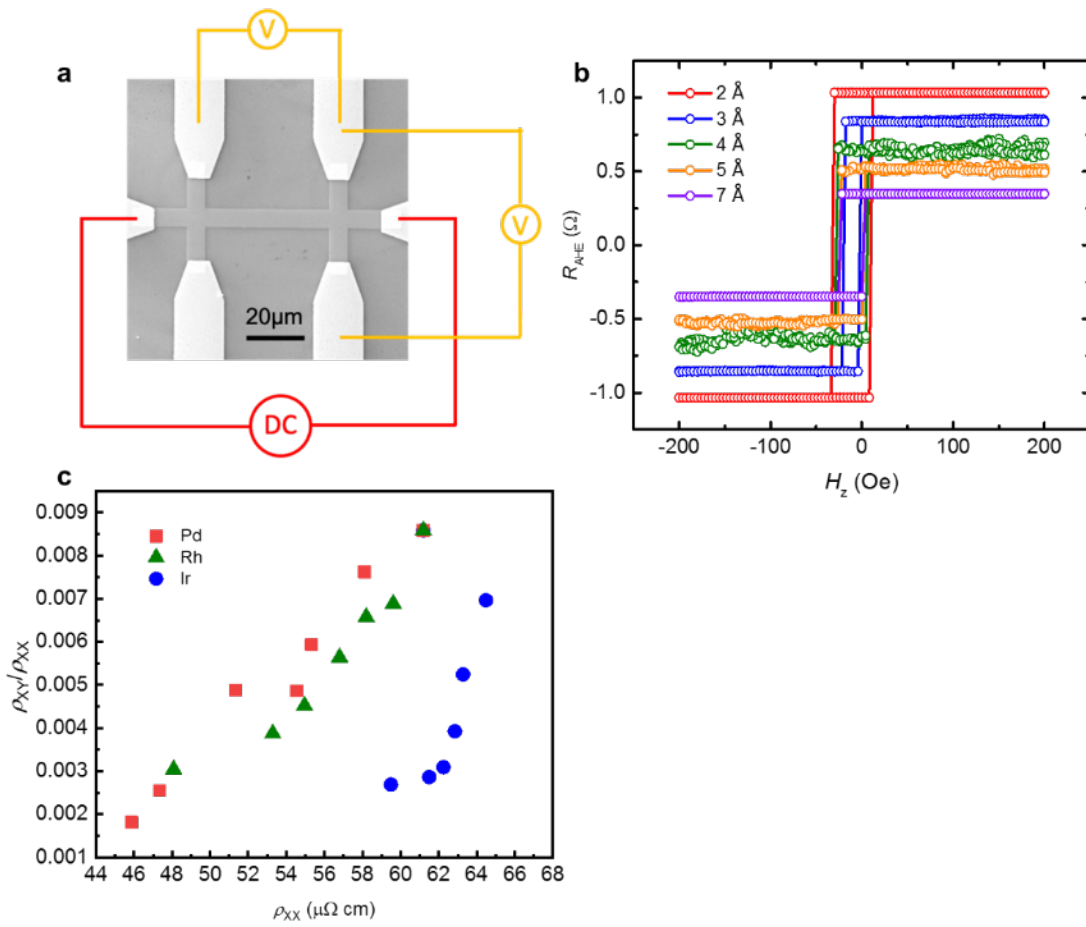


Figure 8-1: Device structure and experimental set-up for the Hall measurements and measurement results. (a) The fabricated Hall bar device with the electrode at the end; (b) The hysteresis R - H loop in the FM samples with different Pd DL thicknesses; (c) The summarized transverse resistivity to longitudinal resistivity ratio against the longitudinal resistivity in FM samples with various DL materials (Pd, Rh, Ir) and thicknesses.

Chapter 8

The planar Hall effect is also examined in Pd and Rh DL cases by sweeping an in-plane field application in the direction 45° deviated from the x -direction. The origin of the planar Hall effect comes from the magnetization-direction dependent scattering of electrons [102, 103], and the Hall signal could be interpreted with the following equation taking the planar Hall effect contributions [104-106]:

$$R_H = R_{\text{AHE}} \cos \theta + R_{\text{PHE}} \sin^2 \theta \sin 2\varphi$$

Here, θ is the angle between the magnetization and z -axis, while φ is the angle between the magnetization and the x -axis. When φ is fixed at 45° , due to the different symmetry dependence on the exterior field application, the anti-symmetric part of the Hall signal represents the anomalous Hall signal while the symmetric part is the planar Hall signal, as shown in Figure 8.2. By increasing the Pd DL thickness, both the R_{AHE} and R_{PHE} decreases quickly, but the planar Hall to anomalous Hall ratio $R_{\text{PHE}}/R_{\text{AHE}}$ is calculated to be almost linearly increasing. In the Rh DL case, the same behavior is observed but a modest increase of $R_{\text{PHE}}/R_{\text{AHE}}$ is observed.

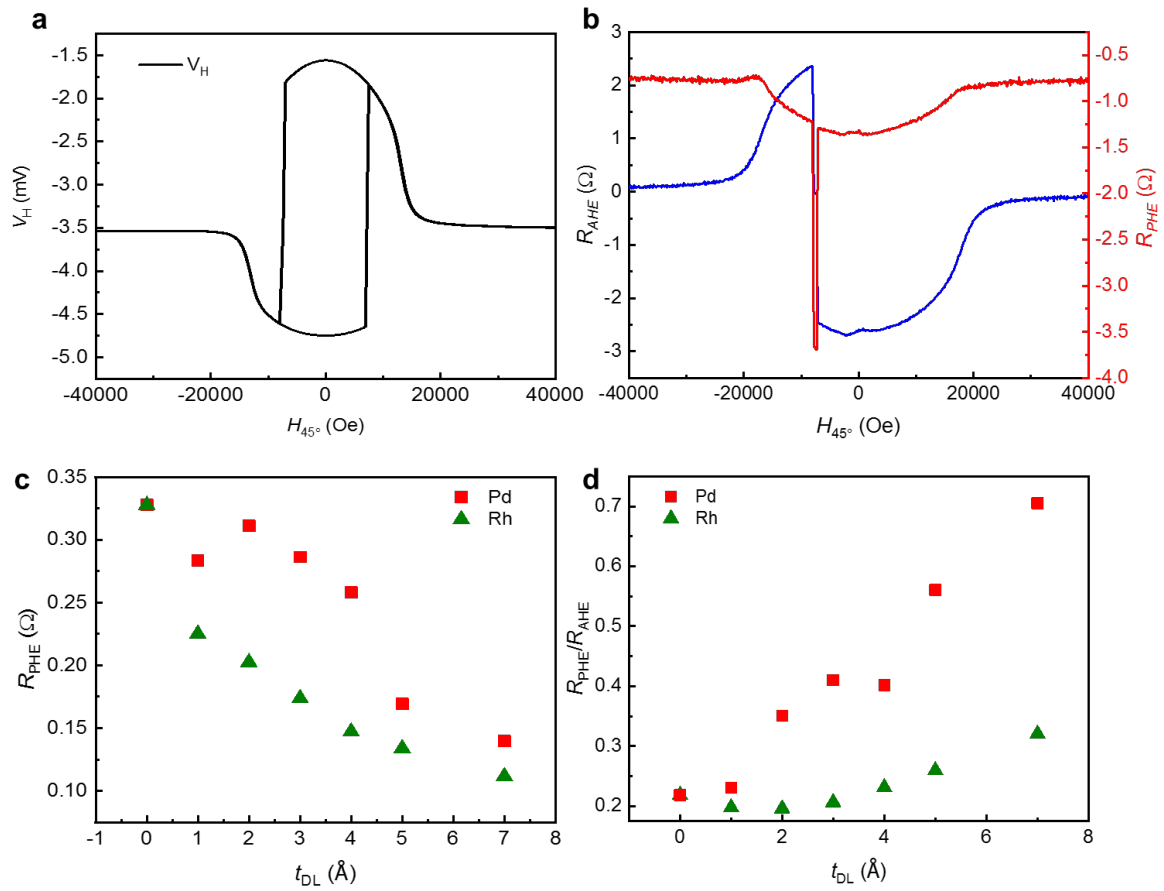


Figure 8-2: The Hall measurement to obtain planar Hall resistance. (a) The typical Hall voltage against exterior field curve of FM sample with 2 \AA Pd DL when sweeping the in-plane magnetic field in the 45 $^\circ$ direction; (b) The separated anomalous Hall resistance (anti-symmetric part of the signal in Fig. 8.2a, blue) and planar Hall resistance (symmetric part of the signal in Fig. 8.2b, red); (c) The DL thickness dependence of the planar Hall resistance in Pd and Rh DL cases; (d) The DL thickness dependence of planar Hall resistance to anomalous Hall resistance ratio in the Pd and Rh DL cases.

8.2. Second-harmonic measurement for the FM structure with Pd and Rh DLs

To look into the SOT in the FM structure with Pd and Rh DLs, the second-harmonic Hall signals are measured. An AC of a sine wave with the frequency of 13Hz is injected into the wire in the x -direction, and the in-phase first harmonic Hall voltage signal V_H^ω and out-of-phase second harmonic Hall voltage $V_H^{2\omega}$ are measured by a lock-in technique while the exterior field is sweeping in longitudinal (x -axis) and transverse (y -axis) directions (Figure 8.3).

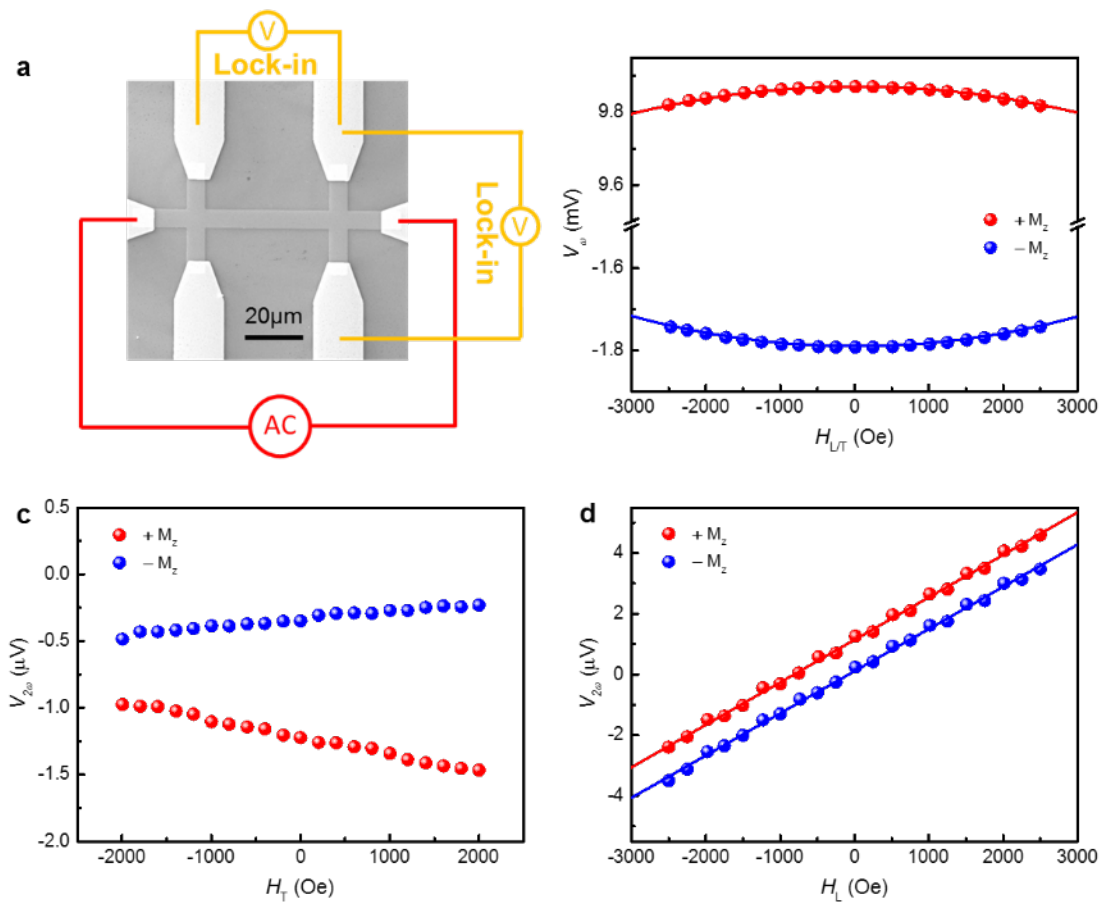


Figure 8-3: Experimental set-up for the harmonic Hall measurement and obtained harmonic Hall signals. (a) The fabricated Hall bar device with the electrode at the end; (b) the measured in-phase first harmonic Hall signal with sweeping the exterior magnetic field in longitudinal/transverse direction; (c) and (d) the measured out-of-phase second harmonic Hall signal with sweeping transverse and longitudinal field. The red and blue circles represent the magnetization of up and down direction.

Chapter 8

After the first and second harmonic Hall signals (V_H^ω and $V_H^{2\omega}$) are obtained, the longitudinal and transverse effective field ($H_{L(T)}$) are obtained from the following equations [104-107]:

$$H_{L(T)} = -2 \frac{\partial V_H^{2\omega} / \partial H_{X(Y)}}{\partial^2 V_H^\omega / \partial H_{X(Y)}^2}$$

Since the exterior field is swept in the x and y direction, the Hall voltage will contain both the anomalous Hall and planar Hall signal, and the Damping-like and Field-like effective field will be derived in the following form regarding the planar Hall resistance to anomalous Hall resistance ratio $\chi = R_{PHE}/R_{AHE}$.

$$H_{DL(FL)} = \frac{H_{L(T)} \pm 2\chi H_{T(L)}}{1 - \chi^2}$$

Depending on the magnetization direction is up (+ z -direction) or down (- z -direction), the $\pm 2\chi H_{T(L)}$ term take + or - symbol. The detailed deduction is presented in Appendix A.

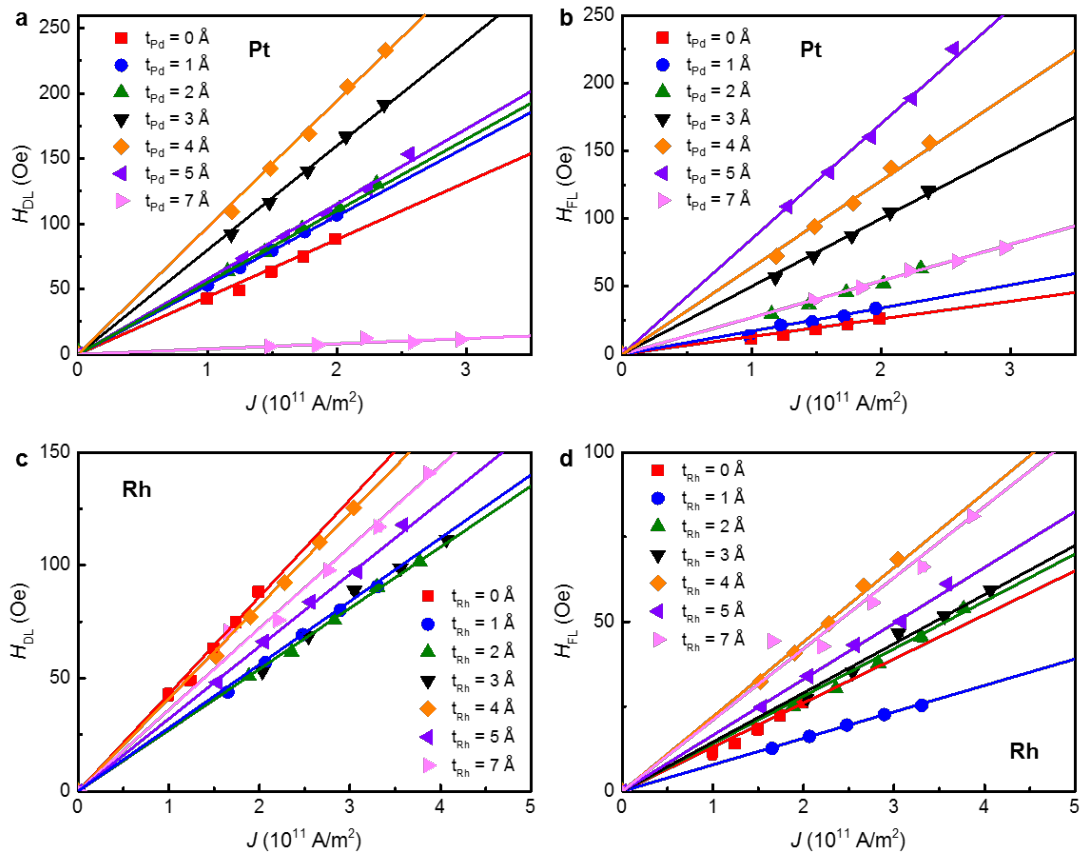


Figure 8-4: The calculated Damping-like and Field-like effective field plotted as a function of injected current density in Pd and Rh DL cases. The Damping-like effective field and Field-like effective field are plotted against the injected current density in Pt (a and b) and Rh (c and d) DLs.

Chapter 8

After plotting the effective field term against the current density flowing in the whole system, the Damping-like and Field-like effective field efficiency could be calculated with the following equation [73, 82, 108, 109]:

$$\theta_{\text{DL(FL)}} = \frac{2e\mu_0 M_S t_{\text{FM}}}{\hbar} \frac{H_{\text{DL(FL)}}}{J}$$

Here, e is the elementary charge, \hbar is the Planck constant, M_S is the saturation magnetization, t_{FM} is the thickness of the ferromagnetic layer and $\frac{H_{\text{DL(FL)}}}{J}$ is the slope of the linear fitting for $H_{\text{DL(FL)}}$ plotted against current density J .

Hence, the DL effects on the SOT are compared by plotting the torque efficiencies against the DL thickness in Figure 8.5. As shown in Chapter 5, the effective SOT efficiency (spin Hall angle) exerted on the DW has already been investigated for different DL insertions through the 1-D model for SOT-driven DWM, distinct behaviors are observed in this second harmonic transport measurement.

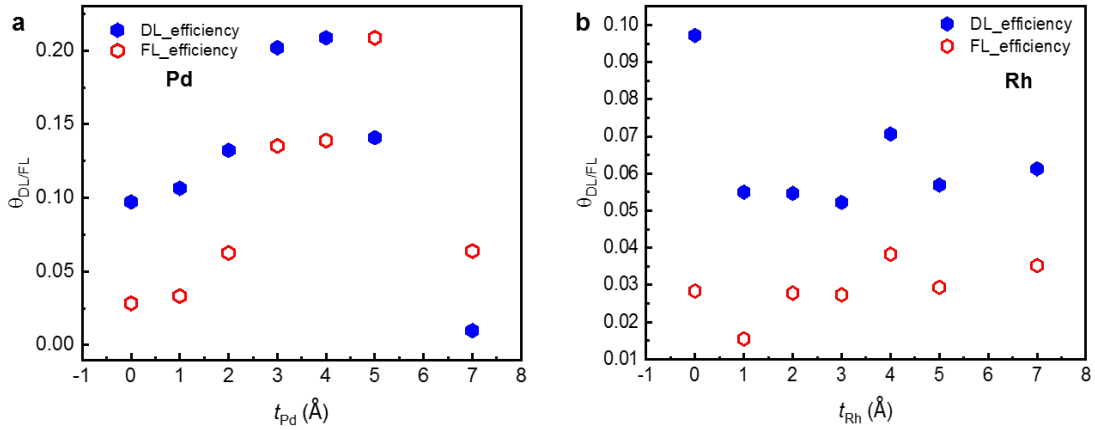


Figure 8-5: DL thickness dependence of calculated effective Damping-like and Field-like torque efficiency. The calculated Damping-like and Field-like torque efficiency are plotted against the DL thickness in FM structures with Pd (a) and Rh (b) DLs. The blue filled hexagon and red unfilled hexagon represent the Damping-like torque efficiency θ_{DL} and the Field-like torque efficiency θ_{FL} , respectively.

Chapter 8

In the Pd DL case, θ_{DL} increases with increasing the Pd thickness and peaks at 4Å then descends with further Pd thickness increase. The same behavior is observed for θ_{FL} but the peak position is at 5Å. In the reference FM sample, the value of θ_{DL} is 0.097, which is close to the reported value of the spin Hall angle in Co/Pt systems (~ 0.1) [73]. With the insertion of Pd DL, θ_{DL} increases over twice, while θ_{FL} increases over 8times. After examining the Damping-like effective field efficiency to Field-like effective field efficiency ratio (θ_{DL}/θ_{FL}), an apparent linear decrease is observed (Figure 8.6a). When the Pd DL is over 4Å thick, the Field-like torque exceeds the Damping-like torque, which is consistent with the pure Co/Pd case.

In the Rh case, a distinct behavior from the Pd case is observed. Once the Rh DL is introduced to the system, a decrease $\sim 40\%$ in θ_{DL} immediately occurs and remains constant with further increasing the Rh DL thickness. For θ_{FL} , an almost constant manner with a large decrease at 1Å and a slight increase at 4Å is observed. As for the Damping-like effective field efficiency to Field-like effective field efficiency ratio, θ_{DL}/θ_{FL} maintains its original value when the Rh DL is extremely thin (1Å) but immediately decreases to and stable at a smaller value with further increasing the Rh DL thickness (Figure 8.6b).

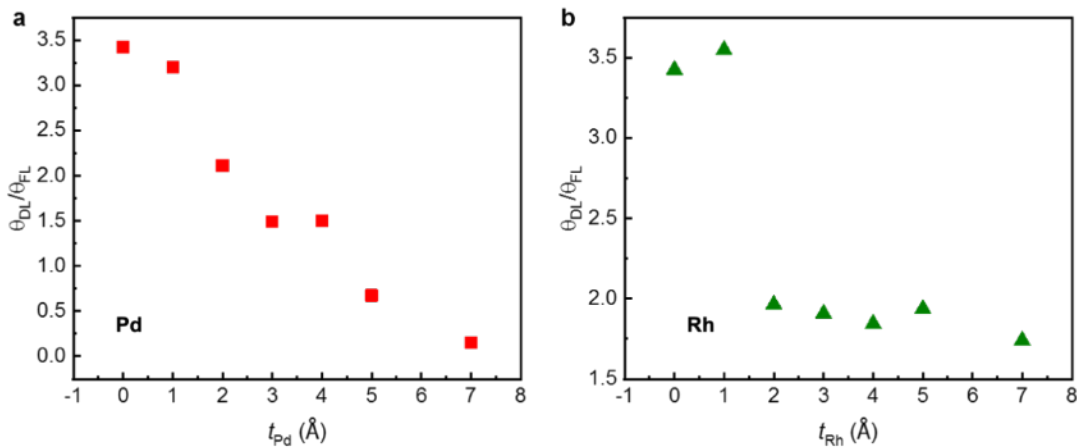


Figure 8-6: DL thickness dependence of calculated effective Damping-like to Field-like torque efficiency ratio. The Damping-like to Field-like torque efficiency ratio of Pd DL (a) and Rh DL (b) are plotted against the DL thickness.

Chapter 8

Even though both the Rh and Pd as $4d$ elements exhibit very similar behavior when served as DL, in this second harmonic Hall measurement, distinct thickness dependence of Damping-like and Field-like torques are observed. Such divergence could possibly be explained by the proximity induced moment as illustrated by the difference in saturation magnetization M_S of Pd DL and Rh DL in Chapter 5. The emergence of the sizeable Field-like torque and decreasing θ_{DL}/θ_{FL} ratio in both Pd and Rh cannot be explained solely by the spin Hall effect and interfacial transparency modification [108, 110]. Rashba effect, which induces the accumulation of spin current at the interface, might be a possible explanation for the enhanced Field-like torque.

In the 1-D model for SOT-driven DWM, the main contribution of the driving force comes from the Damping-like torque [17, 21, 59, 90, 91]. However, the thickness dependence of θ_{DL} obtained from the second Harmonic measurement does not agree well with the one determined from the 1-D model shown in Chapter 5. A plausible explanation will be the difference in the magnetization configuration. In the CIDWM case, there is a DW; in the second Harmonic measurement case, it is a single domain. Also, in the CIDWM case, the interfacial DMI constant plays a deterministic role for the DW configuration but is omitted here in the transport measurement. Besides, unlike in the second Harmonic measurement, where the magnetization is only slightly tilted from the out-of-plane direction, the DW magnetization is an in-plane configuration, which is also reported to cause a contrast difference for the SOT determination.

9. Conclusion

In order to bring racetrack memory based on CIDWM into real applications, higher velocities of DWM and lower threshold current densities, namely, faster response speed and lower energy consumption, are needed. In this thesis, instead of looking for materials with increased SOT and DMI as in more traditional research, the insertion of dusting layers between HM layers and FM layers was used. By this means of interfacial engineering, the CIDWM in both FM and SAF structures was significantly boosted with an enhancement of DW velocity by up to 350% and up to a 70% decrease of the threshold current. Such an increase in CIDWM efficiency is robust against varying temperature and device size.

By carefully selecting the DL materials and delicately varying the DLs thicknesses, the enhancement of CIDWM was shown to be a result of fine-tuning several spin-orbit coupling related magnetic parameters, including the effective magnetic uniaxial anisotropy energy (K_u^{eff}), the interfacial Dzyaloshinskii-Moriya interaction (D) and the spin-orbit torques (SOT). Apart from the increase in CIDWM efficiency, a linear relationship between the K_u^{eff} and D was shown for the first time and, most interestingly, groupings of D versus K_u^{eff} curves concerning two distinct families of DL types ($4d$ or $5d$ materials) was found. These results are, in turn, instructive for searching for materials with larger D and may further benefit research for novel magnetic structures, e.g., the formation of skyrmions and other non-collinear spin textures nano-objects.

A threshold spin current density was introduced, which is not included in the widely used 1-D analytical model of both SOT-driven DWM in the FM case and ECT-driven DWM in the SAF case. This threshold spin current density was then found to have a linear dependence on K_u^{eff} and, thus, can be very effectively manipulated by DL insertions. Reducing the threshold current density is a key to many applications of racetrack memory such as a replacement for very dense 3D memories.

The distinct differences between CIDWM in SOT-driven CIDWM in the FM case and ECT-driven CIDWM in the SAF case have been manifested in this thesis. The tight binding of K_u^{eff}

Chapter 9

and D makes faster terminal DW velocity and smaller threshold current density impractical in the SOT-driven CIDWM as once a more diminutive K_u^{eff} is realized for the reduction of J_{th} , the terminal DW velocity determined by D is also smaller. However, in the SAF case, there is no such dependence as the terminal velocity is now determined by the interlayer exchange coupling instead of D . Thus, a low J_{th} and faster terminal DW velocity can be realized at the same time with DL insertions. This is another key advantage of the SAF structure, in addition to, for example, its insensitivity to stray magnetic fields, lack of bending of the domain walls, and insensitivity of the DW velocity to curvature of the racetracks, that were previously reported. Our new findings demonstrate that SAF racetracks are the leading candidate for the realization of racetrack devices.

The interfacial nature of the mechanisms responsible for CIDWM has been further confirmed by preparing samples with co-sputtered Pd/Pt DLs and sandwiched Pt/Pd/Pt HM layers. Once the interface is dominated by the Co/Pd or Co/Pt, the CIDWM exhibits the corresponding behavior. All these results fit well to the D versus K_u^{eff} relationships and the threshold spin current density versus K_u^{eff} mentioned above concerning the type of interface that these samples possess.

Finally, transport measurement were used to determine the magnetic dependent scattering effects and spin-orbit torques in FM/DL/HM systems. The proximity induced moment is found to cause a big difference that results in different thickness dependences of damping-like and field-like torque efficiencies in the Pd and Rh DL cases. In the Pd DL case, for which there is a considerable proximity magnetic moment, both types of torques exhibit peak values for DL thicknesses of $\sim 4\text{-}5\text{\AA}$. In the Rh DL case, however, both damping-like and field-like torques show an almost non-varying dependence except for an initial large decrease. Interestingly, the discrepancy between the measured spin Hall angle from transport measurements and the calculated spin Hall angle from the CIDWM illustrates the importance of the magnetic configurations for the absorption of spin current within the magnetic layers.

In summary, interfacial engineering utilizing dusting layer insertions has been proved to be an effective method of enhancing the efficiency of CIDWM, which will help to speed-up the development of racetrack memory devices for real applications. In addition, interfacial engineering can also be used to manipulate interfacial magnetic parameters and thus examine

Chapter 9

the physical mechanisms at these interfaces. Apart from its impact in spintronics, the utilization of DLs in other interface-sensitive systems is likely to give rise to highly interesting physical phenomena.

Bibliography

1. Allwood, D.A., et al., *Magnetic domain-wall logic*. Science, 2005. **309**(5741): p. 1688-1692.
2. Torrejon, J., et al., *Neuromorphic computing with nanoscale spintronic oscillators*. Nature, 2017. **547**(7664): p. 428.
3. Parkin, S.S.P, and Yang, S.H., *Memory on the racetrack*. Nature Nanotechnology, 2015. **10**(3): p. 195-198.
4. Bader, S. and Parkin, S.S.P., *Spintronics*. Annual Review of Condensed Matter Physics, 2010. **1**(1): p. 71-88.
5. Zhou, X.L., et al., *Phase-Change Memory Materials by Design: A Strain Engineering Approach*. Advanced Materials, 2016. **28**(15): p. 3007-3016.
6. Kalikka, J., et al., *Strain-engineered diffusive atomic switching in two-dimensional crystals*. Nature Communications, 2016. **7**.
7. Parkin, S.S.P., Hayashi, M. & Thomas, L., *Magnetic Domain-Wall Racetrack Memory*. Science, 2008. **320**: p. 190-194.
8. Jiang, W., et al., *Blowing magnetic skyrmion bubbles*. Science, 2015. **349**(6245): p. 283-286.
9. Nayak, A.K., et al., *Magnetic antiskyrmions above room temperature in tetragonal Heusler materials*. Nature, 2017. **548**(7669): p. 561.
10. Fert, A., Cros, V., and Sampaio, J., *Skyrmions on the track*. Nature nanotechnology, 2013. **8**(3): p. 152-156.
11. Hayashi, M., et al., *Current-controlled magnetic domain-wall nanowire shift register*. Science, 2008. **320**(5873): p. 209-211.
12. Yang, S.H., Ryu, K.S., and Parkin, S.S.P., *Domain-wall velocities of up to 750 m s⁻¹ driven by exchange-coupling torque in synthetic antiferromagnets*. Nature Nanotechnology, 2015. **10**(3): p. 221-226.

13. Miron, I.M., et al., *Current-driven spin torque induced by the Rashba effect in a ferromagnetic metal layer*. Nature Materials, 2010. **9**(3): p. 230-234.
14. Thiaville, A., et al., *Micromagnetic understanding of current-driven domain wall motion in patterned nanowires*. EPL (Europhysics Letters), 2005. **69**(6): p. 990.
15. Manchon, A. and Zhang, S., *Theory of nonequilibrium intrinsic spin torque in a single nanomagnet*. Physical Review B, 2008. **78**(21): p. 212405.
16. Miron, I.M., et al., *Fast current-induced domain-wall motion controlled by the Rashba effect*. Nature Materials, 2011. **10**(6): p. 419-423.
17. Ryu, K.S., Thomas, L., Yang, S.H. & Parkin, S.S.P., *Chiral spin torque at magnetic domain walls*. Nature Nanotechnology, 2013. **8**(7): p. 527-533.
18. Bode, M., et al., *Chiral magnetic order at surfaces driven by inversion asymmetry*. Nature, 2007. **447**(7141): p. 190.
19. Dzyaloshinsky, I., *A thermodynamic theory of "weak" ferromagnetism of antiferromagnetics*. Journal of Physics and Chemistry of Solids, 1958. **4**(4): p. 241-255.
20. Moriya, T., *Anisotropic Superexchange Interaction and Weak Ferromagnetism*. Physical Review, 1960. **120**(1): p. 91-98.
21. Ryu, K.S., Yang, S.H., Thomas, L. and Parkin, S.S.P., *Chiral spin torque arising from proximity-induced magnetization*. Nature Communications, 2014. **5**: p. 3910.
22. Garg, C., et al., *Dramatic influence of curvature of nanowire on chiral domain wall velocity*. Science advances, 2017. **3**(5): p. e1602804.
23. Garg, C., et al., *Highly asymmetric chiral domain-wall velocities in Y-shaped junctions*. Nano letters, 2018. **18**(3): p. 1826-1830.
24. Blasing, R., et al., *Exchange coupling torque in ferrimagnetic Co/Gd bilayer maximized near angular momentum compensation temperature*. Nature Communications, 2018. **9**(1): p. 4984.
25. Kim, K.J., et al., *Fast domain wall motion in the vicinity of the angular momentum compensation temperature of ferrimagnets*. Nature Materials, 2017. **16**(12): p. 1187-1192.
26. Avci, C.O., et al., *Interface-driven chiral magnetism and current-driven domain walls in insulating magnetic garnets*. Nature Nanotechnology, 2019. **14**(6): p. 561-566.

27. Chen, G., Ma, T., N'Diaye, A. T., Kwon, H., Won, C., Wu, Y. and Schmid, A. K., *Tailoring the chirality of magnetic domain walls by interface engineering*. Nature Communications, 2013. **4**: p. 2671.
28. Soumyanarayanan, A., et al., *Emergent phenomena induced by spin-orbit coupling at surfaces and interfaces*. Nature, 2016. **539**(7630): p. 509.
29. Zhang, W., et al., *Role of transparency of platinum-ferromagnet interfaces in determining the intrinsic magnitude of the spin Hall effect*. Nature Physics, 2015. **11**(6): p. 496.
30. Torrejon, J., et al., *Interface control of the magnetic chirality in CoFeB/MgO heterostructures with heavy-metal underlayers*. Nature communications, 2014. **5**: p. 4655.
31. Cho, J., et al., *Thickness dependence of the interfacial Dzyaloshinskii-Moriya interaction in inversion symmetry broken systems*. Nature communications, 2015. **6**: p. 7635.
32. Kim, J., et al., *Layer thickness dependence of the current-induced effective field vector in Ta|CoFeB|MgO*. Nature materials, 2013. **12**(3): p. 240.
33. Parkin, S.S.P., *Origin of Enhanced Magnetoresistance of Magnetic Multilayers - Spin-Dependent Scattering from Magnetic Interface States*. Physical Review Letters, 1993. **71**(10): p. 1641-1644.
34. Kolesnikov, A.G., et al., *Nanoscale control of perpendicular magnetic anisotropy, coercive force and domain structure in ultrathin Ru/Co/W/Ru films*. Journal of Magnetism and Magnetic Materials, 2018. **454**: p. 78-84.
35. Parakkat, V.M., Ganesh, K.R., and Kumar, P.S.A., *Copper dusting effects on perpendicular magnetic anisotropy in Pt/Co/Pt tri-layers*. AIP Advances, 2016. **6**(5).
36. Almasi, H., et al., *Effect of Mo insertion layers on the magnetoresistance and perpendicular magnetic anisotropy in Ta/CoFeB/MgO junctions*. Applied Physics Letters, 2016. **109**(3).
37. Kaidatzis, A., et al., *Tailoring the magnetic anisotropy of CoFeB/MgO stacks onto W with a Ta buffer layer*. Applied Physics Letters, 2015. **106**(26).
38. Pai, C.F., et al., *Enhancement of perpendicular magnetic anisotropy and transmission of spin-Hall-effect-induced spin currents by a Hf spacer layer in W/Hf/CoFeB/MgO layer structures*. Applied Physics Letters, 2014. **104**(8).

39. Kittel, C., Gress, J.M., and Lessard, A., *Einführung in die Festkörperphysik*. Vol. 14. 1969: Oldenbourg München.
40. Kittel, C., McEuen, P., and McEuen, P., *Introduction to solid state physics*. Vol. 8. 1996: Wiley New York.
41. Stöhr, J. and Siegmann, H.C., *Magnetism*. Solid-State Sciences, Berlin, Heidelberg, 2006. **5**.
42. Néel, L., *Magnetism and local molecular field*. Science, 1971. **174**(4013): p. 985-992.
43. Chikazumi, S., *Physics of ferromagnetism*. New York: Oxford University Press) p, 2010, 251: 415.
44. Heisenberg, W., *Mehrkörperproblem und Resonanz in der Quantenmechanik*. Zeitschrift für Physik, 1926. **38**(6-7): p. 411-426.
45. Stoner, E.C., *Collective electron ferromagnetism II. Energy and specific heat*. Proceedings of the Royal Society of London. Series A. Mathematical and Physical Sciences, 1939. **169**(938): p. 339-371.
46. Ruderman, M.A. and Kittel, C., *Indirect exchange coupling of nuclear magnetic moments by conduction electrons*. Physical Review, 1954. **96**(1): p. 99.
47. Kasuya, T.J., *A theory of metallic ferro-and antiferromagnetism on Zener's model*. Progress of theoretical physics, 1956. **16**(1): p. 45-57.
48. Yosida, K.J., *Magnetic properties of Cu-Mn alloys*. Physical Review, 1957. **106**(5): p. 893.
49. Parkin, S.S.P., and Mauri, D., *Spin engineering: Direct determination of the Ruderman-Kittel-Kasuya-Yosida far-field range function in ruthenium*. Physical Review B, 1991. **44**(13): p. 7131.
50. Bloemen, P., et al., *Oscillatory interlayer exchange coupling in Co/Ru multilayers and bilayers*. Physical Review B, 1994. **50**(18): p. 13505.
51. Gradmann, U., *Magnetic surface anisotropies*. Journal of Magnetism and Magnetic Materials, 1986. **54**: p. 733-736.
52. Draaisma, H., et al., *Magnetic interface anisotropy in Pd/Co and Pd/Fe multilayers*. Journal of Magnetism and Magnetic Materials, 1987. **66**(3): p. 351-355.

53. Luttinger, J. and Kittel, C., *A note on the quantum theory of ferromagnetic resonance*. *Helv. Phys. Acta*, 1948. **21**(6): p. 480-489.
54. Koopmans, B., et al., *Unifying ultrafast magnetization dynamics*. *Physical Review Letters*, 2005. **95**(26): p. 267207.
55. Landau, L. and Lifshitz, E., *Phys. Z Sowjetunion* 8, 153 (1953); *TL Gilbert*. *Physical Review*, 1955. **100**: p. 1243.
56. Schryer, N.L. and Walker, L.R., *The motion of 180 domain walls in uniform dc magnetic fields*. *Journal of Applied Physics*, 1974. **45**(12): p. 5406-5421.
57. Metaxas, P.J., et al., *Creep and flow regimes of magnetic domain-wall motion in ultrathin Pt/Co/Pt films with perpendicular anisotropy*. *Physical Review Letters*, 2007. **99**(21): p. 217208.
58. Beach, G.S., et al., *Dynamics of field-driven domain-wall propagation in ferromagnetic nanowires*. *Nature Materials*, 2005. **4**(10): p. 741-744.
59. Thiaville, A., et al., *Dynamics of Dzyaloshinskii domain walls in ultrathin magnetic films*. *EPL (Europhysics Letters)*, 2012. **100**(5): p. 57002.
60. Pham, T.H., et al., *Very large domain wall velocities in Pt/Co/GdOx and Pt/Co/Gd trilayers with Dzyaloshinskii-Moriya interaction*. *EPL (Europhysics Letters)*, 2016. **113**(6).
61. Brataas, A., Kent, A.D., and Ohno, H., *Current-induced torques in magnetic materials*. *Nature Materials*, 2012. **11**(5): p. 372-381.
62. Ralph, D.C., Stiles, M.D., *Spin transfer torques*. *Journal of Magnetism and Magnetic Materials*, 2008. **320**(7): p. 1190-1216.
63. Zhang, S. and Li, Z., *Roles of nonequilibrium conduction electrons on the magnetization dynamics of ferromagnets*. *Physical Review Letters*, 2004. **93**(12): p. 127204.
64. Zhang, S., Levy, P., and Fert, A., *Mechanisms of spin-polarized current-driven magnetization switching*. *Physical Review Letters*, 2002. **88**(23): p. 236601.
65. Slonczewski, J.C., *Current-driven excitation of magnetic multilayers*. *Journal of Magnetism and Magnetic Materials*, 1996. **159**(1): p. L1-L7.
66. Manchon, A. and Zhang, S., *Theory of nonequilibrium intrinsic spin torque in a single nanomagnet*. *Physical Review B*, 2008. **78**(21): p. 212405.

67. Li, Z. and Zhang, S., *Magnetization dynamics with a spin-transfer torque*. Physical Review B, 2003. **68**(2): p. 024404.
68. Tatara, G. and Kohno, H., *Microscopic theory of current-driven domain wall motion*. Journal of Electron Microscopy, 2005. **54**: p. I69-I74.
69. Tatara, G. and Kohno, H., *Theory of current-driven domain wall motion: Spin transfer versus momentum transfer*. Physical Review Letters, 2004. **92**(8): p. 086601.
70. Waintal, X. and Viret, M., *Current-induced distortion of a magnetic domain wall*. EPL (Europhysics Letters), 2004. **65**(3): p. 427.
71. Koyama, T., et al., *Observation of the intrinsic pinning of a magnetic domain wall in a ferromagnetic nanowire*. Nature Materials, 2011. **10**(3): p. 194-197.
72. Seung-heon, C. Baek, et al., *Spin currents and spin-orbit torques in ferromagnetic trilayers*. Nature Materials, 2018. **17**(6): p. 509-513.
73. Sinova, J., et al., *Spin Hall effects*. Reviews of Modern Physics, 2015. **87**(4): p. 1213-1259.
74. Emori, S., Bauer, U., Ahn, S. M., Martinez, E. & Beach, G. S., *Current-driven dynamics of chiral ferromagnetic domain walls*. Nature Materials, 2013. **12**(7): p. 611-616.
75. Liu, L., Lee, O. J., Gudmundsen, T. J., Ralph, D. C. & Buhrman, R. A., *Current-induced switching of perpendicularly magnetized magnetic layers using spin torque from the spin Hall effect*. Physical Review Letters, 2012. **109**(9): p. 096602.
76. Brataas, A., Kent, A.D., and Ohno, H., *Current-induced torques in magnetic materials*. Nature Materials, 2012. **11**(5): p. 372-381.
77. Miron, I.M., et al., *Perpendicular switching of a single ferromagnetic layer induced by in-plane current injection*. Nature, 2011. **476**(7359): p. 189-193.
78. Miron, I.M., et al., *Current-driven spin torque induced by the Rashba effect in a ferromagnetic metal layer*. Nature Materials, 2010. **9**(3): p. 230-234.
79. Ganichev, S., et al., *Spin-galvanic effect*. Nature, 2002. **417**(6885): p. 153-156.
80. Garate, I. and Franz, M., *Inverse spin-galvanic effect in the interface between a topological insulator and a ferromagnet*. Physical Review Letters, 2010. **104**(14): p. 146802.

81. Inoue, J., Bauer, G.E.W., and Molenkamp, L.W., *Diffuse transport and spin accumulation in a Rashba two-dimensional electron gas*. Physical Review B, 2003. **67**(3): p. 033104.
82. Hirsch, J., *Spin hall effect*. Physical Review Letters, 1999. **83**(9): p. 1834.
83. Sinova, J., et al., *Universal intrinsic spin Hall effect*. Physical Review Letters, 2004. **92**(12): p. 126603.
84. Nagaosa, N., et al., *Anomalous hall effect*. Review of Modern Physics, 2010. **82**(2): p. 1539.
85. Berry, M.V., *Quantal phase factors accompanying adiabatic changes*. Proceedings of the Royal Society of London. A. Mathematical and Physical Sciences, 1984. **392**(1802): p. 45-57.
86. Saitoh, E., et al., *Conversion of spin current into charge current at room temperature: Inverse spin-Hall effect*. Applied Physics Letters, 2006. **88**(18): p. 182509.
87. Kimura, T., et al., *Room-temperature reversible spin Hall effect*. Physical Review Letters, 2007. **98**(15): p. 156601.
88. Nagaosa, N., et al., *Anomalous Hall effect*. Reviews of Modern Physics, 2010. **82**(2): p. 1539-1592.
89. Koyama, T., et al., *Current-induced magnetic domain wall motion below intrinsic threshold triggered by Walker breakdown*. Nature Nanotechnology, 2012. **7**(10): p. 635-639.
90. Martinez, E., Emori, S. and Beach, G.S., *Current-driven domain wall motion along high perpendicular anisotropy multilayers: The role of the Rashba field, the spin Hall effect, and the Dzyaloshinskii-Moriya interaction*. Applied Physics Letters, 2013. **103**(7): p. 072406.
91. Khvalkovskiy, A.V., et al., *Matching domain-wall configuration and spin-orbit torques for efficient domain-wall motion*. Physical Review B, 2013. **87**(2): p. 020402.
92. Baltz, V., et al., *Antiferromagnetic spintronics*. Reviews of Modern Physics, 2018. **90**(1).
93. Yang, S.H. and Parkin, S.S.P., *Novel domain wall dynamics in synthetic antiferromagnets*. Journal of Physics Condensed Matters, 2017. **29**(30): p. 303001.
94. Žutić, I., et al., *Proximitized materials*. Materials Today, 2018.

95. Obinata, A., et al., *Electric-field control of magnetic moment in Pd*. Scientific Reports, 2015. **5**: p. 14303.
96. Sakuragi, S., et al., *Thickness-dependent appearance of ferromagnetism in Pd(100) ultrathin films*. Physical Review B, 2014. **90**(5): p. 054411.
97. Kim, S., et al., *Correlation of the Dzyaloshinskii-Moriya interaction with Heisenberg exchange and orbital asphericity*. Nature Communications, 2018. **9**(1): 1-9.
98. Ma, X., et al., *Interfacial Dzyaloshinskii-Moriya Interaction: Effect of 5d Band Filling and Correlation with Spin Mixing Conductance*. Physical Review Letters, 2018. **120**(15): p. 157204.
99. Suzuki, M., et al., *Depth profile of spin and orbital magnetic moments in a subnanometer Pt film on Co*. Physical Review B, 2005. **72**(5): p. 054430.
100. Onoda, S., Sugimoto, N., and Nagaosa, N., *Quantum transport theory of anomalous electric, thermoelectric, and thermal Hall effects in ferromagnets*. Physical Review B, 2008. **77**(16): p. 165103.
101. Tian, Y., Ye, L., and Jin, X., *Proper scaling of the anomalous Hall effect*. Physical Review Letters, 2009. **103**(8): p. 087206.
102. Velev, J., et al., *Ballistic anisotropic magnetoresistance*. Physical Review Letters, 2005. **94**(12): p. 127203.
103. Tang, H., et al., *Giant planar Hall effect in epitaxial (Ga, Mn) As devices*. Physical Review Letters, 2003. **90**(10): p. 107201.
104. Garello, K., et al., *Symmetry and magnitude of spin-orbit torques in ferromagnetic heterostructures*. Nature Nanotechnology, 2013. **8**(8): p. 587-593.
105. Hayashi, M., et al., *Quantitative characterization of the spin-orbit torque using harmonic Hall voltage measurements*. Physical Review B, 2014. **89**(14): p. 144425.
106. Avci, C.O., et al., *Unidirectional spin Hall magnetoresistance in ferromagnet/normal metal bilayers*. Nature Physics, 2015. **11**(7): p. 570-575.
107. Kim, J., et al., *Layer thickness dependence of the current-induced effective field vector in Ta|CoFeB|MgO*. Nature Materials, 2013. **12**(3): p. 240-245.
108. Pai, C.-F., et al., *Dependence of the efficiency of spin Hall torque on the transparency of Pt/ferromagnetic layer interfaces*. Physical Review B, 2015. **92**(6): p. 064426.

109. Nguyen, M.H., Ralph, D., and Buhrman, R., *Spin torque study of the spin Hall conductivity and spin diffusion length in platinum thin films with varying resistivity*. Physical Review Letters, 2016. **116**(12): p. 126601.
110. Zhang, W., et al., *Role of transparency of platinum–ferromagnet interfaces in determining the intrinsic magnitude of the spin Hall effect*. Nature Physics, 2015. **11**(6): p. 496-502.

Appendix

A: Macro-magnetic derivation of second harmonic Hall signal for determination of effective fields

In a typical magnetic thin film with perpendicular magnetic anisotropy, the magnetic energy of the system can be written as:

$$E = -K_u^{\text{eff}} \cos^2 \theta - \vec{M} \cdot \vec{H}$$

Where $\vec{M} = M_S \vec{m} = M_S (\cos \varphi \sin \theta, \sin \varphi \sin \theta, \cos \theta)$ with φ and θ are its azimuthal angle, and $\vec{H} = H^{\text{eff}} (\cos \varphi_H \sin \theta_H, \sin \varphi_H \sin \theta_H, \cos \theta_H)$ with φ_H and θ_H also the azimuthal angle of the effective exterior field.

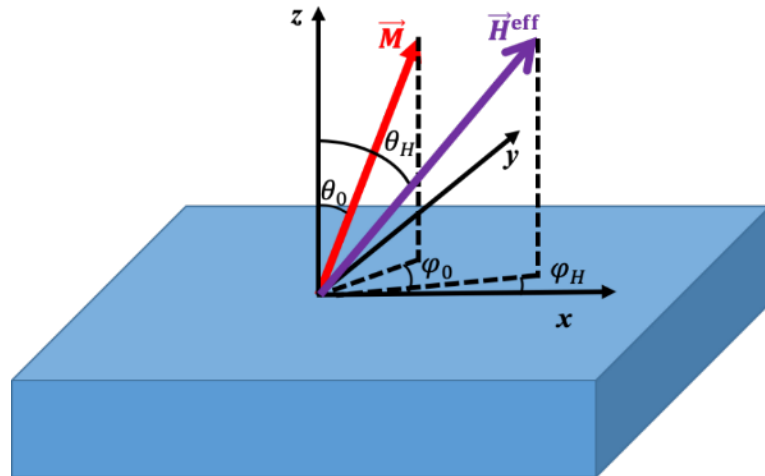


Figure A-1: Schematic illustration of a magnetic film with PMA under the application of the exterior magnetic field.

Appendix

The following equation set then determines the equilibrium azimuthal angle of magnetization (φ_0, θ_0):

$$\begin{cases} \frac{\partial E}{\partial \theta} = 0 = K_u^{\text{eff}} \sin 2\theta_0 - M_S H^{\text{eff}} [\cos \theta_0 \sin \theta_H (\cos \varphi_0 \cos \varphi_H + \sin \varphi_0 \sin \varphi_H) - \sin \theta_0 \cos \theta_H] \\ \frac{\partial E}{\partial \varphi} = 0 = M_S H^{\text{eff}} \sin \theta_0 \sin \theta_H \sin (\varphi_H - \varphi_0) \end{cases}$$

Considering when the current is injected into the system, and the SOT is generated, the magnetization angle will deviate from the equilibrium position (φ_0, θ_0) as ($\Delta\varphi, \Delta\theta$). It can be written in the following form:

$$\begin{cases} \Delta\theta = \sum_i \frac{\partial \theta}{\partial H_i} \Delta H_i \\ \Delta\varphi = \sum_i \frac{\partial \varphi}{\partial H_i} \Delta H_i \end{cases}$$

Here, i denotes the x, y, z directions and ΔH_i is the SOT-effective field in i -direction. The degree of changes $\frac{\partial \varphi}{\partial H_i}$ and $\frac{\partial \theta}{\partial H_i}$ by applying the ΔH_i can be solved by using the above equation sets:

$$\begin{aligned} \frac{\partial}{\partial H_i} \left(\frac{\partial E}{\partial \theta} \right) = 0 &= [2K_u^{\text{eff}} \cos 2\theta_0 - M_S (-H_x \cos \varphi_0 \sin \theta_0 - H_y \sin \varphi_0 \sin \theta_0 - H_z \cos \theta_0)] \frac{\partial \theta}{\partial H_i} \\ &+ M_S (H_x \sin \varphi_0 - H_y \cos \varphi_0) \frac{\partial \varphi}{\partial H_i} - M_S f_i \\ \frac{\partial}{\partial H_i} \left(\frac{\partial E}{\partial \varphi} \right) = 0 &= M_S [H_x \sin \varphi_0 - H_y \cos \varphi_0] \frac{\partial \theta}{\partial H_i} + M_S \sin \theta_0 [H_x \cos \varphi_0 + H_y \sin \varphi_0] \frac{\partial \varphi}{\partial H_i} \\ &+ M_S g_i \end{aligned}$$

Where

$$\begin{aligned} \vec{f} &= (\cos \varphi_0 \cos \theta_0, \sin \varphi_0 \cos \theta_0, \sin \theta_0) \\ \vec{g} &= (\sin \theta_0 \sin \varphi_0, -\sin \theta_0 \cos \varphi_0, 0) \end{aligned}$$

Appendix

Since the exterior field is applied along the x or y -axis as in the second-harmonic Hall measurement, both $\varphi_H = \varphi_0$ and $\sin 2\varphi_0 = 0$ are determined. By solving the above equation sets, the deviation angle ($\Delta\varphi$, $\Delta\theta$) are solved as follows:

$$\Delta\theta = M_S \frac{\cos\theta_0(\Delta H_x \cos\varphi_H + \Delta H_y \sin\varphi_H) - \sin\theta_0 \Delta H_z}{2K_u^{\text{eff}} \cos 2\theta_0 + H^{\text{eff}} \cos(\theta_H - \theta_0)}$$

$$\Delta\varphi = \frac{-\Delta H_x \sin\varphi_H + \Delta H_y \cos\varphi_H}{H^{\text{eff}} \sin\theta_H}$$

As in the Hall measurement, the transverse Hall resistance has the following form with the contributions from both the anomalous Hall effect and planar Hall effect:

$$R_{xy} = \frac{1}{2} R_{\text{ahe}} \cos\theta + \frac{1}{2} R_{\text{phe}} \sin^2\theta \sin 2\varphi$$

Substituting (φ, θ) with $(\varphi_0 + \Delta\varphi, \theta_0 + \Delta\theta)$, and applying $\Delta\varphi(\theta) \ll 1$, the above equation can be expanded to the following form:

$$R_{xy} = \frac{1}{2} R_{\text{ahe}} (\cos\theta_0 - \Delta\theta \sin\theta_0) + \frac{1}{2} R_{\text{phe}} (\sin^2\theta_0 + \Delta\theta \sin 2\theta_0) (\sin 2\varphi_0 + 2\Delta\varphi \cos 2\varphi_0)$$

Since the AC of a sine waveform ($I = I_0 \sin\omega t$) is used, so the effective fields from this sinusoidal current are also oscillating as $\Delta H_i = \Delta H_i \sin\omega t$ and respectively, the angle deviation should also be replaced as $\Delta\varphi \sin\omega t$ and $\Delta\theta \sin\omega t$ in the above expression of R_{xy} . The anomalous Hall voltage measured in the experiment as $V_{xy} = R_{xy} I$ has the following form:

$$V_{xy} = V_0 + V_\omega \sin\omega t + V_{2\omega} \cos 2\omega t$$

$$V_0 = \frac{1}{2} (B_\theta + B_\varphi) I_0$$

$$V_\omega = A I_0$$

Appendix

$$V_{2\omega} = -\frac{1}{2}(B_\theta + B_\varphi)I_0$$

Here,

$$A = \frac{1}{2}R_{\text{ahe}}\cos\theta_0 + \frac{1}{2}R_{\text{phe}}\sin^2\theta_0\sin 2\varphi_0$$

$$B_\theta = -\Delta\theta\left(\frac{1}{2}R_{\text{ahe}}\sin\theta_0 - \frac{1}{2}R_{\text{phe}}\sin 2\theta_0\sin 2\varphi_0\right)$$

$$B_\varphi = \Delta\varphi R_{\text{phe}}\sin^2\theta_0\cos 2\varphi_0$$

If taking the assumption as both \vec{H}^{eff} and ΔH_i are small, so the magnetization is not so deviated from the magnetic easy axis along the z -direction, which means $\theta_0 \ll 1$. Thus,

$$\theta_0 = \frac{H^{\text{eff}}\sin\theta_H}{H_K^{\text{eff}} \pm H^{\text{eff}}\cos\theta_H}$$

Here, + and – correspond to magnetization in z -direction and $-z$ -direction, H_K^{eff} is the effective uniaxial anisotropy field defined as $2K_u^{\text{eff}}/M_S$. Substituting the above θ_0 term into the expression of harmonic Hall voltage signal, and taking $\varphi_0 = \varphi_H$, the first and second harmonic Hall voltages are written as:

$$V_\omega \approx \pm \frac{1}{2}R_{\text{ahe}}\left[1 - \frac{1}{2}\left(\frac{H^{\text{eff}}\sin\theta_H}{H_K^{\text{eff}} \pm H^{\text{eff}}\cos\theta_H}\right)^2\right]I_0$$

$$V_{2\omega} \approx -\frac{1}{4}[\mp R_{\text{ahe}}(\Delta H_x\cos\varphi_H + \Delta H_y\sin\varphi_H)$$

$$+ 2R_{\text{phe}}(-\Delta H_x\sin\varphi_H + \Delta H_y\cos\varphi_H)\cos 2\varphi_H] \times \frac{H^{\text{eff}}\sin\theta_H I_0}{(H_K^{\text{eff}} \pm H^{\text{eff}}\cos\theta_H)^2}$$

By the above derivation, the first and second harmonic Hall voltages have the mixed contributions from anomalous Hall effect and planar Hall effect. As the effective exterior field is swept in the x and y direction, $\theta_H = \frac{\pi}{2}$ could be inserted into the above equation set and further leads to:

Appendix

$$\begin{aligned}
 V_\omega &\approx \pm \frac{1}{2} R_{\text{ahe}} \left[1 - \frac{1}{2} \left(\frac{H^{\text{eff}}}{H_K^{\text{eff}}} \right)^2 \right] I_0 \\
 V_{2\omega} &\approx -\frac{1}{4} [\mp R_{\text{ahe}} (\Delta H_x \cos \varphi_H + \Delta H_y \sin \varphi_H) \\
 &\quad + 2R_{\text{phe}} (-\Delta H_x \sin \varphi_H + \Delta H_y \cos \varphi_H) \cos 2\varphi_H] \times \frac{H^{\text{eff}} I_0}{(H_K^{\text{eff}})^2}
 \end{aligned}$$

For the exterior field along the x -axis, the equation set becomes:

$$\begin{aligned}
 V_\omega &\approx \pm \frac{1}{2} R_{\text{ahe}} \left[1 - \frac{1}{2} \left(\frac{H^{\text{eff}}}{H_K^{\text{eff}}} \right)^2 \right] I_0 \\
 V_{2\omega} &\approx -\frac{1}{4} [\mp R_{\text{ahe}} \Delta H_x + 2R_{\text{phe}} \Delta H_y] \times \frac{H^{\text{eff}} I_0}{(H_K^{\text{eff}})^2}
 \end{aligned}$$

And for the exterior field along the y -axis, the equation set becomes:

$$\begin{aligned}
 V_\omega &\approx \pm \frac{1}{2} R_{\text{ahe}} \left[1 - \frac{1}{2} \left(\frac{H^{\text{eff}}}{H_K^{\text{eff}}} \right)^2 \right] I_0 \\
 V_{2\omega} &\approx -\frac{1}{4} [\mp R_{\text{ahe}} \Delta H_y + 2R_{\text{phe}} \Delta H_x] \times \frac{H^{\text{eff}} I_0}{(H_K^{\text{eff}})^2}
 \end{aligned}$$

The effective longitudinal field ΔH_x and effective transverse field ΔH_y has the following form:

$$\Delta H_{x(y)} = \frac{H_{L(T)} \pm 2\chi H_{T(L)}}{1 - \chi^2}$$

Where

$$H_{L(T)} = -2 \frac{\partial V_{2\omega} / \partial H^{\text{eff}}}{\partial^2 V_\omega / \partial H^{\text{eff}2}} \Big|_{\vec{H}^{\text{eff}} \parallel \vec{x}(\vec{y})}$$

Appendix

And

$$\chi = R_{\text{phe}}/R_{\text{ahe}}$$

From the above derivation, it is worth noticing as these assumptions are used: First, the exterior magnetic field applied to the system should be in the in-plane direction and much smaller than the effective uniaxial anisotropy field to satisfy $\theta_0 \ll 1$; second, it will be essential to determine the planar Hall resistance to anomalous Hall resistance ratio, since both signals will contribute to the harmonic Hall voltage.

B: Supplementary figures

B.1. Film characterizations with AFM and XRD

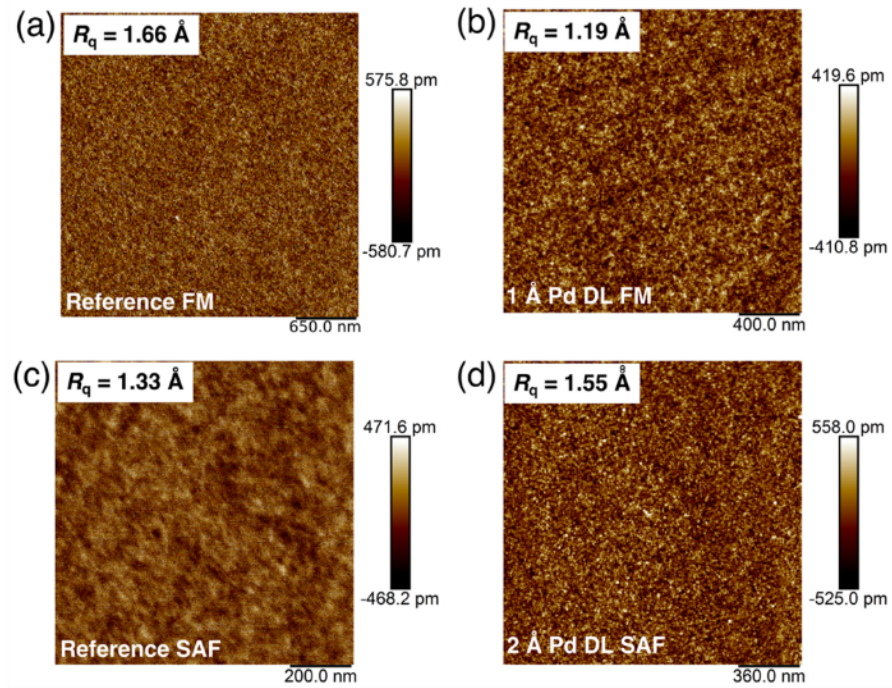


Figure B-1: AFM topographic images of typical films with and without interfacial DLs. a, reference FM film without a DL: 20 TaN|15 Pt|3 Co|7 Ni|1.5 Co|8.5 Ru|50 TaN; b, FM film with a 1 Å thick Pd DL: 20 TaN|15 Pt|1 Pd|3 Co|7 Ni|1.5 Co|8.5 Ru|50 TaN; c, Reference SAF film: 20 TaN|15 Pt|3 Co|7 Ni|1.5 Co|8.5 Ru|5 Co|7 Ni|1.5 Co|50 TaN; d, SAF film with a 2 Å thick Pd DL: 20 TaN|15 Pt|2 Pd|3 Co|7 Ni|1.5 Co|8.5 Ru|5 Co|7 Ni|1.5 Co|50 TaN. All thicknesses are given in angstroms. The root mean square roughness R_q of each of the films is given in the image.

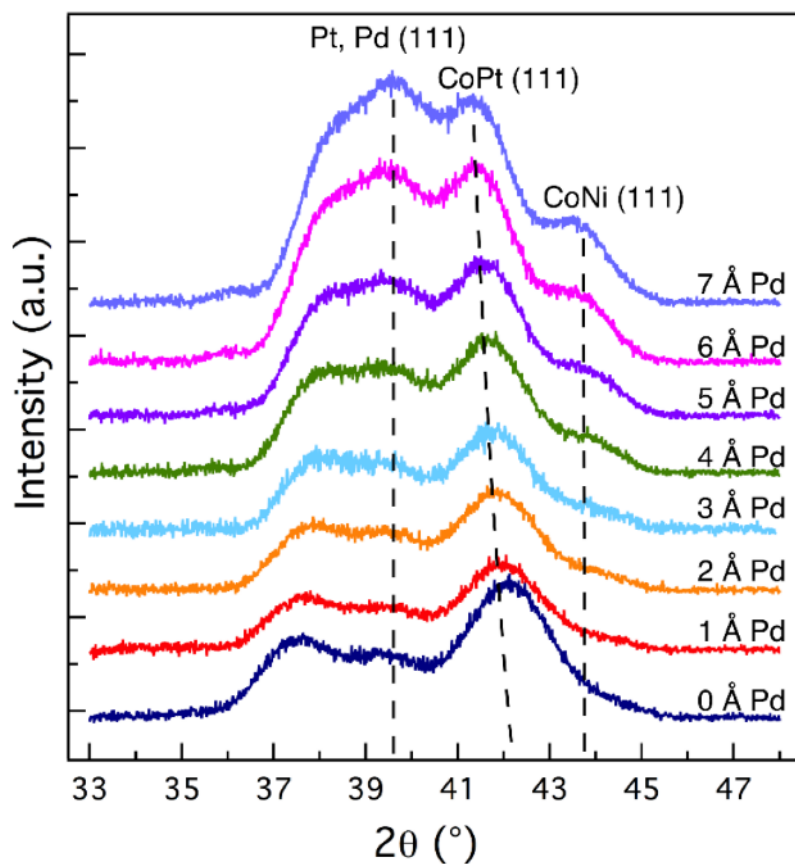


Figure B-2: The x-ray diffraction (XRD) patterns of the SAF structures with Pd dusting layer insertions. The DL thickness increases from 0 to 7 Å as indicated in the figure.

B.2. Fitting for the longitudinal field dependence of DW velocity in SAF structure using a 1-D analytical model

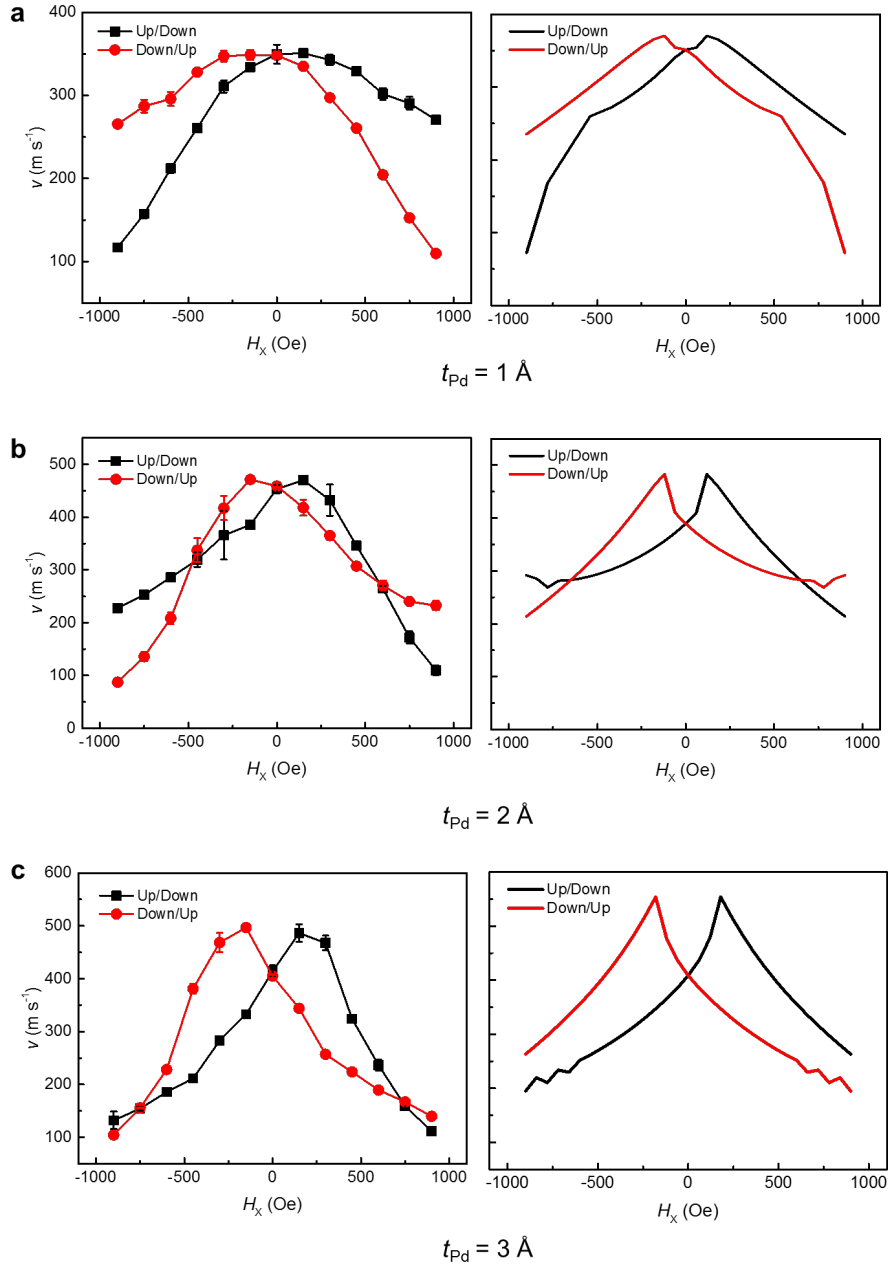


Figure B-3: Fitting results of CIDWM in SAF. Experimental results of the longitudinal field dependence of the DW velocity in the Pd DL system (left panel) and the corresponding simulations (right panel) based on the 1-D model with DL thicknesses of: 1 Å (a), 2 Å (b) and 3 Å (c).

Appendix

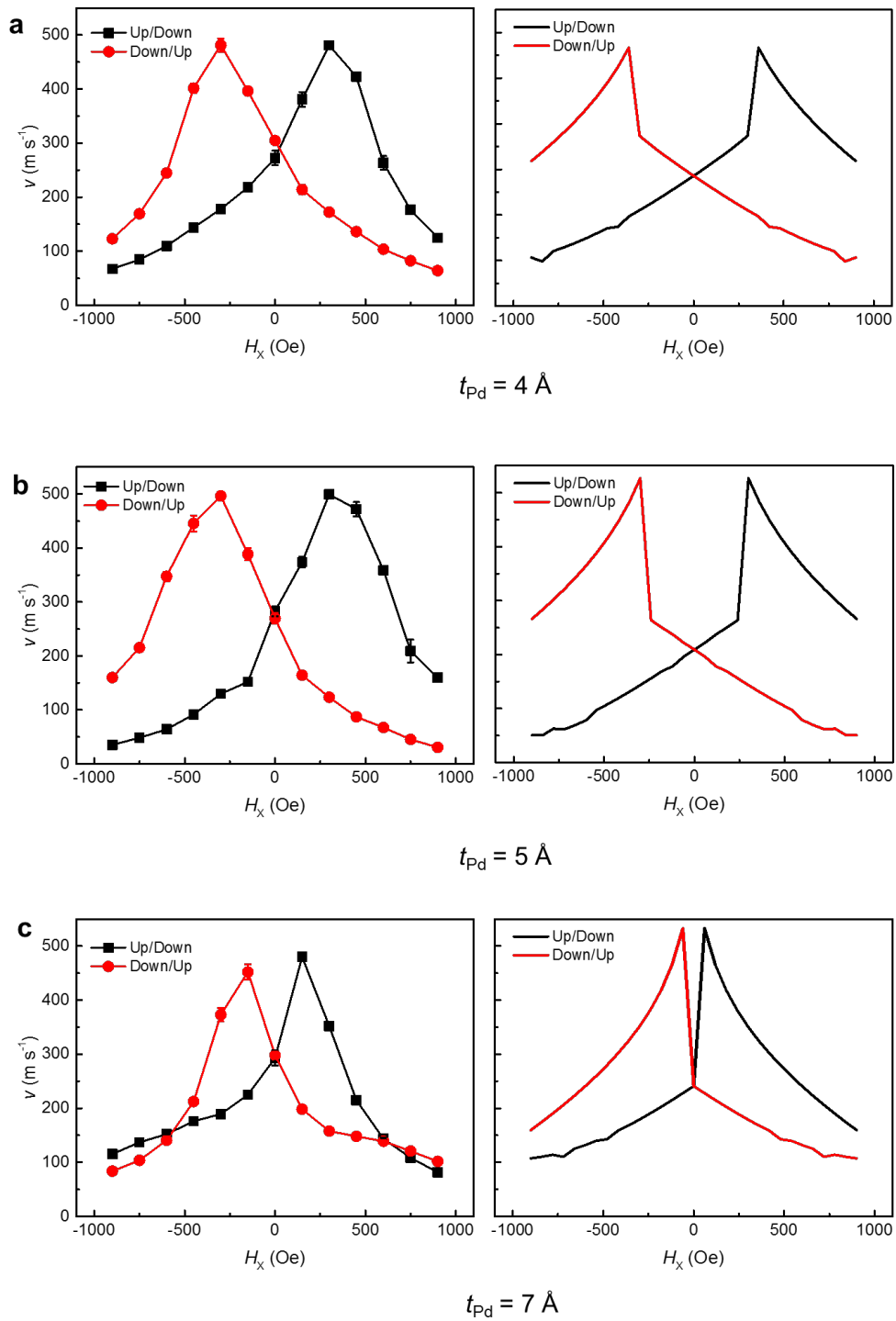


Figure B-4: Fitting results of CIDWM in SAF. Experimental results of the longitudinal field dependence of the DW velocity in the Pd DL system (left panel) and the corresponding simulations (right panel) based on the 1-D model with DL thicknesses of: 4 Å (a), 5 Å (b) and 7 Å (c).

Appendix

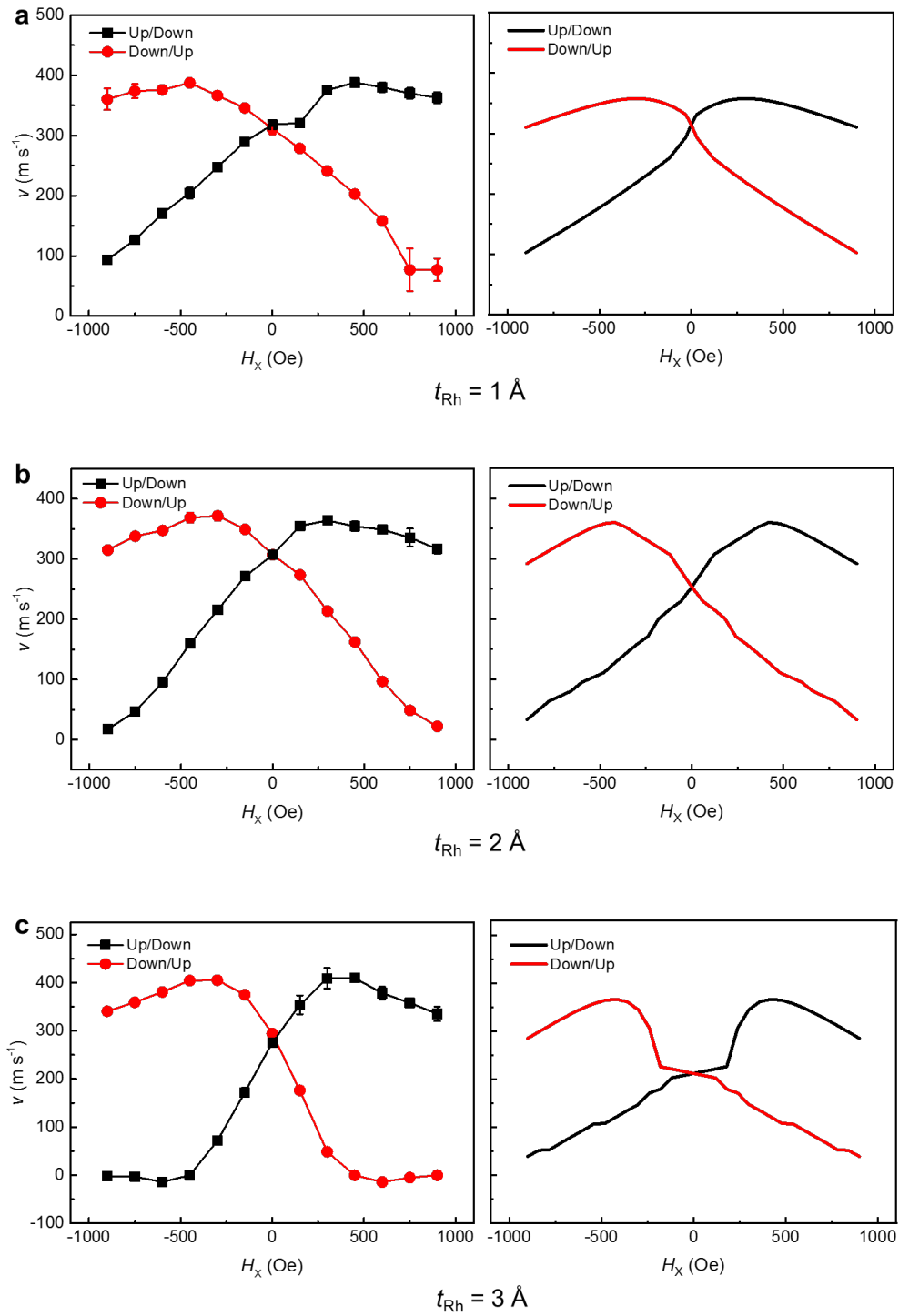


Figure B-5: Fitting results of CIDWM in SAF. Experimental results of the longitudinal field dependence of the DW velocity in the Rh DL system (left panel) and the corresponding simulations (right panel) based on the 1-D model with DL thicknesses of: 1 Å (a), 2 Å (b) and 3 Å (c).

Appendix

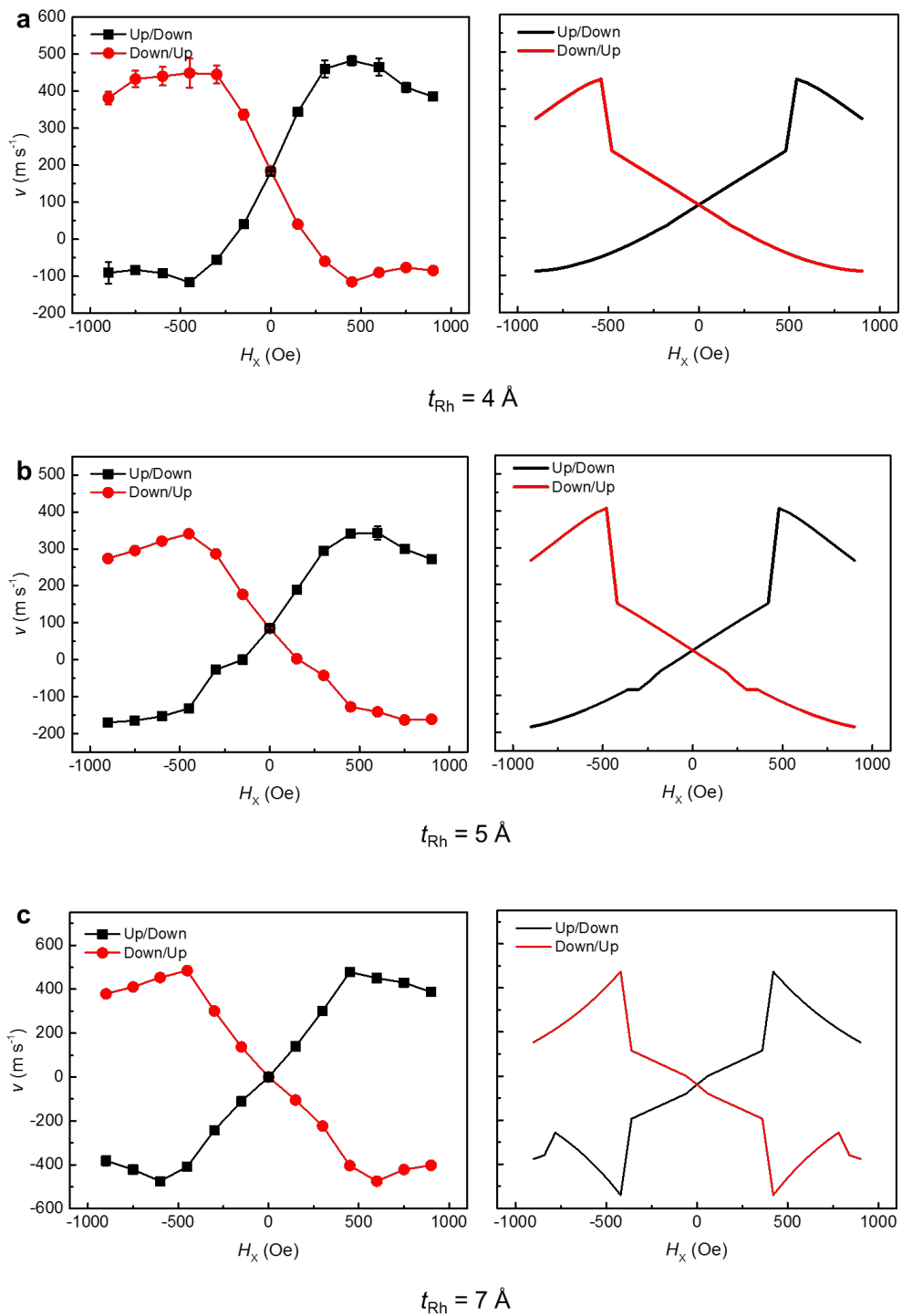


Figure B-6: Fitting results of CIDWM in SAF. Experimental results of the longitudinal field dependence of the DW velocity in the Rh DL system (left panel) and the corresponding simulations (right panel) based on the 1-D model with DL thicknesses of: 4 Å (a), 5 Å (b) and 7 Å (c).

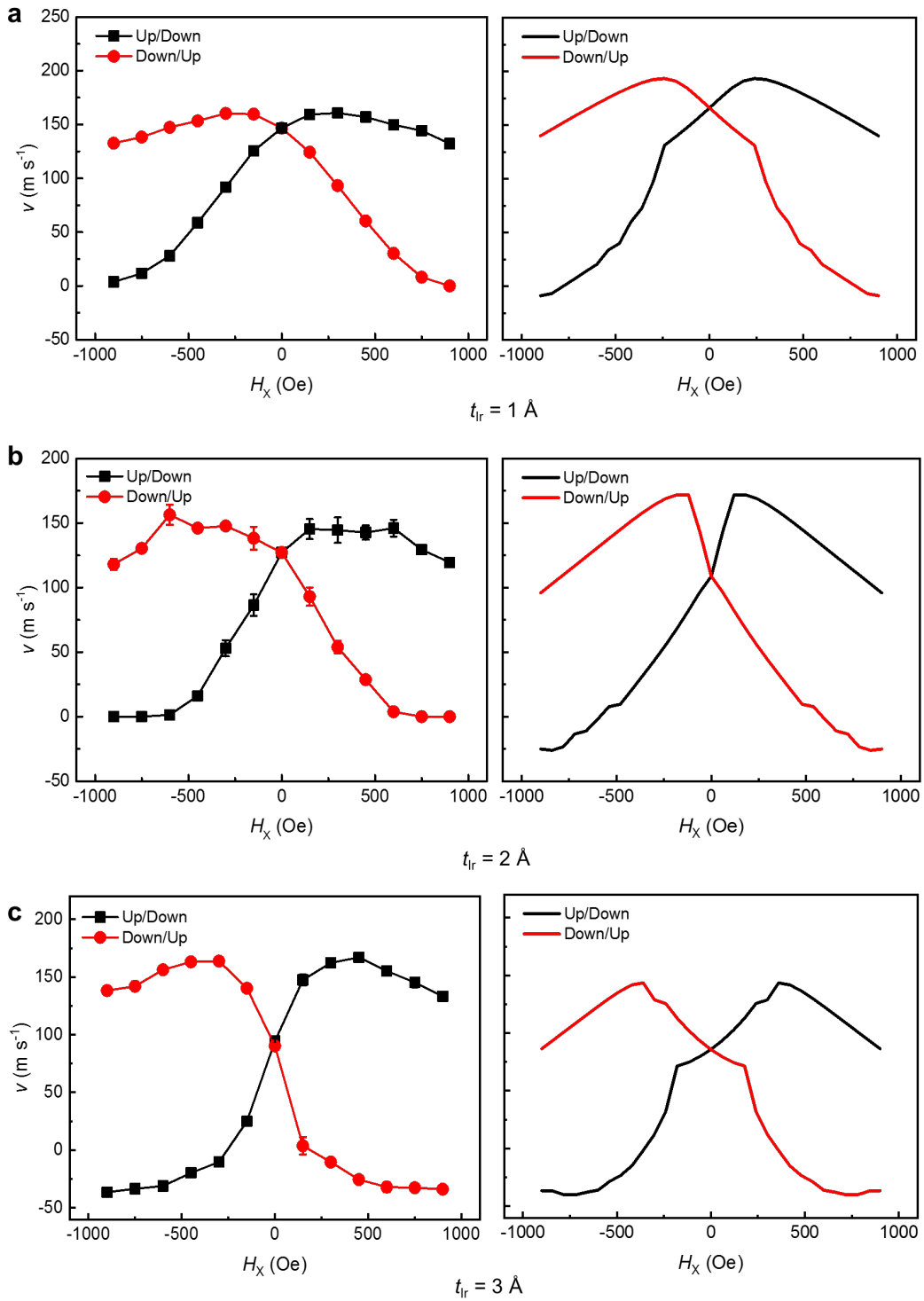


Figure B-7: Fitting results of CIDWM in SAF. Experimental results of the longitudinal field dependence of the DW velocity in the Ir DL system (left panel) and the corresponding simulations (right panel) based on the 1-D model with DL thicknesses of: 1 Å (a), 2 Å (b) and 3 Å (c).

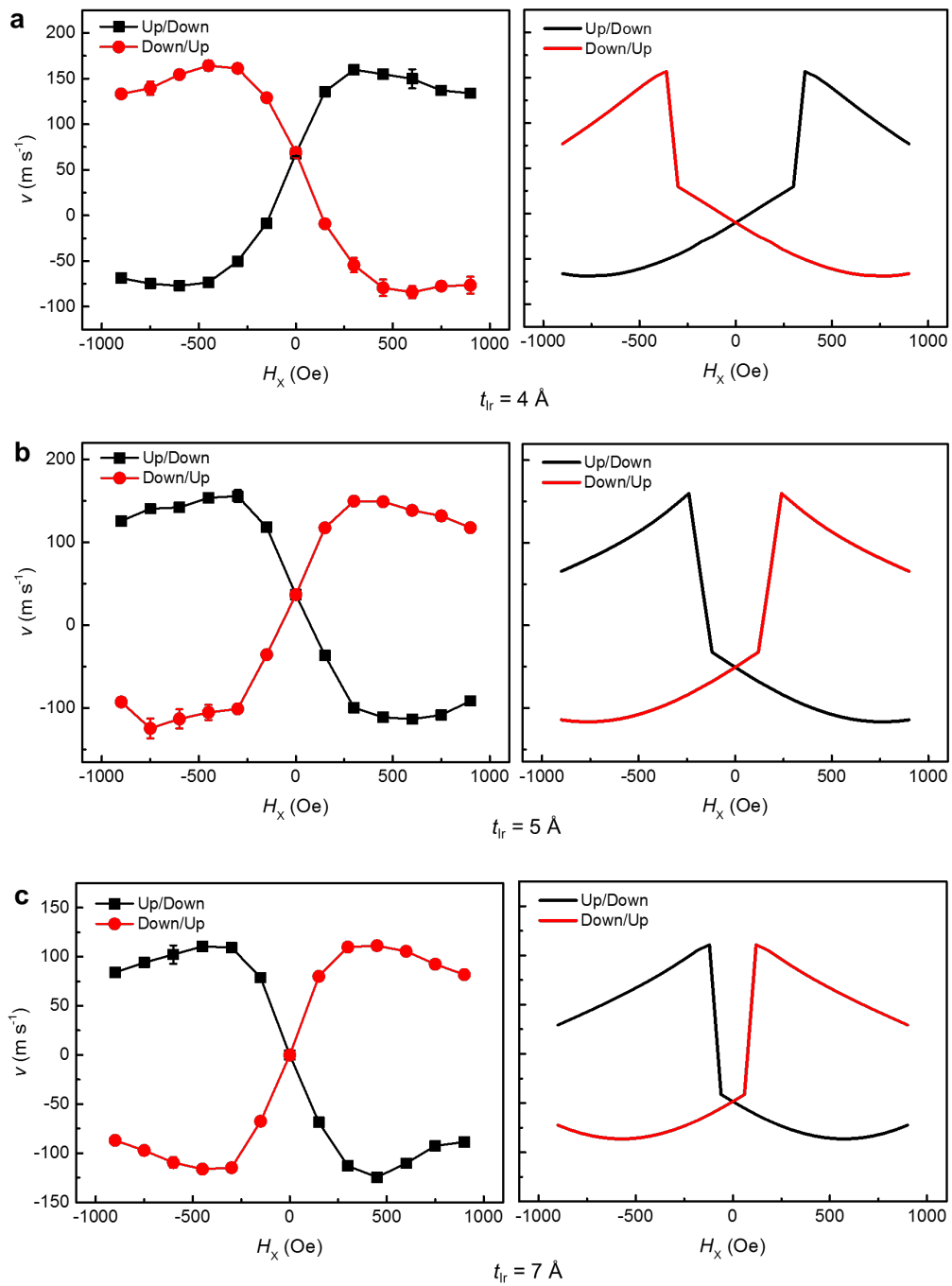


Figure B-8: Fitting results of CIDWM in SAF. Experimental results of the longitudinal field dependence of the DW velocity in the Ir DL system (left panel) and the corresponding simulations (right panel) based on the 1-D model with DL thicknesses of: 4 Å (a), 5 Å (b) and 7 Å (c).

B.3. Determination of the Gilbert damping parameter from optical ferromagnetic resonance (OFMR) measurements

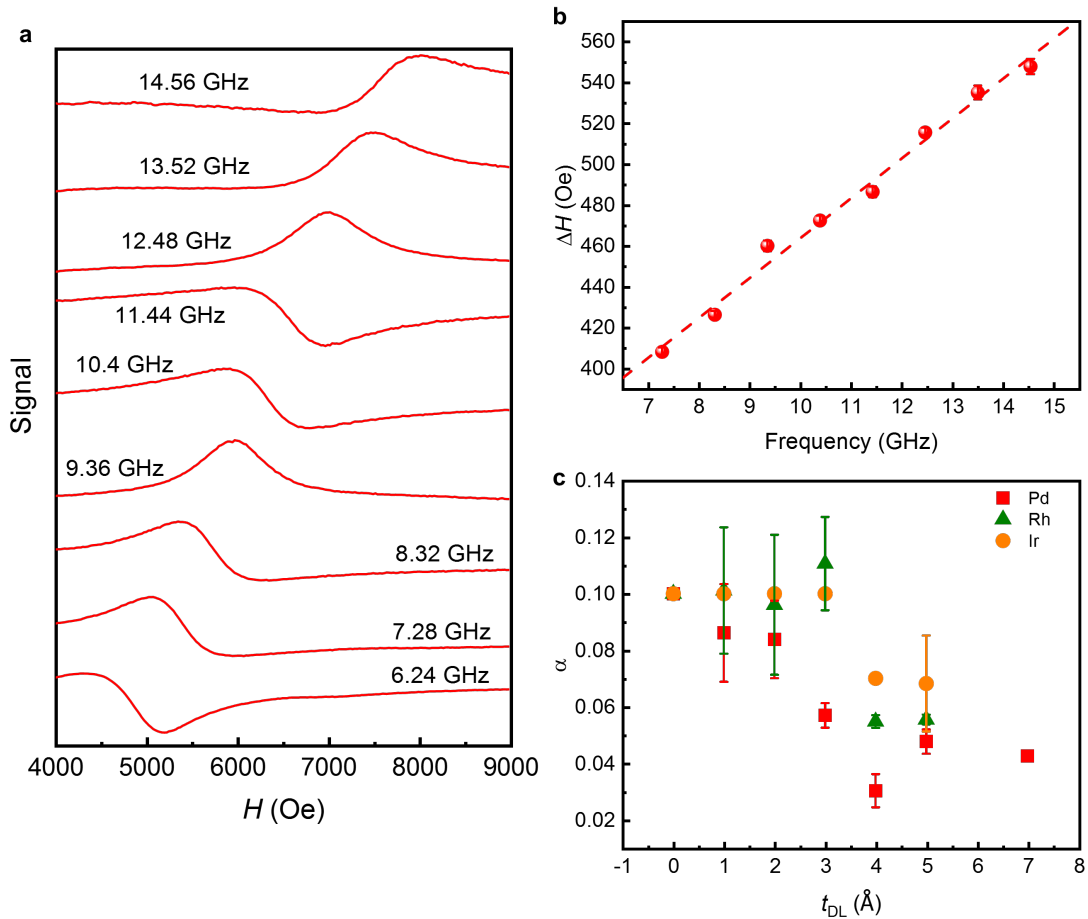


Figure B-9: OFMR determined Gilbert damping parameter for samples with DLs. (a) The OFMR spectra of the sample with a 4 Å Rh DL for various frequencies; (b) The fitted linewidth of the OFMR spectra in Figure B.9a plotted as a function of frequency; (c) Summary of the damping parameters obtained for different DL materials and thicknesses.

Acknowledgment

First of all, I would like to express my sincere gratefulness to my mentor, Prof. Stuart S.P. Parkin. Stuart offered me this great opportunity to join his group to carry out my Ph.D research. Under his supervision, I have acquired not only the profound knowledge in the research field of spintronics but also an open mind and enthusiasm towards a scientific career. His creativity and wisdom have benefitted me in every possible way of doing research. It is a great honor to share this wonderful and productive three years with Stuart, and this unforgettable memory will be of tremendous and far-reaching influence on my future academic life.

I also want to express my gratitude to Prof. Chiba Daichi of Osaka University, who supervised me during my Master period. Prof. Chiba has guided me into the field of spintronics and inspired me for continuously pursuing academic accomplishments.

Furthermore, I would like to give special thanks to Dr. Xilin Zhou and Tianping Ma, who have unselfishly offered me endless help through my Ph.D research. Their versatility in experimental skills and cautious attitudes towards researches have greatly affected me and set great examples as a rigorous scientist. Apart from scientific research, the joyful time we shared is the priceless treasure that I will cherish forever in my mind.

I also want to give my deepest gratitude to Dr. See-hun Yang. His has deepened my understanding of the mechanisms behind the domain wall motion through fruitful discussions and thoughtful guidance. Every time I talked to him, it was always delightful and enlightening. I would like to thank all the colleagues and employees in the Max Planck Institute of Microstructure Physics. Because of their continuing support and heart-warming company, I could make this far to accomplish my Ph.D.

Finally, I want to thank my family, who has always been the spiritual beacon and soul harbor for me across these ten years since I left my home for undergraduate in 2010. Throughout my studies, it is their company and support that offered me the strength to overcome all the obstacles.

Eidesstattliche Erklärung

Ich, Guan Yicheng, erkläre an Eides statt, dass ich die Arbeit selbstständig und ohne fremde Hilfe verfasst, keine anderen als die von mir angegebenen Quellen und Hilfsmittel benutzt und die den benutzten Werken wörtlich oder inhaltlich entnommenen Stellen als solche kenntlich gemacht habe.

Halle (Saale), den 09.09.2020

(Guan Yicheng)

Academic Curriculum Vitae

First Name: Yicheng
Family Name: Guan
Gender: Male
Date of Birth: August 3rd, 1992
Place of Birth: Wuxi, Jiangsu Province, China
Address: Gerhard-Marks-Straße. 10, Halle (Saale), 06120
Nationality: Chinese

ACADEMIC EDUCATION

02/2018 – *Ph.D Candidate (Physics)*
Martin-Luther-University Halle-Wittenberg, Halle, Germany
Max-Planck Institute of Microstructure Physics, Halle,
Germany
Supervisor: Stuart Parkin

09/2015 – 09/2017 *Master's degree in Engineering*
Department of Applied Physics
University of Tokyo, Tokyo, Japan
Supervisor: Chiba Daichi

09/2010 – 09/2015 *Bachelor's degree in Science*
Department of Physics
Tsinghua University, Beijing, China

Yicheng Guan
Halle (Saale), Germany
September 9th, 2020

Halle (Saale), den 09.09.2020

(Guan Yicheng)

Publications

Y. Guan, X. Zhou, T. Ma, R. Bläsing, H. Deniz, S.-H. Yang, and S. S. P. Parkin. Increased efficiency of current-induced motion of chiral domain walls by interface engineering. *Advanced Materials*, 33(10), 2007991, 2021

Y. Guan, X. Zhou, F. Li, T. Ma, S.-H. Yang, and S. S. P. Parkin. Ionic liquid gate control of current induced domain wall motion in synthetic antiferromagnets. *Manuscript submitted to Nature Communication*.

Y. Guan, T. Koyama, and D. Chiba. Current-induced magnetic domain wall motion in Pt/Co/Pd and Pd/Co/Pt structures with opposite sign of Dzyaloshinskii-Moriya interaction. *AIP Advances*, 7(8), 085123, 2017

T. Koyama, Y. Guan, Y. Hibino, M. Suzuki, and D. Chiba. Magnetization switching by spin-orbit torque in Pt with proximity-induced magnetic moment. *Journal of Applied Physics*, 121 (12), 123903, 2017

T. Koyama, Y. Guan, and D. Chiba. Investigation of spin-orbit torque using current-induced magnetization curve. *Scientific Reports*, 7(1), 1-8, 2017